

Analysis and analytical modeling of wake aerodynamics  
behind horizontal-axis wind turbines

(水平軸風車後流の空気力学の解析とモデル化)

January 2023

Doctor of Philosophy (Engineering)

Qidun Maulana Binu Soesanto

キドゥン マウラナ ビヌ スサント

Toyohashi University of Technology



Date of Submission (January 6<sup>th</sup>, 2023)

Department of Mechanical Engineering		Student ID Number	D199103	Supervisors	Akiyoshi Iida
Applicant's name		Qidun Maulana Binu Soesanto			Yuji Nakamura
					Hiroshi Yokoyama

## Abstract (Doctor)

Title of Thesis	Analysis and analytical modeling of wake aerodynamics behind horizontal-axis wind turbines
-----------------	--

Approx. 800 words

The wake transition mechanism behind an isolated non-yawed horizontal-axis wind turbine (HAWT) has been investigated using a low-cost analytical model. The wake itself is defined as the region downstream of the HAWT identified by reduced wind speed. There are two main regions within the wake flowfield behind the HAWT: (i) the near-wake region (ii) the far-wake region. Within the near-wake region, the velocity profile resembles a double-Gaussian shape with two local minima located around the blade midspan due to the suboptimal shape of the blade root and the effect of tip vortices at the blade tip. Meanwhile, within the far-wake region, the wake is completely developed and forms a single-Gaussian shape distribution. Within a full-wake region, it was clarified that the wake expands linearly in an anisotropic manner. All the mentioned wake characteristics are considered in the present study to model the wake transition mechanism within a full-wake region of the HAWT. The preliminary study was conducted to investigate the wake characteristics within the near-wake region using high-fidelity large eddy simulation (LES) data by finite element code FrontFlow/blue (FFB). It was clarified that the wake profile could be approximated by bimodal distribution. The wake was found to recover faster in the lateral direction than in the vertical direction, thus confirming the anisotropic manner of the wake expansion. In addition, it was observed that the wake tends to expand linearly with the downstream distance behind

the HAWT.

Results in the preliminary study were considered in further work to propose an anisotropic double-Gaussian wake model for predicting the wake transition mechanism within a full-wake region behind the non-yawed HAWT. The transition of the wake velocity from the double-gaussian (DG) shape in the near-wake region to the single-Gaussian (SG) shape in the far-wake region by considering the anisotropic wake expansion has been successfully modeled. The effectiveness of the proposed model was validated using LES results and lidar measurements. It was shown that the proposed model could give good agreement with the benchmark datasets. In addition, the performance of the proposed model was compared to the other analytical models based on the top-hat and single-Gaussian shapes. In general, the proposed model has better performance than the other analytical models to predict the wake shape distribution, particularly within the near-wake region where the wake formed the double-Gaussian velocity profile.

Another work in this study intended to propose a linear wake expansion function for the DG analytical wake model. The proposed expansion function for the DG model was constructed from several existing formulations based on the conservation of mass and momentum. By considering the physical and statistical approaches, a linear wake expansion function was derived, thus allowing its direct usability without a prior adjustment/tuning of the wake expansion parameter. The effectiveness of the expansion function was validated with the LES and experimental measurement results, and its performance was also compared to the existing expansion function with tuning. It was clarified both qualitatively and statistically that the proposed expansion function could provide reasonable estimations of the wake expansion within full-wake regions and had comparable results with the tuned expansion function. These results indicate the practicability of the proposed expansion function for the DG wake model to predict the wake recovery within a full-wake region of the HAWT. Furthermore, the proposed expansion function was also evaluated to predict multiple wakes behind three aligned turbines. In general, the result shows that the analytical prediction could give a good agreement with the benchmark dataset from high-fidelity LES by FFB. This indicates the ability of the proposed expansion function to be used in predicting multiple wakes behind the HAWTs in addition to the single wake cases.

## **Acknowledgment**

I greatly thank my supervisor Prof. Akiyoshi Iida for his supervision, advice, and support from the very beginning of my doctoral study; Assistant Prof. Tsukasa Yoshinaga for his supervision and support; Prof. Chisachi Kato, Prof. Yuji Nakamura, and Assoc. Prof. Hiroshi Yokoyama for their constructive advice on my research works. Dr. -Ing. Johannes Schreiber for his technical support; The team from CL-Windcon project for providing me the LES results by Simulator fOr Wind Farm Applications (SOWFA) for validation purposes; The Technical University of Denmark (DTU) for sharing their LES results from EllipSys3D for validation purposes. The past and current members of the Natural Energy Conversion Science Laboratory for our meaningful discussions and their support since day one in Japan; Ms. Suzuki for her administrative support; and the Indonesian and International students in TUT for unforgettable memories. I also greatly thank my wife, Novera Istiqomah, for her unconditional love, patience, and support; My son, Daffa Maulana Rafisqy, for his cheerfulness and understanding, which always motivate me; My parents, for their unceasing love and support, My mother-in-law and father-in-law for their support; My brothers, sisters, and big family in Indonesia. Finally, I gratefully acknowledge the financial support from MEXT Japan, who awarded me with MEXT Scholarship.

# Table of Contents

<b>Acknowledgment</b> .....	<b>iii</b>
<b>Table of Contents</b> .....	<b>iv</b>
<b>List of Figures</b> .....	<b>vii</b>
<b>List of Tables</b> .....	<b>x</b>
<b>Chapter 1</b> .....	<b>1</b>
<b>Introduction</b> .....	<b>1</b>
1.1    General overview .....	1
1.2    Wake transition mechanism behind a HAWT .....	3
1.3    State of the art of WLMs .....	5
1.3.1    CFD-based WLMs .....	5
1.3.2    Analytical-based WLMs.....	7
1.4    Current challenges in the HAWT wake modeling.....	8
1.5    Objectives .....	10
1.6    Limitations .....	10
1.7    Structure of dissertation.....	10
<b>Chapter 2</b> .....	<b>13</b>
<b>HAWT wake aerodynamics</b> .....	<b>13</b>
2.1    Wind velocity .....	13
2.2    Atmospheric boundary layer .....	13
2.3    HAWT blade aerodynamics .....	16
2.4    One-dimensional momentum theory .....	18
2.5    Analytical modeling of HAWT wake.....	21
2.5.1    Top-hat wake model.....	22
2.5.2    SG wake model .....	24
2.5.3    DG wake model.....	25
<b>Chapter 3</b> .....	<b>28</b>
<b>Investigation of the near-wake behavior of an isolated HAWT</b> .....	<b>28</b>
3.1    Overview .....	28
3.2    Introduction .....	28
3.3    Methodology .....	29
3.3.1    Wind Turbine Modeling.....	29
3.3.2    Numerical schemes.....	30
3.3.3    LES turbulence modeling.....	31

3.3.4	The DG function for the near-wake flow field prediction .....	32
3.3.5	Objective Function.....	33
3.4	Results and discussion .....	34
3.4.1	The Wake Centerline .....	34
3.4.2	Contour of streamwise velocity .....	35
3.4.3	Streamwise velocity in the vertical direction .....	36
3.4.4	Streamwise velocity in the lateral direction .....	38
3.4.5	The Wake Recovery .....	39
3.5	Conclusion .....	40
<b>Chapter 4</b>	<b>.....</b>	<b>42</b>
<b>Anisotropic DG analytical wake model for an isolated HAWT .....</b>		<b>42</b>
4.1	Overview .....	42
4.2	Introduction.....	42
4.3	Methodology .....	44
4.3.1	Anisotropic DG wake model.....	44
4.3.2	Model validation .....	52
4.3.3	Model calibration .....	53
4.3.4	Model performance evaluation .....	54
4.4	Results and discussion .....	55
4.4.1	Streamwise wake velocity of NREL 5 MW HAWT within a near-wake region .....	55
4.4.2	Streamwise wake velocity of INNWIND 10 MW HAWT within a full-wake region...	58
4.4.3	Wake velocity centerline of utility-scale AREVA 5 MW HAWT within a full-wake region .....	62
4.4.4	Statistical evaluation .....	64
4.5	Conclusion .....	72
<b>Chapter 5</b>	<b>.....</b>	<b>74</b>
<b>A linear wake expansion function for the DG analytical wake model.....</b>		<b>74</b>
5.1	Overview .....	74
5.2	Introduction.....	74
5.3	Methodology .....	77
5.3.1	Linear wake expansion function for the DG analytical wake model .....	77
5.3.2	Validation.....	81
5.4	Results and discussion .....	82
5.4.1	The near-wake region.....	82
5.4.2	The full-wake region.....	87
5.4.3	Statistical evaluations.....	101

5.4.4	Comparison of wind power potential .....	103
5.4.5	The performance comparison of the evaluated Cases 4-7 .....	105
5.5	Conclusion.....	107
<b>Chapter 6</b>	.....	<b>109</b>
<b>Analysis of multiple wakes behind the HAWTs.....</b>		<b>109</b>
6.1	The wake flowfield of multiple turbines .....	109
6.2	Analytical modeling of multiple wakes.....	112
6.3	Conclusion.....	114
<b>Chapter 7</b>	.....	<b>116</b>
<b>General discussion.....</b>		<b>116</b>
<b>Conclusion and future works .....</b>		<b>118</b>
8.1	Conclusion.....	118
8.2	Limitations and future works .....	121
<b>References</b>	.....	<b>122</b>

## List of Figures

<b>Figure 1. 1.</b> Contour of instantaneous streamwise wake velocity behind two NREL 5MW HAWTs in tandem arrangement. ....	1
<b>Figure 1. 2.</b> Experimental visualization of three-dimensional helical vortex structures shed from blades' root and tip of a turbine rotor under different tip speed ratios .....	2
<b>Figure 1. 3.</b> Wake development behind a HAWT and its transition mechanism .....	3
<b>Figure 1. 4.</b> Field measurements of AREVA M5000 offshore HAWT's wake at the North Sea using scanning lidar .....	4
<b>Figure 1. 5.</b> Wind tunnel measurements of HAWT model's wake under varying atmospheric stability using laser doppler anemometer.....	5
<b>Figure 1. 6.</b> Schematic of indirect methods for blade modeling.....	6
<b>Figure 1. 7.</b> Details of mesh refinement around direct blade modeling. ....	7
<b>Figure 1. 8.</b> The wake velocity distribution.....	8
<b>Figure 2. 1.</b> An illustration of the vertical velocity profile in a streamwise direction within the ABL	14
<b>Figure 2. 2.</b> Blade element at radius $r_e$ with element radial length $\delta r_e$ sweeping out in annular within a HAWT blade swept area .....	16
<b>Figure 2. 3.</b> Wind velocity triangle and aerodynamics forces at HAWT blade section (airfoil).....	17
<b>Figure 2. 4.</b> Schematic of actuator disc model from the horizontal-axis wind turbine.....	19
<b>Figure 2. 5.</b> Cylindrical control volume around a wind turbine rotor with the surface area $A_T$ and volume $X$ .....	21
<b>Figure 2. 6.</b> Schematic of top-hat wake velocity profile behind a HAWT.....	23
<b>Figure 2. 7.</b> Illustration of wake development behind a HAWT using SG analytical wake model.....	24
<b>Figure 2. 8.</b> Illustration of the wake development behind a HAWT using the DG analytical wake model. ....	26
<b>Figure 3. 1.</b> Computational domain of the turbine simulation .....	31
<b>Figure 3. 2.</b> The centerline velocity at the hub height along the axial direction. The Blue dashed line shows the axial position of the rotor. ....	34
<b>Figure 3. 3.</b> The contour of normalized streamwise wake velocity.....	35
<b>Figure 3. 4.</b> The contour of normalized cross-sectional wake velocity at several downstream distances within the near-wake region. ....	36
<b>Figure 3. 5.</b> Vertical profile of streamwise wake velocity at several downstream distances. ....	37
<b>Figure 3. 6.</b> Lateral profile of streamwise wake velocity at several downstream distances. ....	38
<b>Figure 3. 7.</b> The mean wake velocity in the vertical and lateral directions. ....	39
<b>Figure 4. 1.</b> Streamtube control volume of horizontal-axis wind turbine rotor modelled by an actuator disc. ....	45

<b>Figure 4. 2.</b> Case-averaged total RMSE against LES simulations and lidar measurements for pairs of parameter $r_0$ and coefficient $c$ .....	50
<b>Figure 4. 3.</b> RMSEs averaged from both lateral and vertical directions at each evaluated downstream distance. ....	51
<b>Figure 4. 4.</b> Streamwise wake velocity profiles of NREL 5MW HAWT in the lateral direction within the near-wake region. ....	56
<b>Figure 4. 5.</b> Streamwise wake velocity profiles of NREL 5MW HAWT in the vertical direction within the near-wake region. ....	57
<b>Figure 4. 6.</b> Streamwise wake velocity profile of INNWIND 10 MW HAWT in the lateral direction within a full-wake region.....	60
<b>Figure 4. 7.</b> Streamwise wake velocity profile of INNWIND 10 MW HAWT in the vertical direction within a full-wake region.....	61
<b>Figure 4. 8.</b> The wake centerline profile downstream of the AREVA 5MW HAWT at different incoming streamwise velocities.....	63
<b>Figure 4. 9.</b> Average RMSE against lidar measurement (case 3) within the near-wake, far-wake, and full-wake regions at the incoming reference velocity of 7 m/s. ....	66
<b>Figure 4. 10.</b> Average RMSE against lidar measurement (case 4) within the near-wake, far-wake, and full-wake regions at the incoming reference velocity of 9 m/s. ....	66
<b>Figure 4. 11.</b> Average RMSE against lidar measurement (case 5) within the near-wake, far-wake, and full-wake regions at the incoming reference velocity of 11 m/s. ....	66
<b>Figure 4. 12.</b> Total RMSE against lidar measurements (cases 3-5) within the near-wake, far-wake, and full-wake regions. ....	67
<b>Figure 4. 13.</b> Average RMSE against lidar measurements (cases 3-5) within the practical region at different incoming streamwise velocities. ....	68
<b>Figure 4. 14.</b> Total RMSE against lidar measurement (cases 3-5) within the practical downstream distance. ....	69
<b>Figure 4. 15.</b> RMSE against LES simulation of INWIND 10 MW (case 2) at different directions .....	70
<b>Figure 4. 16.</b> Average RMSE against LES simulation of INWIND 10 MW (case 2) within the near-wake, far-wake, and full-wake regions.....	71
<b>Figure 4. 17.</b> Average RMSE against LES simulation of INWIND 10 MW (case 2) within the practical downstream distance. ....	72
<b>Figure 5. 1.</b> Illustration of the proposed expansion function for the analytical DG wake model.....	77
<b>Figure 5. 2.</b> Wake velocity profiles at the hub height under uniform inlet with $U_0 \approx 11.4$ m/s and incoming $TI_{x,hub} \approx 3\%$ within the near-wake region (Case 1).....	83
<b>Figure 5. 3.</b> Wake velocity profiles at the hub height under uniform inlet with $U_0 \approx 11.4$ m/s and incoming $TI_{x,hub} \approx 6.8\%$ within the near-wake region (Case 2). ....	85

<b>Figure 5. 4.</b> Wake velocity profiles at the hub height under ABL inlet with $U_0 \approx 11.6$ m/s and incoming $TI_{x,hub} \approx 7.1$ % within the near-wake region (Case 3).....	86
<b>Figure 5. 5.</b> Contours of streamwise wake velocity on the horizontal plane at the hub height within the full-wake region .....	88
<b>Figure 5. 6.</b> Standard deviation of DG velocity deficit profile centered at the local Gaussian minima ( $\sigma$ ) and wake radius ( $r_w$ ) as functions of the normalized downstream distance ( $x/D$ ).....	90
<b>Figure 5. 7.</b> The normalized velocity deficit at the centerline $\Delta U_c/U_{hub}$ for Cases 4-7.....	91
<b>Figure 5. 8.</b> Wake velocity profiles at the hub height in the lateral direction behind a G1 model turbine within the full-wake region (Case 4).....	93
<b>Figure 5. 9.</b> Wake velocity profiles at the hub height in the lateral direction behind an INNWIND 10 MW reference turbine within the full-wake region (Case 5). .....	95
<b>Figure 5. 10.</b> Wake velocity profiles at the hub height in the lateral direction behind an INNWIND 10 MW reference turbine within the full-wake region (Case 6). .....	98
<b>Figure 5. 11.</b> Wake velocity profiles at the hub height in the lateral direction behind an NREL 5 MW reference turbine within the full-wake region (Case 7).....	101
<b>Figure 5. 12.</b> Comparison of the normalized root mean square error NRMSE and the linear correlation coefficient R between the proposed and the tuned expansion functions.....	102
<b>Figure 5. 13.</b> Comparison of the normalized wind power potential $P_w/P_{ref,w}$ between the analytical predictions and their benchmark datasets.....	104
<b>Figure 6. 1.</b> Inlet velocity profile of the FFB simulation for the triple turbine case and its power law fit. ....	109
<b>Figure 6. 2.</b> Contours of the mean wake velocity of triple turbines on the horizontal and vertical planes. ....	110
<b>Figure 6. 3.</b> Contours of the streamwise turbulence intensity of triple turbines on the horizontal and vertical planes.....	111
<b>Figure 6. 4.</b> Profile of the streamwise turbulence intensity within multiple wakes behind the triple turbines.....	111
<b>Figure 6. 5.</b> Measurement points for geometric averaging of the wake velocity. ....	112
<b>Figure 6. 6.</b> The thrust coefficient ( $C_t$ ) of NREL 5 MW turbine as a function TSR. ....	113
<b>Figure 6. 7.</b> Geometric averaging of wake velocity downstream of the triple turbines. ....	114

## List of Tables

<b>Table 2. 1.</b> Estimations of surface roughness length at different terrains [32].....	15
<b>Table 2. 2.</b> Estimations of power-law exponent $\alpha$ at different terrain characteristics [33]. ....	15
<b>Table 3. 1.</b> Specifications of NREL 5 MW offshore HAWT.....	30
<b>Table 4. 1.</b> Relevant cases from CFD simulation and LiDAR measurements to validate the proposed DG model. ....	52
<b>Table 4. 2.</b> Tuned wake expansion parameters of the respective wake models for different case studies.....	54
<b>Table 5. 1.</b> The normalized velocity deficit $\Delta U/U_{hub}$ , the DG shape function $f(ry, z, \sigma x)$ , and the DG amplitude function $C(\sigma x)$ . ....	80
<b>Table 5. 2.</b> Case studies used to validate the proposed expansion function.....	81
<b>Table 5. 3.</b> Far-wake onset and tuned $k^*$ parameter for Cases 4-7. ....	89
<b>Table 5. 4.</b> The mean values of NRMSE, R coefficient, and $\Delta P_w/P_{ref,w}$ within the full-wake region. ....	106
<b>Table 5. 5.</b> The mean values of NRMSE, R coefficient, and $\Delta P_w/P_{ref,w}$ within the practical region. ....	106
<b>Table 8. 1.</b> Findings and Contributions of the presented works.....	119
<b>Table 8. 2.</b> Limitations and future works .....	121

# Chapter 1

## Introduction

### 1.1 General overview

Wind energy offers great potential for power generation. Despite its great potential to become the main player in the future energy system, further investigations are needed, especially for understanding the wake aerodynamics due to their negative impact on the overall wind farm performance. Investigation into wind turbine wakes has a long history since the late 70s when the utilization of clean, renewable source of wind energy for massive power generation was increasingly in demand among the stakeholders. From the outsider's perspective, the aerodynamics of horizontal-axis wind turbine (HAWT) wakes may seem simple, particularly when considering the one-dimensional axial momentum theory. However, the actual description is much more complicated by the fact that the inflow is always subject to stochastic wind fields, and that loss becomes an intrinsic part of turbines that are not pitch-regulated [1]. Some relevant investigations have been carried out by simulating the atmospheric wind fields where the HAWT wakes were investigated in a controlled environment, such as wind tunnels, or using computational fluid dynamics (CFD) simulation.

The HAWT wake can be defined as the wind flow downstream of the turbine characterized by reduced wind speed due to momentum loss from wind energy extraction by the turbine's rotor. As a result, any turbine placed inside the wake region will undergo power losses due to the velocity deficit. This condition can be observed from the numerical result of high-fidelity large eddy simulation (LES) of the wake velocity behind two NREL 5MW HAWTs in a tandem arrangement as shown in Fig. 1.1.

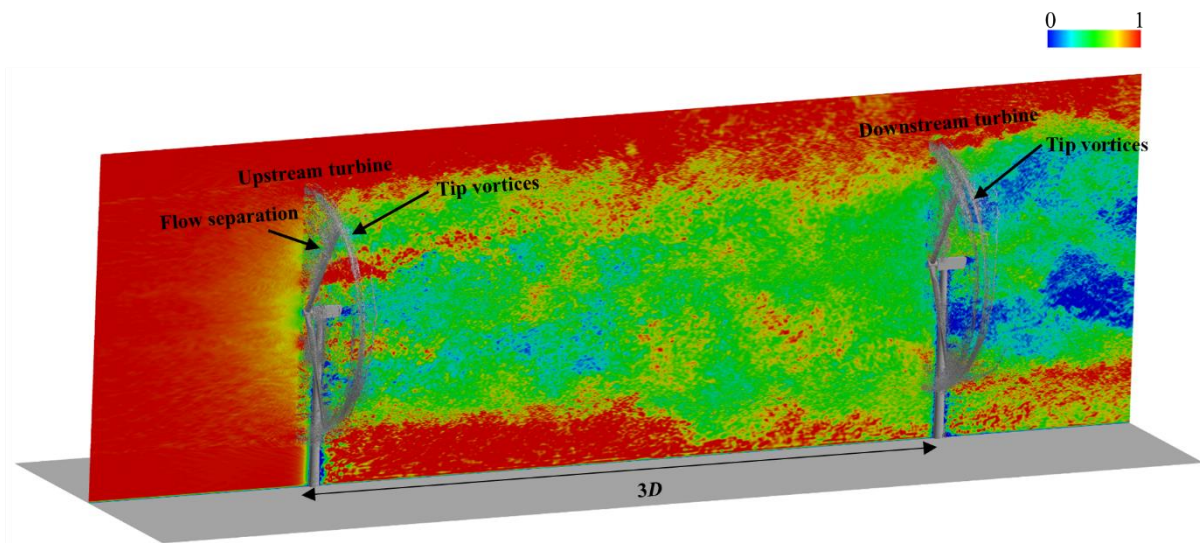


**Figure 1. 1.** Contour of instantaneous streamwise wake velocity behind two NREL 5MW HAWTs in tandem arrangement.

The significant reduction to about half of the undisturbed velocity extracted by the downstream turbine could represent the interference from the upstream turbines' wakes that deteriorate the downstream turbines' performances and consequently reduce the overall power production of the wind farm. Hence, the turbine micro-siting scenario becomes extremely important for a wind farm's net power production and lifespan.

In general, the wake turbine consists of two main regions: (i) the region immediately downstream of the turbine, called the near-wake; and (ii) the region further downstream, called the far-wake. Meanwhile, the upwind region affected by the turbine is called the induction region. The near-wake region is more dominated by the turbine presence, thus detailed features of the turbine's main components such as blade and nacelle geometries can influence the flow field in this region. In the near-wake, the velocity deficit profile in the lateral and vertical directions depends on the amount of lift produced along the span of the blade [2]. The maximum lift generated around the blade mid-span causes maximum velocity deficit around the mid-span position within the near-wake region. Meanwhile, a very small lift around the blade's root due to the suboptimal shape of the airfoil cross-section attenuates the velocity deficit, which becomes lesser around the blade's tip due to the shear layer. As a result, the double-Gaussian (DG) velocity profile with two local minima located around the blade mid-span position is formed within the near-wake region.

Another interesting feature within the near-wake region that may be visible is the vorticial structures shed from the blade's tip and root in helical trajectories towards the downstream direction as shown in Fig. 1.2.

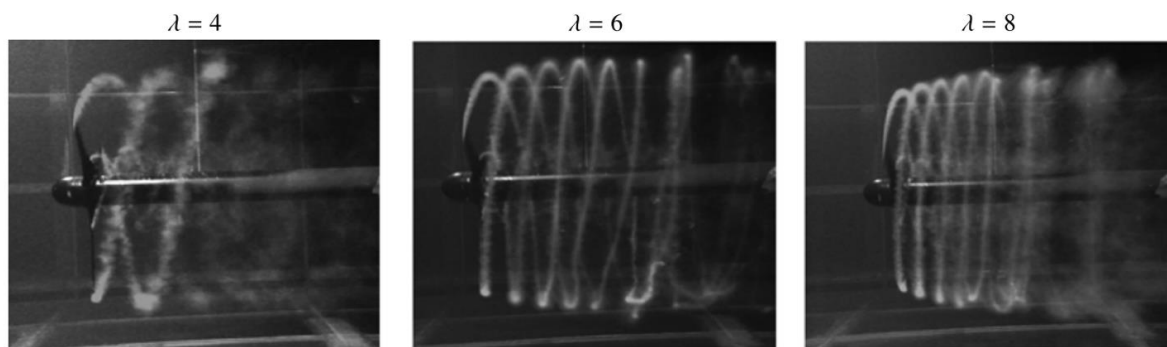


**Figure 1. 2.** Experimental visualization of three-dimensional helical vortex structures shed from blades' root and tip of a turbine rotor under different tip speed ratios [3].

The helical vortex structures are caused by the pressure difference between the pressure and suction sides of the rotor blade, with a shedding frequency three times the rotor rotational frequency for a three-bladed HAWT [4]. The helix pitch, or the axial distance between two consecutive vortices, decreases with the increase of TSR. Moreover, the pitch of tip vortices is greater than that of root vortices.

In contrast to the near-wake region, the far-wake region is less influenced by the presence of the turbine. Within this region, the wake is completely developed, which may be assumed that the profiles of both velocity deficit and turbulence intensity are axisymmetric and have self-similar distributions in the cross-sections of the wake [5]. Later it was found that the wake expands in a non-axisymmetric shape, in which the wake expansion rates in the lateral and vertical directions are slightly different [6]. At the farther downstream distances, the wake recovered to its undisturbed velocity and the pressure regained its freestream level. The universal parameters of a wind turbine, such as the thrust coefficient and incoming flow conditions, are likely enough to predict the wake profile distribution within the far-wake region. Due to the stable nature of the main flow within the far-wake region, most of the downstream turbine micro-siting in a wind farm is located within this far-wake region. Based on the micro-siting practices, it is the sub-area of 5 to 10 rotor diameter behind the turbine that attracts the greatest interest of both researchers and project developers [7].

## 1.2 Wake transition mechanism behind a HAWT

A schematic of the wake development behind a HAWT and its transition mechanism is shown in Fig. 1.3. Within the atmospheric boundary layer (ABL), the axial load from the incoming wind is extracted by the rotor, causing pressure drop over its area and creating a wake region downstream of the rotor due to momentum loss. The transition mechanism of the wake velocity evolving downstream of the turbine is influenced by the turbine's physical features and the ambient conditions.

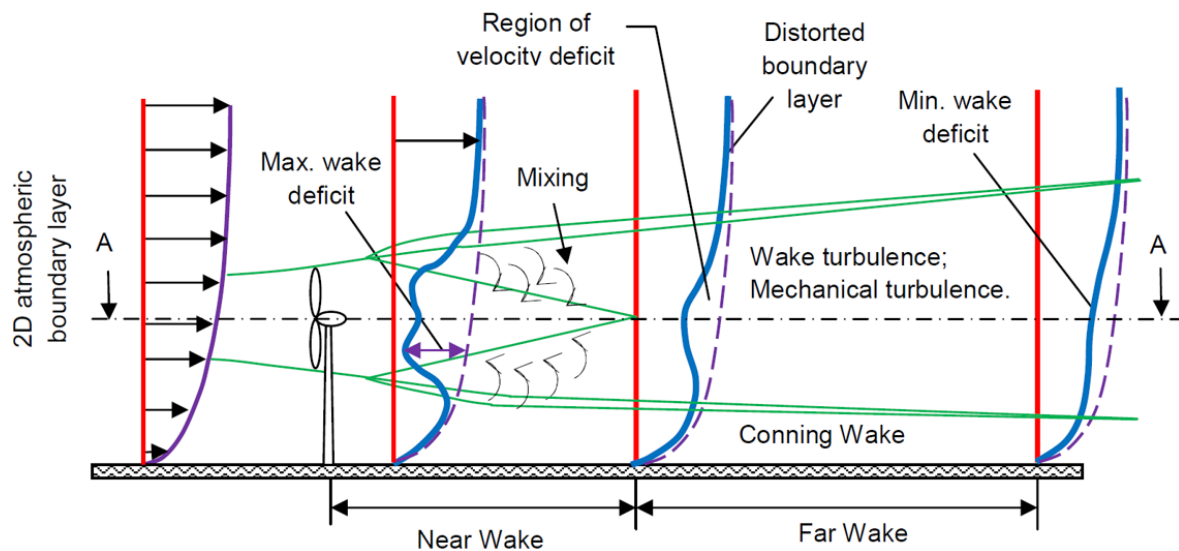


**Figure 1. 3.** Wake development behind a HAWT and its transition mechanism [8].

Starting from the near-wake region, the velocity difference between the wake and the ambient flow creates an annular shear layer that separates the inner core from the ambient flow, where its thickness increases with the downstream distance [9]. Turbulence within this shear layer effectively mixes the lower velocity in the wake with the higher ambient velocity outside the wake, ensuring momentum

transfer towards the wake center. When the shear layer is thick enough to reach the wake center, indicating the end of the near-wake region and the onset of the far-wake region. In this region, the pressure gradient becomes less significant in respect to the atmospheric level. Within the far-wake region, the wake velocity tends to form a single-Gaussian (SG) distribution with the wake axis located around the hub centerline [4]. This tendency is acknowledged as the general characteristic of the far-wake region, idealized as a self-similar axis-symmetric SG wake profile. The attenuation of velocity deficit at further downstream distances in this region is compensated by the expansion in the wake area due to the conservation of mass.

It can be summarized that, in general, the wake velocity distribution has two main shapes, the DG profile within the near-wake region and the SG profile within the far-wake region. These velocity characteristics behind a single HAWT were also observed during field and wind tunnel measurements, as shown in Figs. 1.4 and 1.5, respectively.

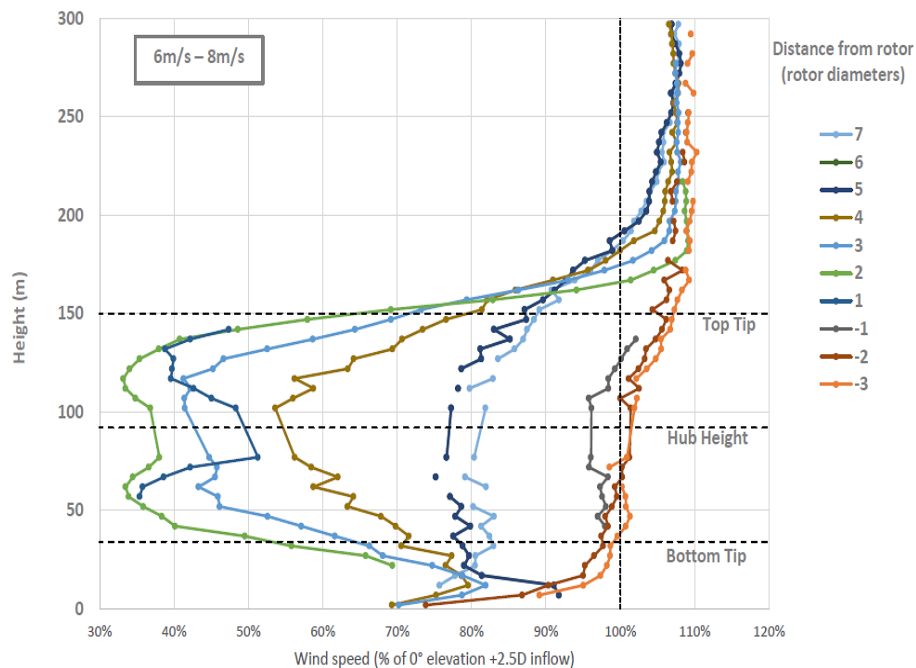


**Figure 1. 4.** Field measurements of AREVA M5000 offshore HAWT’s wake at the North Sea using scanning lidar [10].

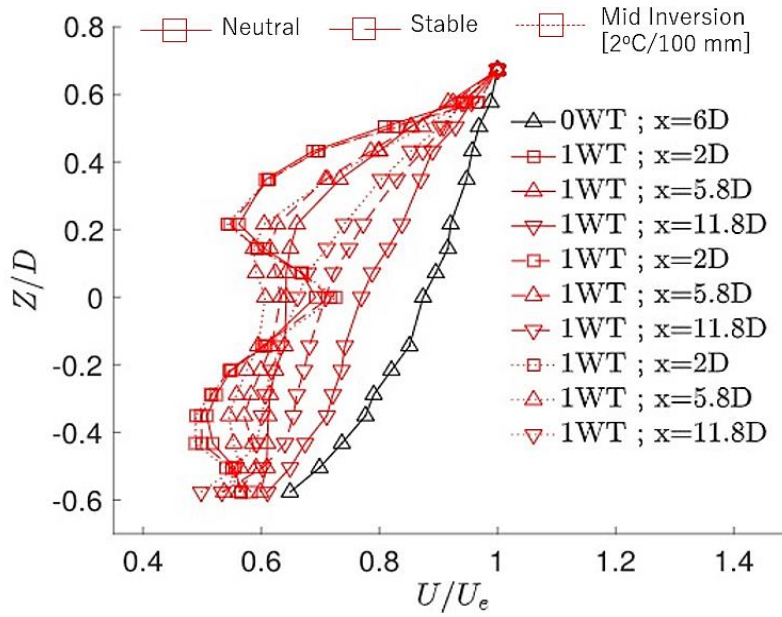


**Figure 1. 5.** Wind tunnel measurements of HAWT model's wake under varying atmospheric stability using laser doppler anemometer [11].

Either from field measurements or wind-tunnel experiments under varying atmospheric stability, the DG and SG wake shapes were observed within the near and far-wake regions, respectively. These general characteristics of velocity distribution behind a single HAWT lay the foundation of the Gaussian-based analytical wake models, which proved more reasonable than the top-hat approach.

### 1.3 State of the art of WLMs

The wake behavior and its negative impact on the downstream turbine performance have attracted several investigators to perform wake modeling by means of wake loss models (WLMs). There are two categories of WLMs: (i) WLMs based on CFD; (ii) Analytical WLMs [12]. The CFD-based WLMs, also known as field models, solve the Navier-Stokes equations numerically. Meanwhile, the analytical WLMs provide an analytical solution to the wind speed deficit or relative power of a downwind turbine with respect to the upstream turbine. State of the art of WLMs for wake modeling is further described in the following section. This section aims to give an overview of the WLMs, which can be used to model a single wake behind a horizontal-axis wind turbine. Some CFD-based and analytical approaches are highlighted, and their methods are briefly described in this section.

#### 1.3.1 CFD-based WLMs

Due to the importance of wake aerodynamics, several publications have been reported in the literature. Some of them focus on the numerical approach of wake modeling using computational fluid dynamics (CFD). This approach was chosen because of its ability to give solutions for various properties of unsteady flow behavior within the wake region in great detail, which are likely very difficult to measure experimentally in a wind tunnel, particularly when implementing real atmospheric conditions

[9]. Since a full-scale CFD simulation of wind turbine wake is computationally expensive, some investigators use indirect methods to simplify the complexity of blade geometry with certain assumptions, hence reducing its computational cost. An illustration of several methods for indirect blade modeling is shown in Fig. 1.6.

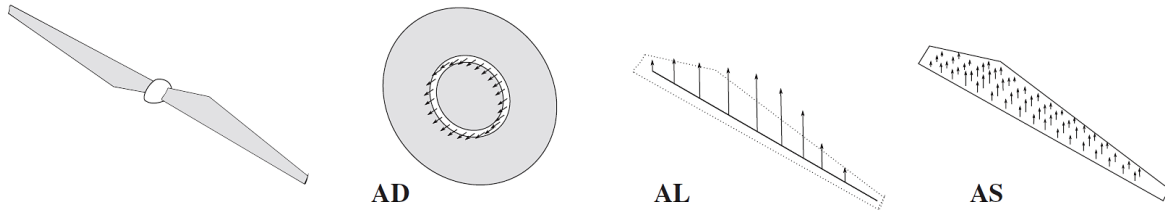


**Figure 1. 6.** Schematic of indirect methods for blade modeling [13]. (a) Actuator disc (AD); (b) Actuator line (AL); (c) Actuator surface (AS).

The AD is modeled by estimating blade loading with uniformly distributed force on the circular disc as a function of the thrust coefficient which is determined from turbine performance curves [14]. The AD method has been extended to a more realistic approach by employing the actuator disc model (ADM) in combination with the blade element momentum (BEM) approach to account for actual blade loading by prescribed different forces based on tabulated airfoil data over the circular disc [15]. A more sophisticated indirect method is the actuator line method (ALM) which replaces the loading of rotor blades by body forces on straight lines where each line represents each blade of the turbine. Compared to the previous methods, ALM has better accuracy when capturing the vortical structures shed from the blade tip within the near-wake region [16]. Although ALM offers more promising results to address the limitations of ADM, the method has lack information regarding force distribution along each airfoil section which is only represented by one point. In order to overcome this problem, the body forces are distributed on each airfoil section as a function of chord length along the blade spanwise direction using a more advanced indirect approach so-called actuator surface method (ASM) [17]. In the ASM, the lift and drag forces calculated using the blade element method are distributed over the actuator surface formed by chord lines at different radial locations of a blade. The results show that the ASM has an intrinsic advantage over the previous indirect methods, especially for flow structure modeling around the blade region of wind turbines.

BEM-based indirect methods such as the actuator methods are effective approaches to retaining computational efficiency. On the other hand, these methods have relied on empirical corrections of chosen two-dimensional airfoil data to account for three-dimensional effects and hence still have limitations, especially for handling viscous effects and separation because of the numerical assumptions being made [18]. Furthermore, for future research on full-scale turbine modeling, information regarding airfoil characteristic data for large-scale turbine blades is often not accessible due to commercial sensitivity; hence the direct approach for large-scale turbine modeling, such as offshore wind turbines,

becomes necessary [19].

The indirect methods for blade modeling with certain assumptions as described above, basically to overcome the computational cost problem. However, if high computational resources are available, the best results of CFD-based wake modeling would have resulted from the direct method of blade modeling. This direct method is crucial, particularly to capture a detailed representation of flow structures around the rotating blades within the near wake region. The direct blade modeling using the structured hexahedral meshes is shown in Fig. 1.7.

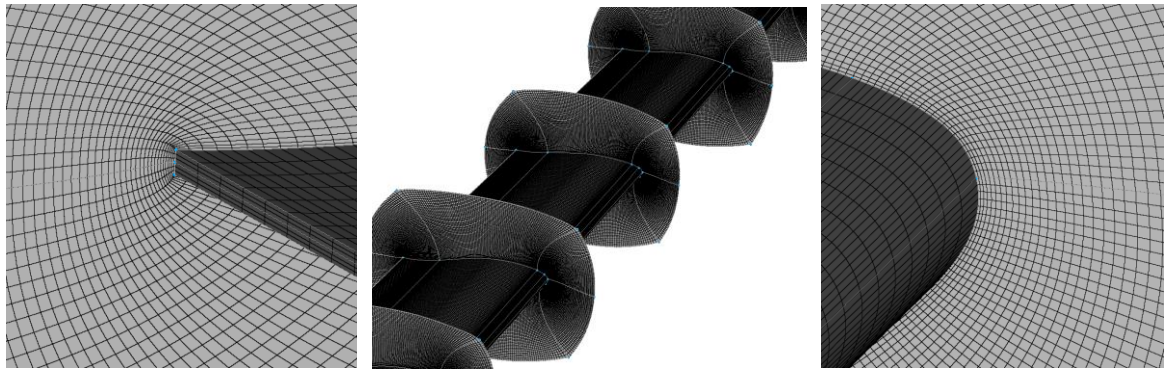


**Figure 1. 7.** Details of mesh refinement around direct blade modeling.

The boundary layers are created along the blade spanwise direction to ensure the quality of the mesh around the blade. This mesh generation step is critical to obtaining a reasonable estimation of the flow separation shedding from the rotating rotor. Using this direct blade modeling in the CFD-based simulation, such as large eddy simulation (LES), a wake flow field behind a utility-scale megawatt-type turbine can be simulated. However, the LES simulation needs large computational resources, which may need weeks to simulate a few minutes of the large-scale wake field. This factor could restrict the affordability of LES-based simulation for practical applications, which require a fast solution of wake estimation.

### **1.3.2 Analytical-based WLMs**

Analytical wake modeling is known for its less expensive yet effective method of giving a fast wake flow field prediction solution. The model was derived from the conservation of mass [20], [21], or the conservation of mass and momentum [5], [22]. There are two main approaches for the wake shape analytical modeling: (i) top-hat shape and (ii) Gaussian shape. The illustration of both the wake shape distribution approaches is shown in Fig. 1.8.

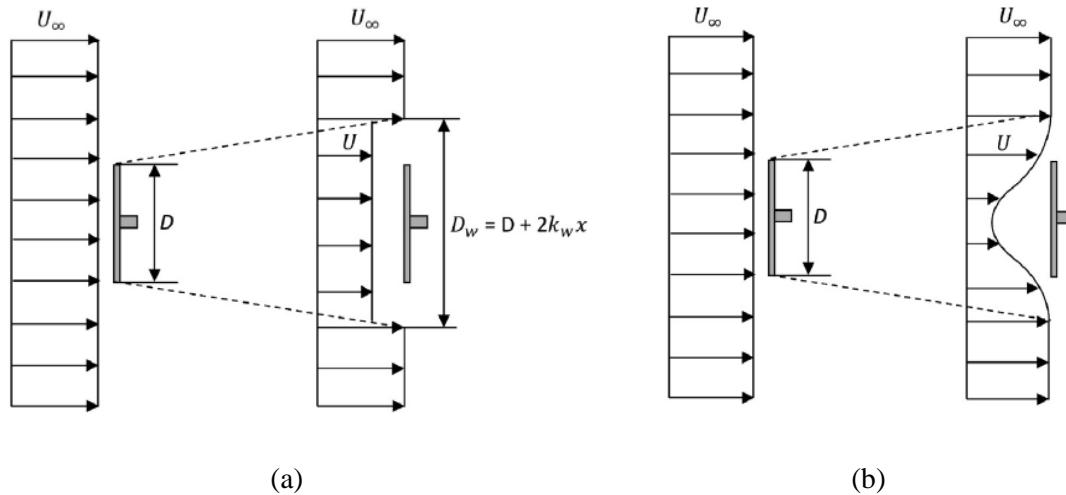


**Figure 1. 8.** The wake velocity distribution. (a) Top-hat shape approach in Jensen model; (b) Gaussian-based approach [12].

The top-hat shape assumes the velocity deficit within the wake region has a constant value, thus resulting in a rectangular distribution of the wake speed. Frandsen et al. [22] argued that the wake-affected wind turbine's rotor integrates the wake over a sizable fraction of its area, thus making finer details less important. Instead of focusing only on the energy content as in the top-hat assumption, the Gaussian analytical models also provide a more realistic representation of wake distribution, particularly within the far-wake region where the wake tends to form a single Gaussian shape profile [4]. It should be reminded that the wind power varies as the cube of the wind velocity. Therefore, the validity of power prediction for the downstream turbine is strongly determined by the accuracy of wake shape distribution within the wake region. The important parameter in the wake loss model is their ability to predict the velocity degradation within the wake region, which is called velocity deficit,  $\Delta U$ . In the analytical wake model, the velocity deficit is strongly affected by the expression of the wake expansion function, which controls the wake growth rate downstream of the turbine.

#### 1.4 Current challenges in the HAWT wake modeling

A too-large distance between the neighboring turbines will result in additional installation costs, whereas too short a distance will result in increased fatigue problems for turbines located in the wake of other turbines [23]. Hence, the wake investigation of the wake transition mechanism within a full-wake region, which covers the near-wake and the far-wake regions, becomes imperative. This investigation can be done by elucidating the wake characteristics properly within a full-wake region behind an isolated turbine, in this case, a utility-scale non-yawed horizontal-axis wind turbine (HAWT).

To date, the wake investigations behind a HAWT have been conducted both experimentally and numerically and have contributed to elucidating the main aerodynamic characteristics of wind turbine wakes, which are important to the development of modern wind turbines. Some important tasks can be

measured using both methods, which are summarized as follows [9]:

- Calculating time-averaged wake flow, which is important to estimate the turbine performance.
- Calculating turbulence intensity in the wake, which is important for structural analyses of the turbine.
- Calculating wake meandering, representing the wake center displacement over time.

There are several reasons for focusing on numerical simulation through CFD against experiments regarding the HAWT wake investigations:

- A full-scale with good-quality experimental measurements of HAWT wake is very expensive and has a limited number of global parameters which can be extracted from the conditioned environments. Meanwhile, the CFD simulation of full-scale HAWT wake can provide detailed information on a lot of flow parameters at any coordinate within the numerical environments.
- Due to variability in the atmospheric conditions, it is difficult to find the mutual interference of turbines on each other.
- The optimization of a full-scale wind farm layout in an experimental setting is almost impossible.

However, CFD computations of full-scale HAWT wake or wind farm aerodynamics face some following challenges:

- High computational resources for full-scale HAWT wake and wind farm aerodynamic simulations may not be affordable among researchers, academics, and stakeholders.
- A high-resolution CFD simulation of megawatt-type HAWT wake with direct blade modeling could take years to obtain a fully-developed wake flow with sufficient averaging data, particularly when dealing with the wake simulations of clustered turbines in a wind farm.

Over the last decade, the deployment of wind farms has grown rapidly due to the high demand for clean and renewable energy resources. Thus, practical solutions become inseparable among the project developers for developing high-performance HAWTs and efficiently supporting wind farm layout optimization. Wind tunnel measurements and CFD simulations can provide an effective solution to gain knowledge in HAWT wake aerodynamics, but less efficient due to expensive experimental setup and high computational resources and time, respectively.

An alternative to experimental and numerical approaches is the analytical approach, which has the potential to give a relatively fast yet feasible solution for practical applications in HAWT wake aerodynamics. However, most of the investigators did not go into the details regarding the investigation and modeling within the near-wake region, particularly behind the utility-scale turbine. As a result, most of the existing analytical wake models are not feasible to be used within the near-wake region, thus limiting their ability to elucidate the wake transition within the full-wake region.

## 1.5 Objectives

The present study aims to contribute to addressing the current challenges of HAWT wake modeling by elucidating the wake transition mechanism within a full-wake region of non-yawed HAWT using a low-cost analytical approach. The findings of this thesis provide new valuable insight into a physically-based wake transition mechanism within a full-wake region behind a utility-scale turbine. To achieve this goal, a series of research works have been done with the following sub-objectives:

1. Further investigating the research question regarding the wake characteristics within the near-wake region. The numerical results from high-fidelity large eddy simulation (LES) of the wake flow behind a utility-scale non-yawed HAWT were analyzed to provide detailed information regarding the wake characteristics within the near-wake region.
2. Performing analytical modeling of the wake transition mechanism within a full-wake region behind a utility-scale non-yawed HAWT by considering the anisotropic behavior of the wake expansion within the near-wake region. The proposed anisotropic DG analytical wake model was validated with the LES simulation and field measurement results.
3. Proposing a linear wake expansion function for the DG analytical wake model. The proposed DG expansion function was validated with LES simulation and the wind-tunnel measurement results.

## 1.6 Limitations

Some limitations in this study are highlighted as follows:

1. The wake analysis in this study covers only HAWTs with the no-yawed condition.
2. Only the wake velocity component in the mainstream direction is estimated.
3. The wake meandering behavior and its effects are not included in the present HAWT wake analyses.
4. Structural analysis is not considered in this study.

## 1.7 Structure of dissertation

This dissertation is constructed from three major works that were sequentially conducted. The first work investigated the detailed wake characteristics in terms of the wake velocity distribution and its expansion within the near-wake region from the high-fidelity LES data. Findings in the first work were considered in the second work to propose the anisotropic DG analytical wake model. Meanwhile, the third work was focused on the development of a linear wake expansion function for the DG wake model. In total, the dissertation consists of seven chapters. Some parts in each chapter of this dissertation are excerpts from the resulting publications of the conducted works.

### ◆ Chapter 1: Introduction

The dissertation's relevant background and references, current challenges, objectives, limitations, and structure of the dissertation are presented in this chapter.

◆ **Chapter 2: HAWT wake aerodynamics**

This chapter gives an overview of the theoretical basics of HAWT aerodynamics, and the basic theory and assumptions underlying the formulation for a HAWT wake analytical modeling.

◆ **Chapter 3: Investigation of the near-wake behavior of an isolated HAWT**

This chapter presents the HAWT wake behavior within the near region in terms of streamwise wake velocity distribution in the lateral and vertical directions.

**Background**

Much research has been carried out to elucidate the wake flow behavior using experimental, numerical, and analytical approaches. Nevertheless, a detailed investigation, particularly within the near-wake region, has received less attention which may be caused by the complex flow field inside this region and micro-siting of wind turbines commonly located within the far-wake region. This study aims to investigate the wake flow behavior within a near-wake region behind a full-scale isolated NREL 5 MW HAWT. The three-dimensional LES data of time-averaged streamwise wake velocity were processed and analyzed. A detailed wake shape distribution and its expansion are highlighted and discussed.

**Outcome**

Further insight into the near-wake flow characteristics was obtained. The DG wake profile distribution was observed, and the anisotropy behavior of wake expansion within the near-wake region was revealed in this study.

◆ **Chapter 4: Anisotropic DG analytical wake model for an isolated HAWT**

The DG approach for analytical wake modeling by considering the anisotropic behavior of the wake expansion is proposed.

**Background**

To date, the analytical investigations that focused on wake development within the near-wake region are few. Related to the near-wake study, Aitken et al. [24] developed a set of statistical models for the characterization of wind turbine wakes, including an analytical wake model for the near-wake region using the DG approach. However, the parameter for velocity deficit amplitude was not derived directly but was estimated using data fitting from the Doppler Lidar measurement instead. The other works have been dedicated to developing the analytical DG wake model [25]–[27]. However, none of those mentioned DG models explicitly consider the anisotropic behavior of wake expansion, which has been observed in the preliminary study of this study (Chapter 3). Furthermore, the anisotropic behavior of wake expansion is inevitable, particularly under different types of atmospheric stability [28].

### **Originality**

An anisotropic DG analytical wake model is proposed, thus facilitating its usability under varying atmospheric stability. Moreover, the additional empirical coefficient is added to the original formula of far-wake onset [29] to calculate the stream tube outlet position behind the utility-scale turbine instead of tuning. Meanwhile, the constant value of local Gaussian minima  $r_0$  for utility-scale turbines is suggested based on the evaluation of the root-mean-square error (RMSE).

#### ◆ **Chapter 5: A linear wake expansion function for the DG analytical wake model**

A linear wake expansion function is developed to enable the practical use of the DG wake model.

### **Background**

A key parameter of the wake expansion in the existing DG analytical wake models still has yet to be defined explicitly instead of tuning, thus limiting its usability for practical applications. It should be noted that the expansion parameter controls the wake recovery development and eventually determines the accuracy of the wake velocity field predicted by the analytical models. The conducted research aims to construct a physically-based linear wake expansion function for the DG model from the existing formulas based on the conservation of mass and momentum.

### **Originality**

Proposing a linear wake expansion function for the DG analytical model which can be used directly without tuning.

#### ◆ **Chapter 6: Analysis of multiple wakes behind HAWTs**

### **Background**

The wake flow field inside a wind farm is represented by the wake interactions between three aligned HAWTs. The LES result by FFB was used to analyze the wake flow field of the triple turbine case. In addition, the benchmark data from FFB was used to validate the analytical prediction of multiple wakes by the DG model employing the proposed expansion function.

### **Outcome**

This section implements the proposed wake expansion function for the DG analytical wake model to predict multiple wakes from three aligned HAWTs. Rotor-based Linear Sum was employed as a merging method of multiple wakes. The result shows the potential of the analytical DG model with the proposed expansion function to predict overlapping wakes between the turbines in a wind farm.

#### ◆ **Chapter 7: General discussion**

An overview of three sequential works is presented in this chapter.

#### ◆ **Chapter 8: Conclusion and future works**

This section summarizes the contributions of each research work conducted in this study, and the possible future works to address some limitations of the presented study are suggested.

## Chapter 2

### HAWT wake aerodynamics

#### 2.1 Wind velocity

The most basic measure of the wake is its mean velocity. The available wind velocity consists of streamwise, lateral, and vertical components. It is common to only consider the streamwise wake velocity component, where the velocity flows in the prevailing wind direction. For the sake of clarity, the streamwise velocity component in this text is denoted with the  $u$  letter. In the actual condition, the instantaneous streamwise velocity  $u$  including both the mean and turbulent components is given by:

$$u = U + u', \quad (2.1)$$

where  $U$  is the mean wind velocity and  $u'$  is fluctuating wind velocity. Note that the mean velocity  $U$  refers to the short-term mean wind speed, with the period  $\Delta t$  usually equal to ten minutes by the convention in wind energy engineering [30]. The short-term mean streamwise wind velocity  $U$  is the one most often employed in time series observations expressed as:

$$U = \frac{1}{\Delta t} \int_0^{\Delta t} u dt. \quad (2.2)$$

In practical applications, the instantaneous velocity is not measured continuously but is sampled with the interval  $\delta t$  at a number of samples  $N_s$ , such that  $\Delta t = N_s \delta t$ . Thus, the short-term mean wind velocity in the discrete form can be expressed as follows:

$$U = \frac{1}{N_s} \sum_{i=1}^{N_s} u_i. \quad (2.3)$$

Meanwhile, the root mean square of fluctuating wind velocity in the prevailing wind direction  $u_{rms} = \sqrt{u'u'}$ , is defined as the standard deviation of streamwise wind velocity  $\sigma_u$ , representing the turbulence strength. The ratio between the standard deviation of streamwise wind velocity to the mean streamwise wind velocity defines the streamwise turbulence intensity  $TI_u$ , given by:

$$TI_u = \frac{\sigma_u}{U}. \quad (2.4)$$

#### 2.2 Atmospheric boundary layer

The atmospheric boundary layer (ABL), also known as the planetary boundary layer, is the lowest layer of the atmosphere. Its characteristics are directly affected by the earth's surface characteristics, such as terrain types and vertical temperature distribution governing atmospheric stability. According

to atmospheric stability, which is defined as the tendency to resist vertical motion or to suppress existing turbulence [30], ABL can be classified into three types: neutral, stable, and unstable or convective [28].

The neutral boundary layer happens during relatively short transition periods after sunset or in windy conditions, where its mean vertical temperature distribution is approximately constant, and turbulence is mainly generated by shear around the surface. Meanwhile, the unstable boundary layer occurs during the daytime, when the surface is warmer than the air. The positive buoyance due to heat transfer between the surface and air heightens turbulence kinetic energy and the vertical transport of momentum, heat, and moisture. For the stable boundary layer, the surface cooling by longwave radiation to outer space damps the air to move upward. This stably stratified ABL normally happens at night, when turbulence is generated by shear and demolished by negative buoyancy and viscosity, causing weaker turbulence among the other atmospheric stability.

Another critical parameter for wind resources within the ABL is the vertical velocity profile or vertical wind shear, defined as wind speed variation with elevation. In general, the distribution of the vertical velocity profile in the mainstream directions for all atmospheric stability within the ABL is illustrated in Fig. 2.1.

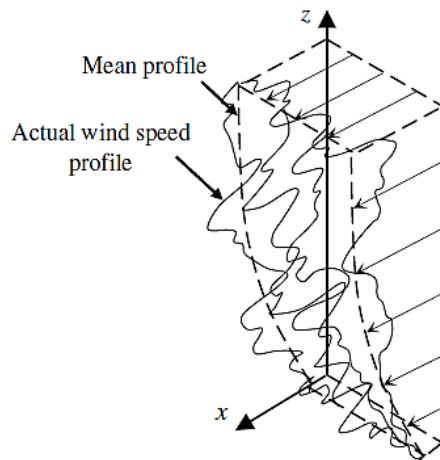


**Figure 2. 1.** An illustration of the vertical velocity profile in a streamwise direction within the ABL [31].

The mainstream wind velocity increases with height, representing vertical wind shear. In actual conditions, the ABL wind velocity at any position varies in time and direction around its mean value due to the turbulence effect, as illustrated by the actual wind speed profile in Fig. 2.1. Meanwhile, the variation of the ABL's velocity profile is strongly affected by atmospheric stability, terrain topography, and surface roughness.

The estimation of vertical wind shear is an important parameter for the HAWT designers since it affects the turbine output and lifespan, particularly the rotor component. There are two well-known approaches that have generally been used to model the mean ABL vertical velocity profile over

homogenous flat terrains: the logarithmic profile (log law) and the power law profile. The log law profile was derived from a combination of theoretical and empirical research. For the neutral stability condition, where the mean temperature profile within the ABL is approximately constant, the formulation for the vertical velocity profile is expressed as follows:

$$U(z) = U(z_r) \frac{\ln\left(\frac{z}{z_0}\right)}{\ln\left(\frac{z_r}{z_0}\right)}, \quad (2.5)$$

where  $U$  is the wind velocity (m/s) at the height  $z$  above the ground (m),  $U(z_r)$  is the wind velocity at the reference height  $z_r$ , and  $z_0$  is surface roughness. Note that  $U$  refers to the mean value where the turbulence effects have been averaged out. Some estimations of surface roughness length at various terrains are shown in Table 2.1.

**Table 2.1.** Estimations of surface roughness length at different terrains [32].

Type of terrain	Roughness length, $z_0$ (m)
Cities, forest	0.7
Suburbs, wooded countryside	0.3
Villages, countryside with trees and hedges	0.1
Open farmland, few trees, and buildings	0.03
Flat grassy plains	0.01
Flat desert, rough sea	0.001

Another approach is the power law profile, which represents a simple approach to model the mean of the vertical velocity profile, defined as follows:

$$U(z) = U(z_r) \left(\frac{z}{z_r}\right)^\alpha, \quad (2.6)$$

where  $\alpha$  is a power-law exponent and its value depends on terrain characteristics, as shown in Table 2.2.

**Table 2.2.** Estimations of power-law exponent  $\alpha$  at different terrain characteristics [33].

Terrain characteristics	Friction coefficient, $\alpha$
Smooth hard ground, calm water	0.10
Tall grass on level ground	0.15
High crops, hedges, and shrubs	0.20
Wooded countryside, many trees	0.25
Small town with trees and shrubs	0.30
Large city with tall buildings	0.40

In general, both approaches are widely used among researchers and project developers during the first stages of HAWT design for fatigue calculations and power production estimations from cyclic loads by the wind forces varying in the vertical direction exerted at the rotating blades.

### 2.3 HAWT blade aerodynamics

The aerodynamic forces on the HAWT blades can be represented by lift and drag forces acting on each blade element or section constructing the blades. Considering a two-dimensional airfoil with its aerodynamic characteristics at a specific angle of attack obtained from the relative wind velocity, the lift and drag forces can be calculated, and eventually, the axial load and torque at each blade section can be determined. Some assumptions apply for the method to be useful. Careful attention should be paid to the assumption that the spanwise velocity component is ignored, thus no aerodynamic interaction between the blade elements. A blade element sweeping out in an annular trajectory within a HAWT blade swept area is illustrated in Fig. 2.2.

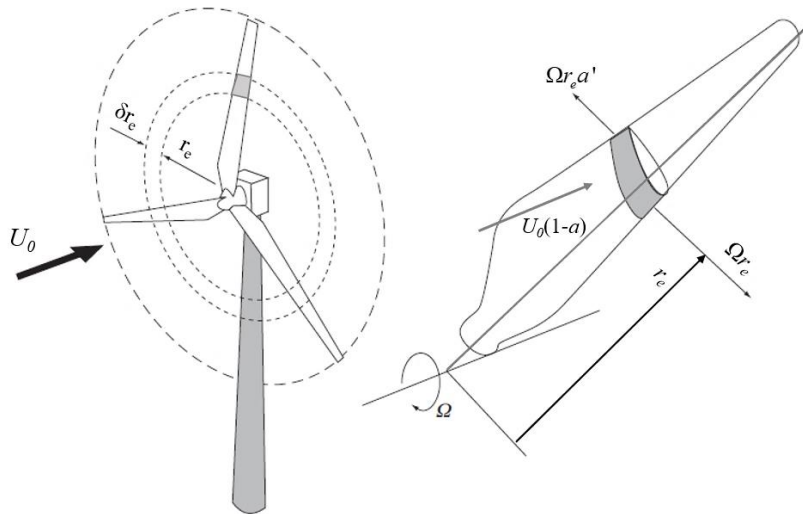


**Figure 2. 2.** Blade element at radius  $r_e$  with element radial length  $\delta r_e$  sweeping out in annular within a HAWT blade swept area [32].

The undisturbed wind velocity  $U_0$  reduced to  $U_0(1-a)$  at the rotor because of the axial induction factor  $a$ . Based on this wind velocity at the rotor and tangential velocity of the rotating HAWT blade, the wind velocity triangle and aerodynamic forces at each blade section can be drawn. The net tangential velocity experienced by the blade element at the radius  $r$  is the combination of the tangential velocity  $\Omega r$  and induced tangential velocity at the wake  $\Omega r a'$  due to the conservation of angular momentum. Thus, the net tangential velocity of the blade element at the radius  $r_e$  as shown in Fig. 2.2 is  $\Omega r_e(1+a')$ , where  $a'$  denotes the tangential induction factor for the tangential blade velocity. A more detailed of the two-dimensional wind velocity triangle and aerodynamic forces at each HAWT blade section or airfoil is shown in Fig. 2.3.

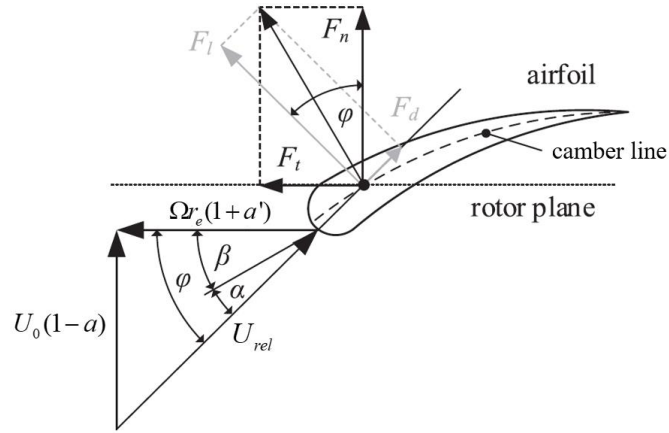


**Figure 2. 3.** Wind velocity triangle and aerodynamics forces at HAWT blade section (airfoil) [34].

Referring to the velocity triangle as shown in Fig. 2.3, the magnitude of relative wind velocity  $U_{rel}$  can be defined by incorporating the axial and tangential velocities at the blade section, given by:

$$U_{rel} = \sqrt{U_0^2(1-a)^2 + \Omega^2 r_e^2(1+a')^2} . \quad (2. 7)$$

Meanwhile, the angle of relative wind velocity to the rotor plane,  $\varphi$ , can be obtained using the trigonometric function. Then, the angle of attack can be defined as follows:

$$\alpha = \varphi - \beta . \quad (2. 8)$$

The optimal value of the blade twist angle  $\beta$  can be obtained iteratively by adjusting the angle of attack  $\alpha$  that gives the optimal ratio of lift coefficient ( $C_l$ ) to drag coefficient ( $C_d$ ) representing the aerodynamic performance characteristics of the selected airfoil at the section of interest. These airfoil characteristics can be obtained from the available look-up tables or by employing an external program such as XFOIL.

The lift force normal to the direction of  $U_{rel}$  on a blade element with a radial length  $\delta r_e$  is given by:

$$\delta F_l = \frac{1}{2} \rho U_{rel}^2 c C_l \delta r_e , \quad (2. 9)$$

where  $c$  is chord length. Meanwhile, the drag force parallel to  $U_{rel}$  is expressed as:

$$\delta F_d = \frac{1}{2} \rho U_{rel}^2 c C_d \delta r_e . \quad (2. 10)$$

Considering the  $B$  number of HAWT rotor blades, the axial load on the annular blade element having a radial length of  $\delta r_e$  within the rotor swept area is formulated as:

$$\delta F_n = \frac{1}{2} \rho U_{rel}^2 B c (C_l \cos \varphi + C_d \sin \varphi) \delta r_e , \quad (2. 11)$$

and the torque on the same blade element due to tangential force at the radius  $r_e$  from the blade center is formulated as:

$$\delta F_t = \frac{1}{2} \rho U_{rel}^2 B (C_l \cos \varphi + C_d \sin \varphi) c r_e \delta r_e, \quad (2.12)$$

where

$$\sin \varphi = \frac{U_0(1-a)}{U_{rel}} \quad \text{and} \quad \cos \varphi = \frac{\Omega r_e(1+a')}{U_{rel}}. \quad (2.13)$$

It should be kept in mind that the drag force reduces the torque and hence the power output of the HAWT but increases the blade axial loading.

## 2.4 One-dimensional momentum theory

The aerodynamic analysis of HAWT can be started without considering any detailed shape of rotor geometry but rather focused on the wind energy extraction process. This simplification is facilitated by the general device called an actuator disc with its permeable surface as a representation of the HAWT rotor and is described using the actuator disc model (ADM). In this model, the actuator disc is enclosed within a stream tube control volume which obeys the conservation of mass and momentum. The following conditions apply as basic assumptions in the ADM [30]:

- Homogenous, incompressible, steady-state flow;
- No frictional drag;
- An infinity number of blades;
- Uniform thrust over the actuator disc representing the rotor area;
- A non-rotating wake;
- The static pressure at far upstream and far downstream is equal to the undisturbed ambient static pressure.

When an incompressible time-invariant wind flow passes the stream tube control volume, pressure drop  $\Delta p$  occurs due to wind energy extraction by the actuator disc. As a result, the undisturbed wind  $U_0$  from the stream tube inlet section  $A_0$  slows down to  $U_d$  at the actuator disc section  $A_d$  and would be smaller to  $U_w$  at the wake section  $A_w$ , where the air pressure has regained its undisturbed value ( $p_w=p_0$ ). Considering the continuity equation in the steady state, the mass flow rate  $\dot{m}$  should be constant in each section of the control volume, thus yielding the following relation:

$$\dot{m} = \rho U_0 A_0 = \rho U_d A_d = \rho U_w A_w, \quad (2.14)$$

where  $\rho$  denotes the air density. Ensuring the conservation of mass in the continuity equation expressed in Eq. 2.14, the reduction of the undisturbed wind velocity  $U_0$  throughout the stream tube due to energy

extraction at the disc is compensated with the expansion area of the disc  $A_d$  and even more at the wake section  $A_w$ . This relation is illustrated in Fig. 2.4.

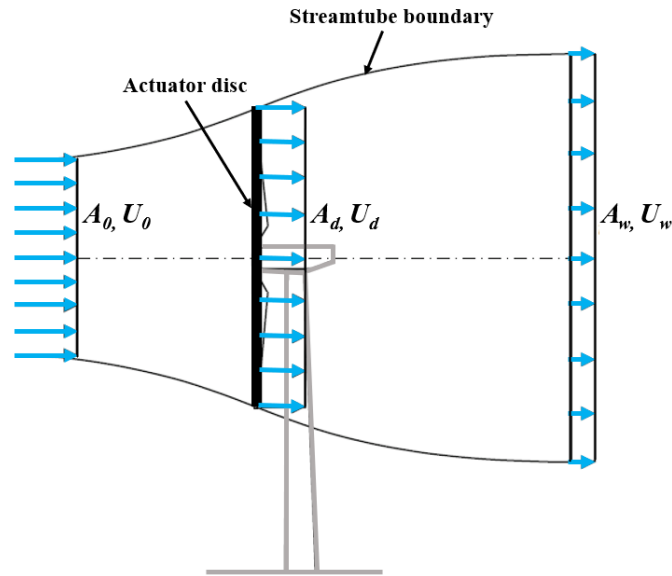


**Figure 2. 4.** Schematic of actuator disc model from the horizontal-axis wind turbine.

The wind energy extraction by the actuator disc causes an overall change in the air velocity within the stream tube control volume, which equals  $U_0 - U_w$ . Applying axial momentum balance, the rate of change of incoming momentum of the flow equals but opposite to the axial force exerted on the flow by the disc (thrust,  $T$ ):

$$T = \rho A_d U_d (U_0 - U_w). \quad (2. 15)$$

Since the flow is frictionless and no work is done on both sides of the disc, the Bernoulli equation in the front and behind of the disc can be applied to find the pressure drop across the disc using the following expression:

$$\Delta p = \frac{1}{2} \rho (U_0^2 - U_w^2). \quad (2. 16)$$

The fact that the thrust force  $T$  is equal to the pressure drop  $\Delta p$  over the disc area,  $T = \Delta p A_d$ , enables the expression for the air velocity at the disc  $U_d$  to be derived as follows:

$$U_d = \frac{1}{2} (U_0 + U_w). \quad (2. 17)$$

It is shown that the wind velocity at the disc is the mean of wind velocity at the inlet and outlet sections of the stream tube. Introducing the axial induction factor,  $a$ , as follows:

$$a = \frac{U_0 - U_d}{U_0}, \quad (2.18)$$

then substituted into Eq. 2.17, the streamwise velocity at the rotor disc and the wake can be written as follows:

$$U_d = U_0(1-a), \quad (2.19)$$

and

$$U_w = U_0(1-2a). \quad (2.20)$$

Substituting Eqs. 2.19 and 2.20 into the thrust formula in Eq. 2.15, the following equations for thrust can be obtained:

$$T = 2\rho A_d U_0^2 a(1-a). \quad (2.21)$$

Since power output based on the axial momentum balance is equal to  $P=TU_d$ , thus:

$$P = 2\rho A_d U_0^3 a(1-a)^2. \quad (2.22)$$

The performance characteristics of the turbine can be represented by the dimensionless power and thrust coefficients, respectively:

$$C_p = \frac{P}{\frac{1}{2}\rho A_d U_0^3}, \quad (2.23)$$

$$C_T = \frac{T}{\frac{1}{2}\rho A_d U_0^2}. \quad (2.24)$$

Employing the definitions of thrust  $T$  and power  $P$  in the Eqs. 2.21 and 2.22, a more compact term of power and thrust coefficients is given by:

$$C_p = 4a(1-a)^2, \quad (2.25)$$

$$C_T = 4a(1-a). \quad (2.26)$$

By differentiating the power coefficient against the axial induction factor, the maximum achievable value of power coefficient  $C_{pmax}$  is obtained when:

$$\frac{dC_p}{da} = 4(1-a)(1-3a) = 0, \quad (2.27)$$

that is achieved for  $a=1/3$ . Thus,

$$C_{P_{max}} = \frac{16}{27} = 0.593. \quad (2.28)$$

Hence, the value of the thrust coefficient giving the maximum power coefficient is as follows:

$$C_T = \frac{8}{9}.$$

The maximum theoretical value of the power coefficient  $C_{P_{max}}$  is known as the Betz limit after Albert Betz (1919) the German aerodynamicist. This  $C_{P_{max}}$  sets the upper limit for wind power extraction by an ideal rotor, which is no more than 59 %. Note that this maximum value doesn't include any mechanical and aerodynamic losses and therefore it represents a conservative upper maximum. Although there is no real turbine in such an ideal condition, this approach gives a reasonable estimation of the maximum wind energy that can be extracted by the real turbine.

Another important parameter for the HAWT design is the tip speed ratio (TSR),  $\lambda$ , which is defined as the ratio of blade tip velocity in the tangential direction to the undisturbed streamwise velocity.

$$\lambda = \frac{\Omega r_0}{U_0}, \quad (2.29)$$

where  $\Omega$  is rotational speed (rad/s) and  $r_0$  is rotor radius. Since  $C_P$  and  $C_T$  vary with the  $U_0$ , thus the turbine performance can be expressed as a function of the TSR.

## 2.5 Analytical modeling of HAWT wake

The ideal condition of wake aerodynamics behind a single turbine can be modeled by a streamtube control volume approach. The wind turbine rotor is represented as a permeable disc within a cylindrical control volume where the airflow comes from the inlet section with the undisturbed velocity  $U_0$  and exits with the wake velocity  $U_w$  where the pressure has regained its freestream level. The illustration of this streamtube approach for single wake aerodynamics is shown in Fig. 2.5.

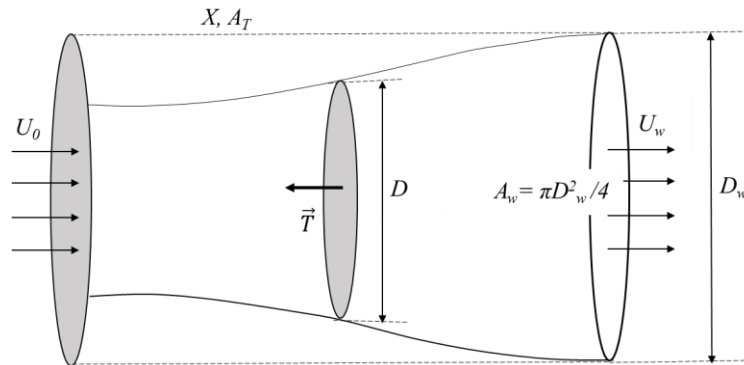


**Figure 2.5.** Cylindrical control volume around a wind turbine rotor with the surface area  $A_T$  and volume  $X$  [22].

By referring to Frandsen et al. [22], the momentum equation in vector form for the flow within the streamtube control volume with the volume  $X$  and surface area  $A_T$  is expressed as:

$$\int_X \rho \frac{\partial \vec{U}_w}{\partial t} dX + \int_{A_T} \rho \vec{U}_w (\vec{U}_w \cdot d\vec{A}_w) = - \int_{A_T} p d\vec{A}_w + \int_X \rho \vec{g} dX + \vec{T} + \int_{A_T} \vec{\tau} dA_w. \quad (2.30)$$

Suppose the acceleration term (first left-hand side), the pressure term (first right-hand side), the gravity term (second right-hand side), and the turbulent shear forces in the cylinder surface (the last term on the right-hand side) are neglected, and assume that the pressure downstream has regained to its freestream level. In that case, the following relation can be obtained for the wake aerodynamics behind a single turbine rotor by applying the conservation of mass and momentum:

$$T = \int_{A_w} \rho U_w (U_0 - U_w) dA_w, \quad (2.31)$$

where  $T$  is the total force over the rotor, which can be formulated as follows:

$$T = \frac{1}{2} C_T \rho A U_0^2, \quad (2.32)$$

where  $A$  is the rotor-swept area. Eq. 2.31 is a starting point for developing an analytical wake model. Next, the normalized velocity deficit within the wake region,  $\Delta U/U_0$ , using self-similarity assumption can be defined as:

$$\frac{\Delta U}{U_0} = \frac{U_0 - U_w}{U_0} = C(x) f(r, \sigma(x)), \quad (2.33)$$

where  $C(x)$  denotes the maximum velocity deficit at each downstream position  $x$ ,  $f(r, \sigma(x))$  represents the shape function which determines the spatial shape of the deficit along the radial distance  $r$  at the distance  $x$  downstream of the turbine. By inserting Eqs. 2.33 and 2.32 into Eq. 2.31, the physically based wake velocity profile downstream of the turbine, either by using the top-hat or Gaussian shape distribution, can be derived accordingly.

An overview of some analytical wake models, which become the pioneers for number of recently developed analytical models considering conservation law, is briefly described in the following subsections.

### 2.5.1 Top-hat wake model

One of the pioneering works in analytical wake modeling is the Jensen model, which is acknowledged as the industry standard model for simulating wake-induced velocity deficit behind HAWT with its simple top-hat approach [20], [21]. The wake velocity deficit is considered constant within the wake region and expanded linearly with the downstream distance. The simplification of the

top-hat approach was justified because the model aimed to give an estimate of the energy content in the wind seen by the downstream turbines, rather than to accurately estimate the velocity field. A schematic of the top-hat velocity profile behind a HAWT is shown in Fig. 2.6.

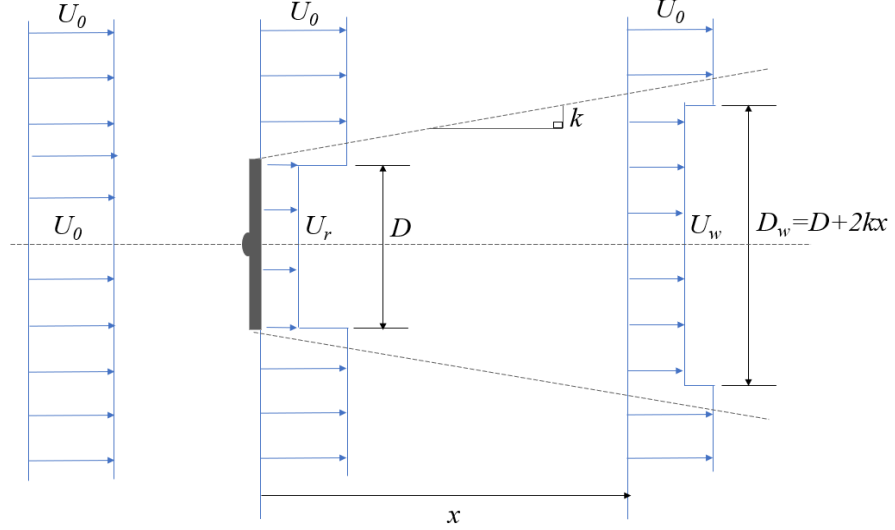


**Figure 2. 6.** Schematic of top-hat wake velocity profile behind a HAWT.

Considering the conservation law, a balance of momentum from the region just behind the rotor and within the wake area gives the following relation:

$$D^2 U_r + (D_w^2 - D^2) U_0 = D_w^2 U_w, \quad (2.34)$$

where  $U_0$  denotes the undisturbed velocity,  $U_r$  is the wake velocity just behind the rotor equals to  $U_r = (1 - 2a)U_0$ , and its area is assumed to be equal to rotor diameter  $D$ ,  $U_w$  is the wake velocity with the diameter  $D_w$ . Assuming the linear wake expansion with the distance  $x$  downstream of the turbine and applying wake decay constant  $k$ , the wake diameter can be defined as  $D_w = D + 2kx$ . By substituting  $D_w$  and  $U_w$  formulas into Eq. 2.34, the normalized wake velocity considering the top-hat approach at a given downstream position  $x$  is:

$$\frac{U_w}{U_0} = 1 - \frac{2a}{\left(1 + \frac{2kx}{D}\right)^2}, \quad (2.35)$$

where  $a$  is the axial induction factor defined as the function of thrust coefficient  $C_T$  by:

$$a = \frac{1 - \sqrt{1 - C_T}}{2}. \quad (2.36)$$

Another top-hat approach for the analytical wake model was also proposed by Frandsen et al. by considering the conservation of mass and momentum [22]. Although this model could give a practical

solution for the wake velocity field prediction, the issue arises since the energy content from the wind is the cube of the wind velocity. Thus, little discrepancies resulting from the top-hat assumption could result in the wrong prediction of the actual wake flow field, which eventually could cause errors in the prediction of the power output of the downstream turbines and overall production of the wind farm.

### 2.5.2 SG wake model

An SG wake model approach was proposed based on the actual representation of the wake distribution within the far-wake region by Bastankhah and Porte-Agel, abbreviated as the BPA model [5]. The model was derived by considering the conservation of mass and momentum and using self-similarity and axis-symmetric assumptions centered at the rotor axis. An illustration of the wake development behind a HAWT using the SG wake model is shown in Fig. 2.7.

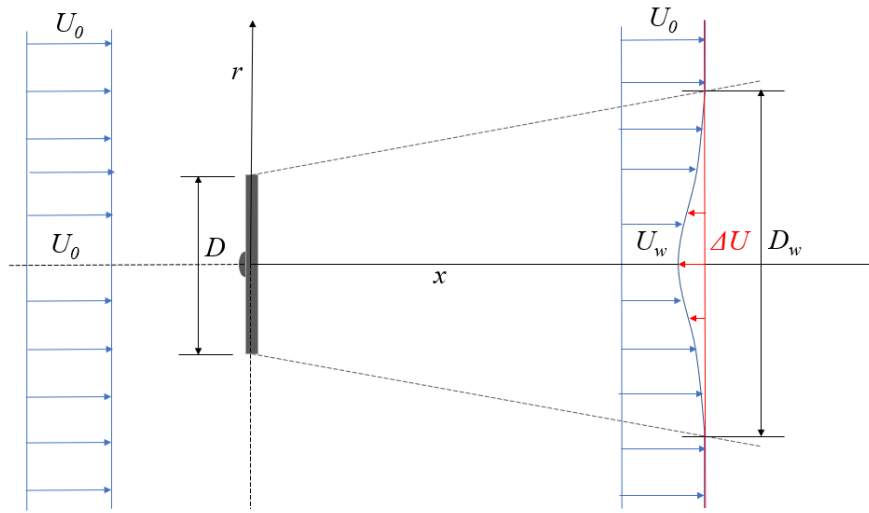


**Figure 2. 7.** Illustration of wake development behind a HAWT using SG analytical wake model.

Applying the single-Gaussian (SG) spatial distribution at the radial position  $r = \sqrt{y^2 + (z - z_{hub})^2}$  from the axis in Eq. 2.33, the SG velocity deficit profile is expressed as follows:

$$\frac{\Delta U}{U_0} = C(x)e^{-\frac{r^2}{2\sigma^2}}, \quad (2.37)$$

where  $\sigma$  is the standard deviation of SG velocity deficit profile as a function of the downstream distance  $x$  from the turbine. Then, the normalized wake velocity is given by:

$$U_w = U_0(1 - C(x)e^{-\frac{r^2}{2\sigma^2}}). \quad (2.38)$$

By inserting Eqs. 2.38 and 2.37 into Eq. 2.31 and integrating from 0 to  $\infty$ , a physically acceptable solution for the maximum velocity deficit at each downstream distance from the rotor is obtained as follows:

$$C(x) = 1 - \sqrt{1 - \frac{C_T}{8(\sigma/D)^2}}. \quad (2.39)$$

Meanwhile, the standard deviation of the SG profile which defines the wake expansion is defined as follows:

$$\sigma(x) = k^* x + \varepsilon D, \quad (2.40)$$

where  $k^*$  is the wake decay coefficient, and  $\varepsilon$  is the wake expansion at  $x=0$  defined as:

$$\varepsilon = 0.2\sqrt{\beta}, \quad (2.41)$$

where  $\beta$  is given by:

$$\beta = \frac{1}{2} \frac{1 + \sqrt{1 - C_T}}{\sqrt{1 - C_T}}.$$

Finally, the proposed form of normalized wake velocity which expands radially at the downstream distance  $x$  is formulated as follows:

$$\frac{U_w}{U_0} = 1 - \left[ \left( 1 - \sqrt{1 - \frac{C_T}{8(k^* x/D + \varepsilon)^2}} \right) \times \exp \left( - \frac{1}{2(k^* x/D + \varepsilon)^2} \left\{ \left( \frac{z - z_{hub}}{D} \right)^2 + \left( \frac{y}{D} \right)^2 \right\} \right) \right]. \quad (2.42)$$

It should be noted that Eq. 2.42 assumes the linear and isotropic wake expansion, which later was modified by Xie and Archer [6] by considering the anisotropic nature of the wake expansion thus allowing its usability under different atmospheric stability [28]. However, the SG-based model is only suitable within the far-wake region where the wake distribution shows self-similarity behavior of the SG wake shape.

### 2.5.3 DG wake model

Wind-tunnel, field, and numerical measurement results show that within the near-wake region, the average wake velocity tends to form the DG distribution. This fact inspired the development of Keane's model [25], which later was corrected by Schreiber et al. [26], to predict the wake velocity profile for all distances downstream of the turbine, by assuming the DG approach for the velocity distribution within the wake region. An illustration of the wake development behind a HAWT using the DG approach is shown in Fig. 2.8.

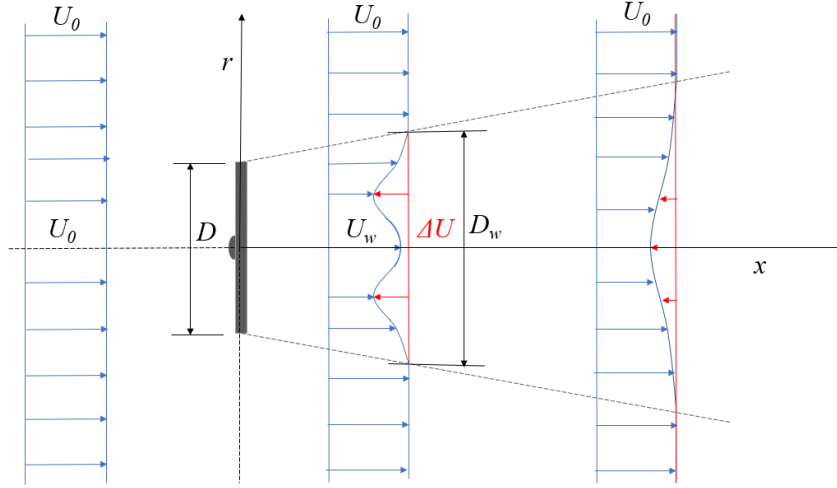


**Figure 2.8.** Illustration of the wake development behind a HAWT using the DG analytical wake model.

Applying conservation of mass and momentum, the DG shape of velocity within the near wake region evolves downstream the turbine, causing two local minima around the blade mid-span to shift towards the centerline within the far-wake distance thus forming the SG velocity profile. As a result, an estimation of wake velocity distribution within the full-wake region, which consists of the near and far-wake regions, could be produced.

In the DG model, the basic equation for the normalized velocity deficit  $\Delta U/U_0$  uses Eq. (2.33), and the wake aerodynamics behind a HAWT for deriving the DG velocity deficit amplitude function  $C(x)$  follows Eq. (2.31). Firstly, the wake shape function  $f(r, \sigma(x))$  for the DG distribution is defined as:

$$f(r, \sigma(x)) = \frac{1}{2} \left( e^{D^{G^+}} + e^{D^{G^-}} \right), \quad (2.43)$$

where

$$D^\pm = \frac{-(r \pm r_0)^2}{2\sigma^2(x)}.$$

By inserting Eqs. 2.43 and 2.32 into Eq. 2.31 and integrating from 0 to  $\infty$ , a physically acceptable solution for the amplitude function of the DG velocity deficit  $C(x)$  at the distance  $x$  downstream of the rotor is obtained as follows:

$$C(\sigma(x)) = \frac{M - \sqrt{M^2 - 1/2 N C_T D^2}}{2N}, \quad (2.44)$$

where

$$M = 2\sigma^2 e^{\frac{-r_0^2}{2\sigma^2}} + \sqrt{2\pi} r_0 \sigma \operatorname{erf} \left( \frac{r_0}{\sqrt{2}\sigma} \right),$$

and

$$N = \sigma^2 e^{\frac{-r_0^2}{\sigma^2}} + \frac{\sqrt{\pi}}{2} r_0 \sigma \operatorname{erf}\left(\frac{r_0}{\sigma}\right).$$

Meanwhile, the wake expansion function is given by:

$$\sigma(x) = k^*(x - x_0) + \varepsilon_{DG}, \quad (2.45)$$

where  $\varepsilon_{DG}$  is the initial wake expansion at the unknown downstream distance  $x_0$  and  $k^*$  is the wake expansion rate. To derive  $\varepsilon_{DG}$ , mass conservation between the Betz streamtube obtained by Frandsen's model [22] and the DG model is enforced, resulting in the following relation:

$$\frac{D^2 \beta}{8} \left(1 - \sqrt{1 - \frac{2}{\beta} C_T}\right) = M(\varepsilon_{DG}) \frac{M(\varepsilon_{DG}) - \sqrt{M(\varepsilon_{DG})^2 - 1/2 N(\varepsilon_{DG}) C_T D^2}}{2N(\varepsilon_{DG})}. \quad (2.46)$$

Eq. 2.46 needs to be solved numerically to obtain the value of  $\varepsilon_{DG}$ . Finally, the formulation of normalized wake velocity behind a HAWT considering the DG approach is given by:

$$\frac{U_w}{U_0} = 1 - \left( \frac{M - \sqrt{M^2 - 1/2 N C_T D^2}}{2N} \times \frac{1}{2} \left( e^{DG^+} + e^{DG^-} \right) \right). \quad (2.47)$$

The development of the DG-based analytical wake model has shown its effectiveness to predict the velocity distribution within a full-wake region, as shown by Schreiber et al [26]. However, its usability is still quite challenging since the values for the radial position of local minima  $r_0$ , the wake expansion rate  $k^*$ , and the downstream position of initial wake expansion  $x_0$  need to be tuned by case.

## Chapter 3

# Investigation of the near-wake behavior of an isolated HAWT

### *Attribution*

*Q. M. B. Soesanto, T. Yoshinaga, and A. Iida, "Investigation of the near-wake behavior of an isolated horizontal-axis wind turbine," The 9<sup>th</sup> International Conference on Sustainable Energy Engineering and Applications (ICSEEA 2021), Online, pp.1-9, October 2021.*

### 3.1 Overview

This study investigates the near-wake flow behavior of an isolated NREL 5 MW horizontal-axis wind turbine (HAWT). Time-averaged streamwise wake velocity distribution resulting from high-fidelity large eddy simulation (LES) result was analyzed to study the wake evolution and distribution in the lateral and vertical directions. It was observed that the induction zone upstream of the turbine gradually reduced the incoming velocity due to the blockage effect of the rotating rotor. Meanwhile, the contour of streamwise velocity from the LES result shows that the streamwise inflow velocity significantly reduced within the near-wake region downstream of the turbine. In addition, the magnitude of velocity deficit was higher around the blade mid-span than its surroundings. This study employed the double-Gaussian (DG) function to represent the wake shape distribution within the near-wake region. In addition, the single-Gaussian (SG) function was also included for comparison.

It was clarified from the LES results that the wake distribution in both lateral and vertical directions within the near-wake region tends to form a DG shape, thus confirming the suitability of the DG function. Furthermore, it was found that the laminar inflow condition slowed down the turbulence mixing from the wake boundary to the centerline, thus resulting in a slow wake recovery. In the analyzed LES data, the wake recovery rates in both lateral and vertical directions are likely to increase with the downstream distance. The difference in the mean velocity between both directions was more significant as the downstream distance increased. It means the wake recovery tends to have a linear relationship with the downstream distance. Moreover, the wake tends to recover in an anisotropic way in which the wake recovery rate in the vertical direction is less than in the lateral direction. Hence, for analytical wake modeling, it is recommended to consider the DG shape function with anisotropic expansion for better accuracy of streamwise velocity prediction within the near-wake region

### 3.2 Introduction

The offshore wind power plant, commonly called a wind farm, offers great potential to become the main energy player for supplying energy demand worldwide [35]. However, current challenges still exist regarding the comprehensive understanding of the aerodynamic aspects of offshore wind farms. Therefore, further investigations are needed, particularly to accurately predict the wake behavior downstream of the turbines.

A wind turbine wake is defined as a plume-like region behind the wind turbine, identified by reduced wind speed and increased turbulent intensity [12]. Hence, any turbine placed inside this wake region will experience power losses and increased mechanical stresses [36]. In addition, the high turbulence intensity resulting from the rotating blades complicates the flow field inside the wake region. Therefore, it can cause interference in the downstream turbine performance. Despite the complex flow behavior inside the wake region, it was found that the streamwise velocity profile within this wake region has self-similarity characteristics, which tend to follow Gaussian shape distribution [1], [37], [38]. This discovery becomes a steppingstone among researchers to develop analytical wake models that consider the Gaussian shape distribution, particularly for predicting the streamwise velocity within the far wake region [5], [6], [39].

Much research has been carried out to elucidate the wake flow behavior using experimental measurement, CFD simulation, or analytical wake modeling. Nevertheless, a detailed investigation, particularly within the near-wake region, has received less attention which may be caused by the complex flow field inside this region and micro-siting of wind turbines commonly located within the far-wake region. Conversely, improved knowledge of wake development may lead to more efficient wind farm layouts [40]. Thus, a better understanding of the wake behavior, including within the near-wake region, becomes imperative.

This study investigates the wake flow behavior within a near-wake region behind an isolated full-scale NREL 5 MW HAWT. The three-dimensional CFD simulation data of time-averaged streamwise wake velocity from the last five revolutions were processed and analyzed. Some near-wake characteristics which were identified previously are also clarified in this study. In addition, a detailed wake shape distribution and its recovery are highlighted and discussed.

### **3.3 Methodology**

#### **3.3.1 Wind Turbine Modeling**

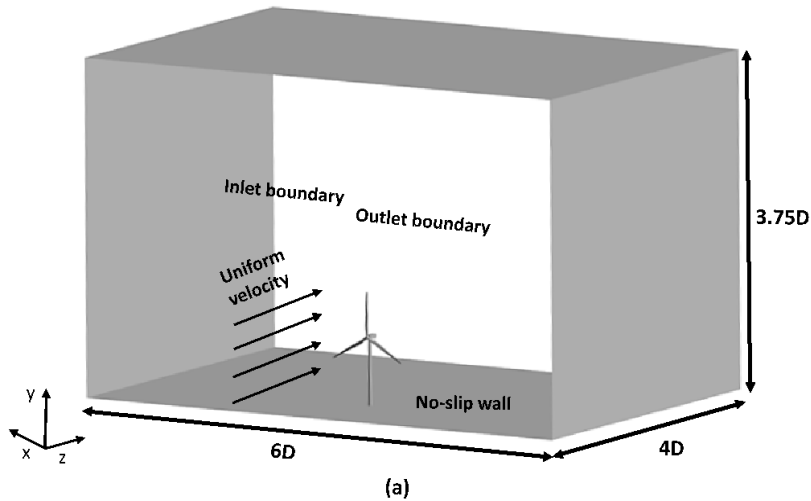
A wind turbine model used in this study is NREL 5 MW reference offshore HAWT [41]. The turbine's rotor contains three blades that rotate around the horizontal-axis. The main parts of the turbine, such as the nacelle and tower, were also included in the simulation. Therefore, a realistic flow field might be obtained, particularly within the near-wake region. Since only fluid flow simulation is of interest in the present study, thus the structural response, the blade cone, and shaft tilt angles as specified in the reference turbine are neglected. Further details of the turbine geometry and its rated conditions are tabulated in Table 3.1.

**Table 3. 1.** Specifications of NREL 5 MW offshore HAWT.

Parameter	Value
Rated power, $P$	5 MW
Reference wind speed, $U_0$	11.4 m/s
Rotational speed, $\omega$	12.1 rpm
Tip speed, $U_{tip}$	80 m/s
Tip speed ratio, $TSR$	7
Rotor diameter, $D$	126 m
Rotor configuration	3 blades
Hub diameter, $D_H$	3 m
Hub height	95 m

### 3.3.2 Numerical schemes

The turbine modeling contains the main turbine components, i.e., rotor, nacelle, and tower. A direct approach for rotor modeling was used to capture the flow structures around the blade and might give a realistic wake flow downstream of the turbine. Without considering atmospheric wind shear and inflow turbulence at the inlet boundary, incoming streamwise velocity was uniformly distributed at the inlet. The free boundary, where the pressure is assumed to be zero, was defined on the domain's outlet. The no-slip condition was set on the bottom of the domain and the surface of the turbine's stationary components. Structured hexahedral meshes were used within the entire domain. Fig. 3.1 illustrates the related domain and boundary condition of the simulation.



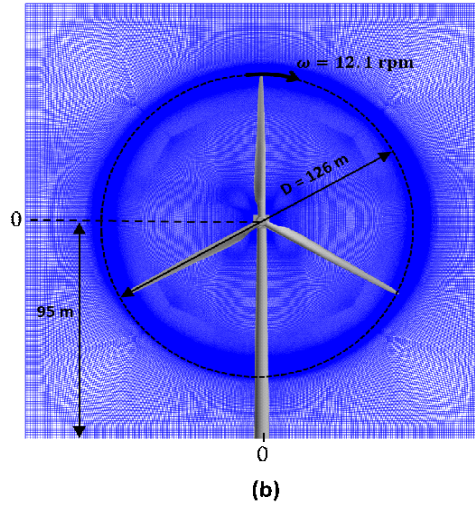


**Figure 3. 1.** Computational domain (375960278 hexahedral elements) of the turbine simulation: (a) domain size and the boundary conditions; (b) wind turbine dimension with the background of structured hexahedral mesh at  $0.5D$  behind the turbine.

In this study, the three-dimensional flow field around the turbine was simulated using the non-commercial CFD solver FrontFlow/blue (FFB). The solver uses the finite element method (FEM) to numerically solve the unsteady incompressible Navier-Stokes (NS) equations in cartesian coordinates. A moving boundary interface was set to calculate the interaction between rotating and stationary regions inside the computational domain via overset mesh approach within multiple frames of reference. This approach ensures that the flow field interaction between rotating and stationary regions can be solved using an appropriate margin of overlapping meshes. A fully implicit method from the Crank-Nicholson scheme was used for the temporal discretization of the momentum equation, yielding second-order accuracy in time. Moreover, the fractional step method solved the Poisson equation for pressure. The spatial and temporal characteristics of turbulence flow were calculated using the large eddy simulation (LES) turbulence model.

### 3.3.3 LES turbulence modeling

Rather than use time-averaging, LES uses a spatial filtering on the continuity and Navier-Stokes (NS) equations which is denoted by the overbar  $\overline{(\ )}$  at the grid-filter width  $\Delta$ . In the present study, the airflow is assumed to be incompressible. Thus, the continuity and NS equations for LES approach can be reformulated as follows:

$$\frac{\partial \overline{u}_i}{\partial x_i} = 0, \quad (3.1)$$

$$\frac{\partial \overline{u}_i}{\partial t} + \frac{\partial}{\partial x_j} (\overline{u}_i \overline{u}_j) = -\frac{1}{\rho} \frac{\partial \overline{p}}{\partial x_i} + \nu \frac{\partial^2 \overline{u}_i}{\partial x_j \partial x_j} - \frac{\partial \tau_{ij}}{\partial x_j}. \quad (3.2)$$

Sub grid scale (SGS) stresses,  $\tau_{ij}$ , mainly due to the interactions between unresolved or SGS eddies, is given by

$$\tau_{ij} = \overline{u_i u_j} - \bar{u}_i \bar{u}_j. \quad (3.3)$$

The effect of these whole stresses  $\tau_{ij}$  on the resolved flow needs to be modeled by means of SGS turbulence model.

A closure from Smagorinsky model, which is based on isotropic eddy-viscosity, is employed to determine the SGS stresses via SGS eddy viscosity,  $\nu_{SGS}$ , and resolved strain-rate tensor,  $\bar{S}_{ij}$ , using the following correlations:

$$\tau_{ij} - \frac{1}{3} \tau_{kk} \delta_{ij} = -2\nu_{SGS} \bar{S}_{ij}, \quad (3.4)$$

$$\nu_{SGS} = (C_S \Delta)^2 |\bar{S}|, \quad (3.5)$$

$$\bar{S}_{ij} = \frac{1}{2} \left( \frac{\partial \bar{u}_i}{\partial x_j} + \frac{\partial \bar{u}_j}{\partial x_i} \right), \quad (3.6)$$

$$|\bar{S}| = \sqrt{2\bar{S}_{ij}\bar{S}_{ij}}, \quad (3.7)$$

$$\Delta = \sqrt[3]{\Delta_x \Delta_y \Delta_z}. \quad (3.8)$$

In the original Smagorinsky model, the constant  $C_S$  is a user-prescribed constant. However, from a practical standpoint, there is no universal value of  $C_S$  which can be applied to a wide range of flow. Therefore, the dynamic Smagorinsky model (DSM), which allows to dynamically compute the local values of the model constant  $C_S$  as a function of time and space based on the resolved flow, is adopted in this study.

### 3.3.4 The DG function for the near-wake flow field prediction

To elucidate the complex behavior of the wind turbine's wake, averaging data of the flow field is essential to give an insight into the wake flow behavior and its development downstream of the turbine. In general, the streamwise velocity within the near-wake region is dominated by the effect of turbine geometry, particularly the rotor shape. In this study, the spreads of the normalized streamwise velocity data points averaged from the last five revolutions resulting from LES were fitted with the Gaussian functions. The equations of the normalized streamwise velocity for the DG function in the lateral and vertical directions at each downstream distance to fit with the respective LES data are formulated in Eqs. (3.9) and (3.10), respectively.

$$\frac{U_{DG-fit,ltr}}{U_0} = 1 - \left( \frac{A_{DG,ltr}}{2} \left( \exp \left[ -\frac{(x+R_l)^2}{2\sigma_{DG,ltr}^2} \right] + \exp \left[ -\frac{(x-R_r)^2}{2\sigma_{DG,ltr}^2} \right] \right) \right), \quad (3.9)$$

$$\frac{U_{DG-fit,ver}}{U_0} = 1 - \left( \frac{A_{DG,ver}}{2} \left( \exp \left[ -\frac{(y+R_b)^2}{2\sigma_{DG,ver}^2} \right] + \exp \left[ -\frac{(y-R_a)^2}{2\sigma_{DG,ver}^2} \right] \right) \right). \quad (3.10)$$

In addition, the SG function, which is commonly used in analytical wake modeling to represent the wake distribution within the far-wake region, was also added for comparison. The equations of the normalized streamwise velocity for the SG function in the lateral and vertical directions at each downstream distance to fit with the respective LES data are expressed in Eqs. (3.11) and (3.12), respectively.

$$\frac{U_{SG-fit,ltr}}{U_0} = 1 - \left( A_{SG,ltr} \exp \left[ -\frac{(x+x_c)^2}{2\sigma_{SG,ltr}^2} \right] \right), \quad (3.11)$$

$$\frac{U_{SG-fit,ver}}{U_0} = 1 - \left( A_{SG,ver} \exp \left[ -\frac{(y+y_c)^2}{2\sigma_{SG,ver}^2} \right] \right), \quad (3.12)$$

where subscripts *DG*, *SG*, *ltr*, and *ver* denote double-Gaussian, single-Gaussian, lateral and vertical directions, respectively. *A* is the amplitude of the Gaussian, *x* and *y* are the lateral and vertical distances from the wake center, respectively. *R<sub>l</sub>*, *R<sub>r</sub>*, *R<sub>a</sub>* and *R<sub>b</sub>* are the left, right, above, and bottom positions of the DG local minima, respectively.

For the SG function, the centerline positions *x<sub>c</sub>* and *y<sub>c</sub>* are equal to zero. Meanwhile, *σ* denotes the standard deviation of the Gaussian velocity deficit at each direction and downstream distance. In this study, the unknown parameters of *A*, *R*, and *σ* need to be optimized iteratively starting from the initial guess using appropriate criteria so that the generated Gaussian velocity profile could give the best fit against the respective CFD data. The Nelder-Mead simplex algorithm with some modifications to include bound and inequality constraints was employed using MATLAB optimization function *fminsearchcon* [42].

### 3.3.5 Objective Function

In this study, the objective function aims to minimize residuals or differences between the LES data and their Gaussian estimations. The root-mean-square error (RMSE) statistical model was used for this purpose. The objective function formulations for the DG and SG functions in the lateral direction are expressed using Eqs. (3.13) and (3.14), respectively.

$$\text{minimize: } \sqrt{\left(\frac{U_{CFD,lat}}{U_0} - \frac{U_{DG-fit,lat}}{U_0}\right)^2}, \quad (3.13)$$

$$\text{minimize: } \sqrt{\left(\frac{U_{CFD,lat}}{U_0} - \frac{U_{SG-fit,lat}}{U_0}\right)^2}. \quad (3.14)$$

The same equations apply to calculate the objective functions for the DG and SG functions in the vertical direction by substituting subscript *lat* in Eqs. (3.13) and (3.14) with *ver*.

### 3.4 Results and discussion

#### 3.4.1 The Wake Centerline

The axial profile of centerline velocity ( $x = 0, y = 0$ ) from the inlet to the outlet of the domain is shown in Fig. 3.2. Interaction between the rotor and the incoming velocity was observed just after the domain inlet, starting about  $z/D \approx 0.9$  upstream of the turbine. The interaction was getting intense within the upstream induction zone near the rotor, where the reference wind speed  $U_0$  slowing down significantly due to the blockage effect of the rotating rotor.

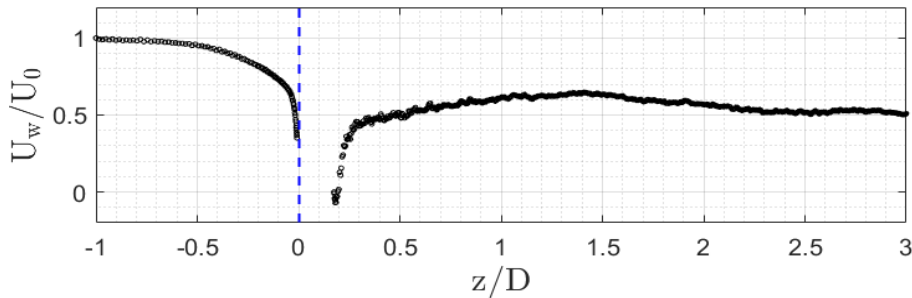


**Figure 3. 2.** The centerline velocity at the hub height along the axial direction. The Blue dashed line shows the axial position of the rotor.

After nacelle blockage became insignificant, the wake centerline velocity increased exponentially, observably starting from  $z/D \approx 0.2$  until  $z/D \approx 0.3$ . Afterward, the velocity gradually increased until  $z/D \approx 1.4$ . This occurrence indicates that the upstream flow around the hub that already passed through the rotating blade has reached the centerline and mixed with its surroundings, thus speeding up the centerline velocity.

At the remaining distance, the velocity field around the hub height was more dominated by the wake effect resulting from the rotor. However, as the downstream distance further increased, the wake recovery on the centerline profile was relatively slow. It might be owing to the laminar inflow condition upstream of the turbine. As a result, the turbulence mixing from the wake boundary to the centerline came about gradually, thus resulting in a slow wake recovery. A longer downstream distance would be

needed for the wake centerline to regain its undisturbed condition, which is beyond the domain dimension of the conducted simulation.

### 3.4.2 Contour of streamwise velocity

The contours of streamwise velocity from the center of vertical and horizontal sections are shown in Figs. 3.3(a) and 3.3(b), respectively. It was observed clearly in both views that the inflow velocity significantly diminished within the near-wake region downstream of the turbine. By referring to the normalized velocity color bar, the magnitude of velocity deficit tends to be higher around the blade mid-span than its surroundings, which means that the DG velocity profile is formed.

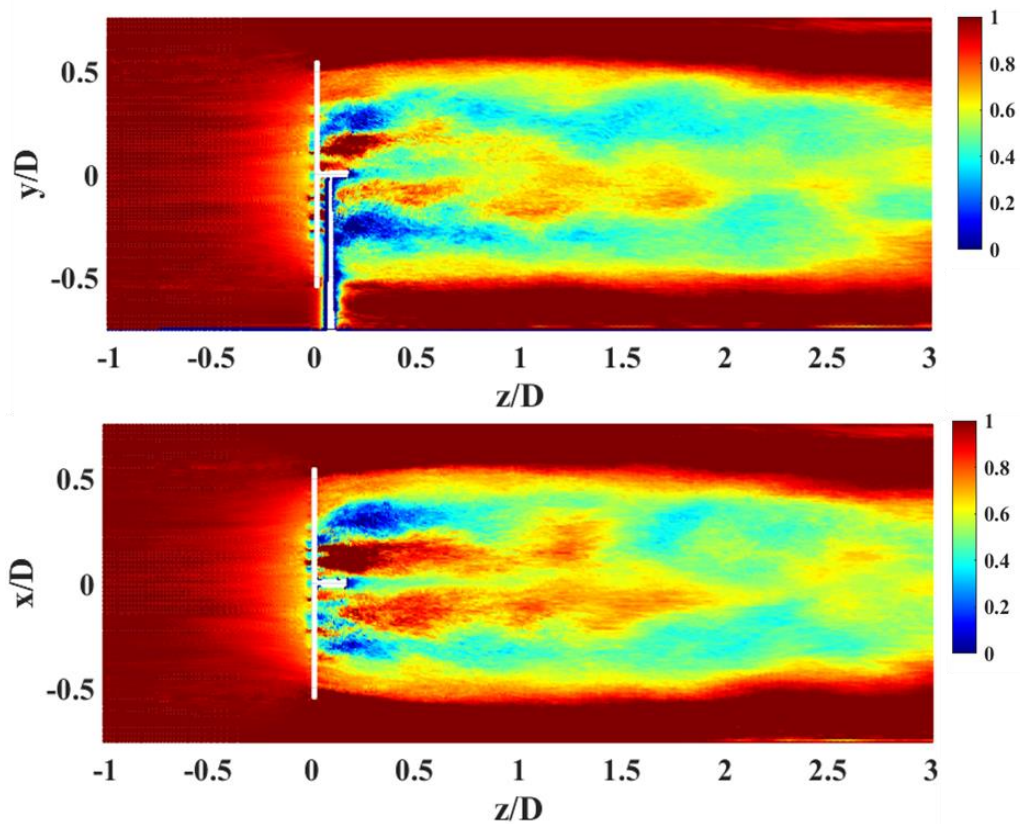


**Figure 3. 3.** The contour of normalized streamwise wake velocity: (a) side view ( $x = 0$ ); (b) top view ( $y = 0$ ).

From both views, a shear layer was observed around the blade tip position. This occurrence could represent the wake boundary, where the transition between the freestream inflow to the wake region occurs. Further description is depicted in Fig. 3.4, showing the contours of cross-sectional wake velocity within the near-wake region resulting from the high-fidelity LES.

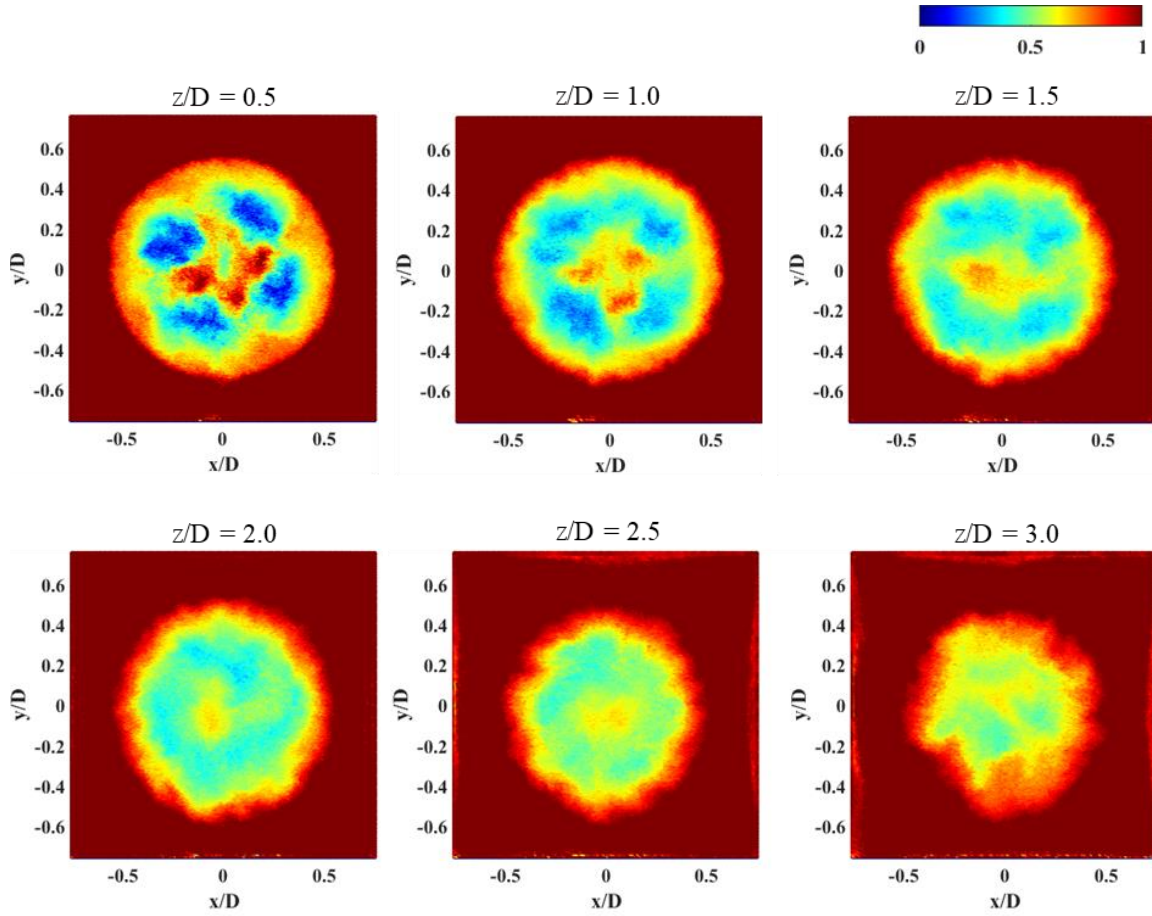


**Figure 3. 4.** The contour of normalized cross-sectional wake velocity at several downstream distances within the near-wake region.

It is shown from the cross-sectional wake areas that the velocity contours around the wake axis are relatively higher than their surroundings around the blade mid-span. It indicates the DG wake shape has formed, where the significant velocity deficit around the blade mid-span gradually weakened as the wake recovered at further downstream distances. To get more details regarding the wake characteristics, the wake profile distributions from the LES result will be further analyzed in the following sections.

### 3.4.3 Streamwise velocity in the vertical direction

Streamwise wake velocity in the vertical direction at several downstream distances is shown in Fig. 3.5. The results from the SG distribution fit were added for comparison. The DG fit generally has better accuracy for wake distribution prediction at each evaluated distance within the near-wake region. The suboptimal shape of the blade root and the resulting tip vortices around the blade tip leads to a less significant velocity deficit around these regions [2], [24]. Conversely, the optimum lift generated around the blade midspan makes a significant velocity deficit about this position. Thus, generating two local minima in both lateral and vertical directions around the blade midspan. As a result, the DG profile of the streamwise wake velocity is formed within the near-wake region. The scatter plots of the normalized wake velocities from the LES data clearly support this bimodal distribution behavior.

At  $z/D = 0.75$ , two local minima of the velocity appear around the blade mid-span, and the salient velocity deficit can be observed just above the centerline due to the remaining influence of the hub blockage. At a further downstream distance, the velocity around the hub height underwent less deficit than the previous downstream location, thus creating a more ideal shape of DG distribution, observably starting from  $z/D = 1.25$ .

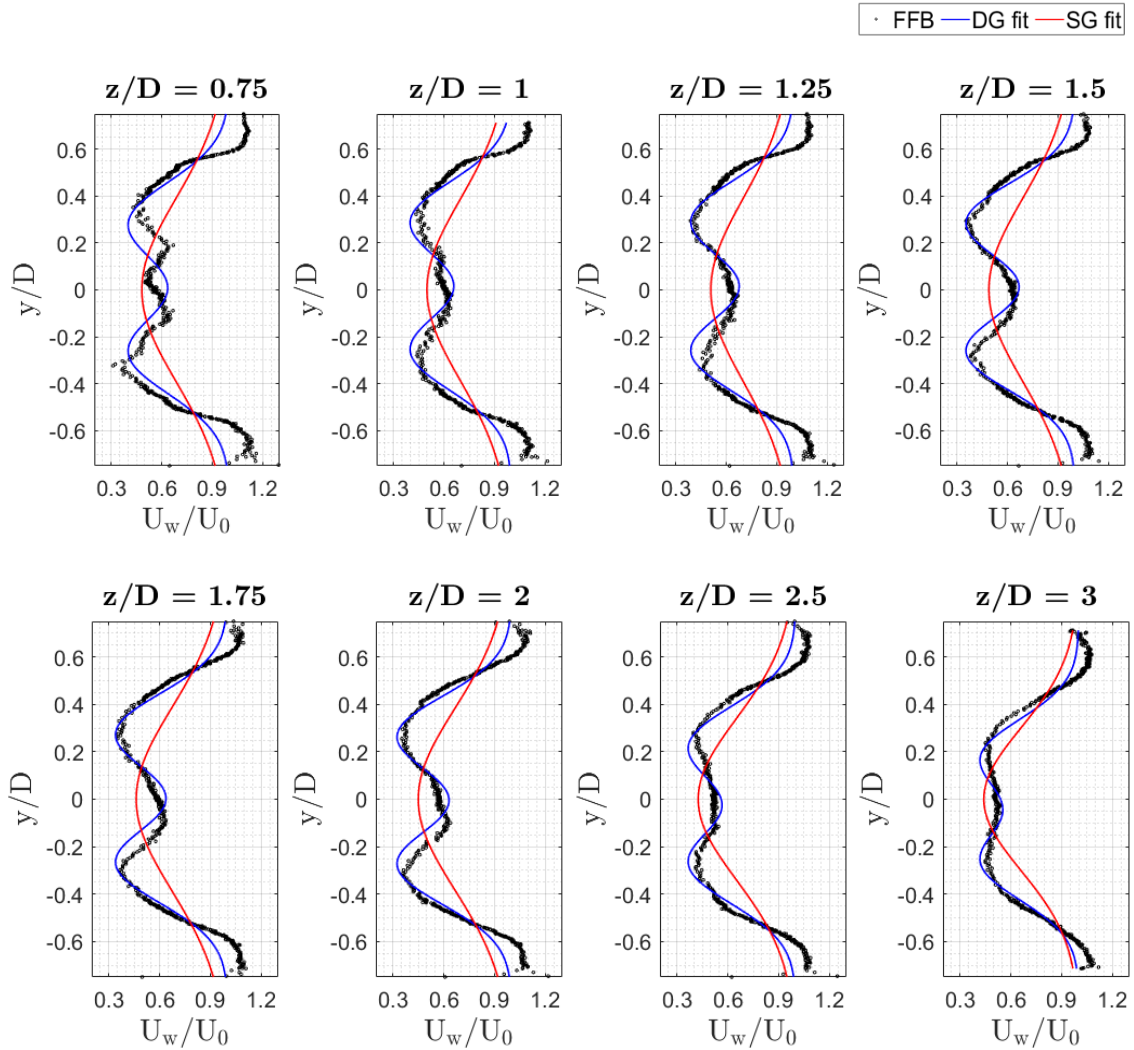


**Figure 3. 5.** Vertical profile of streamwise wake velocity at several downstream distances.

As the downstream distance increased, the significance of velocity deficit at the local minima around the blade mid-span and the centerline velocity tended to weaken, eventually forming an almost flat shape profile as in the downstream distance of  $z/D = 3$ . In the analyzed LES result, It was observed that the wake center tended to shift slightly below the centerline. If the domain were long enough, the wake distribution represented by the SG shape profile might be formed, which marked out the onset of the far-wake region.

### 3.4.4 Streamwise velocity in the lateral direction

The evolution of streamwise velocity distribution in the lateral direction is shown in Fig. 3.6. The results from the SG fit of the wake velocity in the lateral direction were also added for comparison. It can be observed that the wake shape distributions in the lateral direction also tend to form the DG shapes. Thus, the DG approach is more suitable to model the wake velocity distribution within the near-wake region than the SG-based approach.

Still the same as in the vertical direction, the wake profile resulting from the CFD dataset at  $z/D = 0.75$  shows an obtrusive velocity deficit towards the centerline. Nevertheless, the bimodal distribution still appears around the blade mid-span positions. As the downstream distance increased, the effect of hub blockage around the centerline was diminished, starting from  $z/D = 1.25$ . Therefore, the DG shape distribution was more ideally produced at the remaining evaluated distances. Interestingly, the wake center shifted to the negative side of the lateral direction from the centerline. In addition, the amplitude of the wake center velocity was reduced as the downstream distance increased.

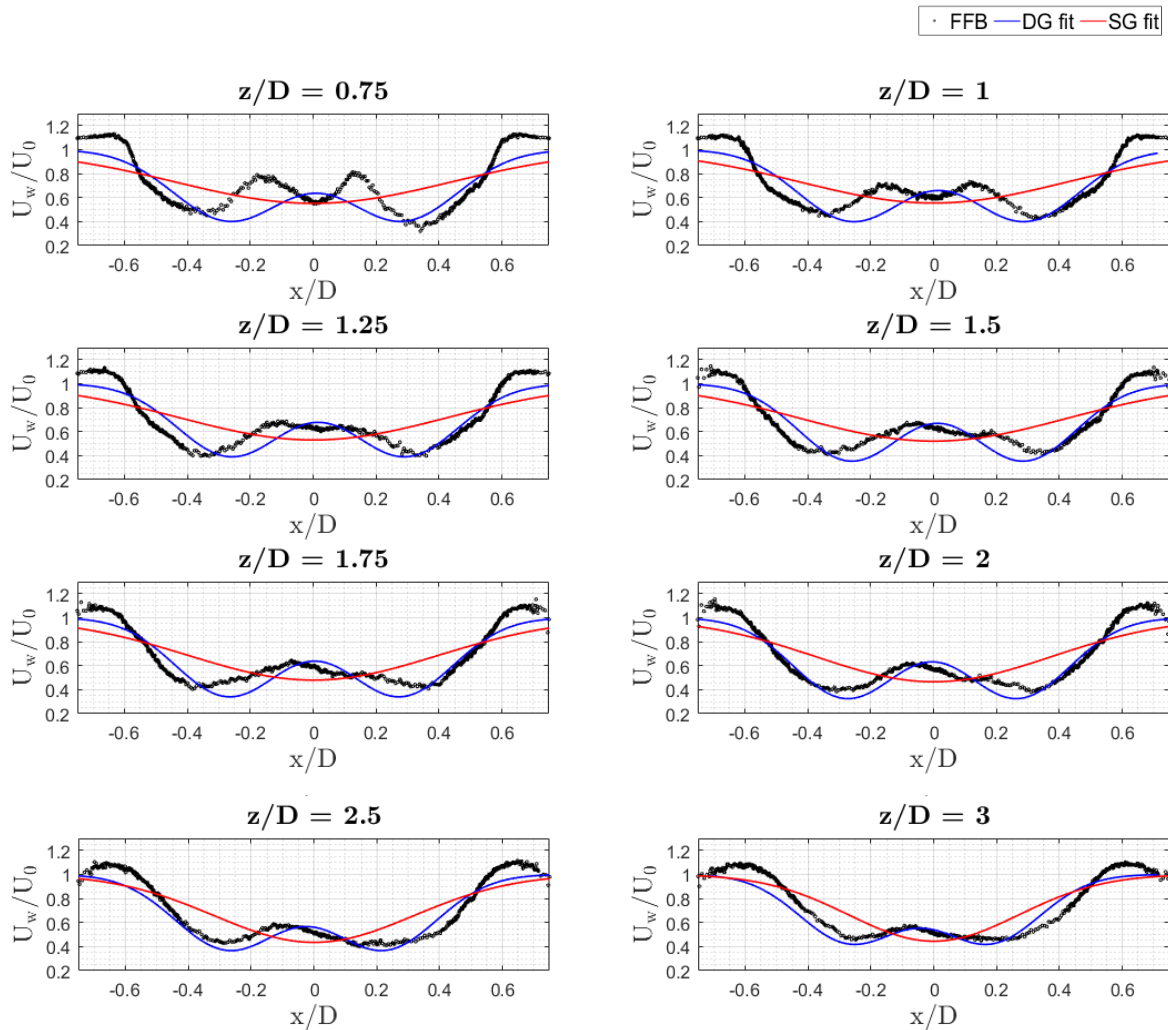


**Figure 3. 6.** Lateral profile of streamwise wake velocity at several downstream distances.

Since the conducted simulation was focused within the near-wake region, the trend of wake distribution could be well estimated using the DG function. Generally, the wake profile behind the turbine in the lateral and vertical directions has the same behavior, where the DG profile is more suitable to represent the wake distribution than the SG function due to the strong influence of the turbine's presence. However, this behavior may be valid until the transition from the near to far-wake region. Afterward, the local minima would be merged towards the wake center, and then the wake shape distribution becomes effectively single Gaussian.

### 3.4.5 The Wake Recovery

In this section, the wake recovery in both vertical and lateral directions is estimated and analyzed. The mean normalized wake velocity in the lateral direction ( $\overline{U_{w,l}}/U_0$ ) and vertical direction ( $\overline{U_{w,v}}/U_0$ ), which can be used to represent wake recovery, was estimated using the arithmetic mean. The wake data from LES result were averaged within the range of  $0.75D$  from the hub center spanned in both sides of lateral and vertical directions. Thus, a total of  $1.5D$  in length of the wake data was averaged at each evaluated downstream distance.

Based on the LES results, this length is sufficient to cover the wake expansion of the evaluated distances within the near-wake region. Finally, the comparison of the mean wake velocity in both directions is shown in Fig. 3.7(a). Meanwhile, the velocity difference between both directions at each evaluated distance is shown in Fig. 3.7(b).

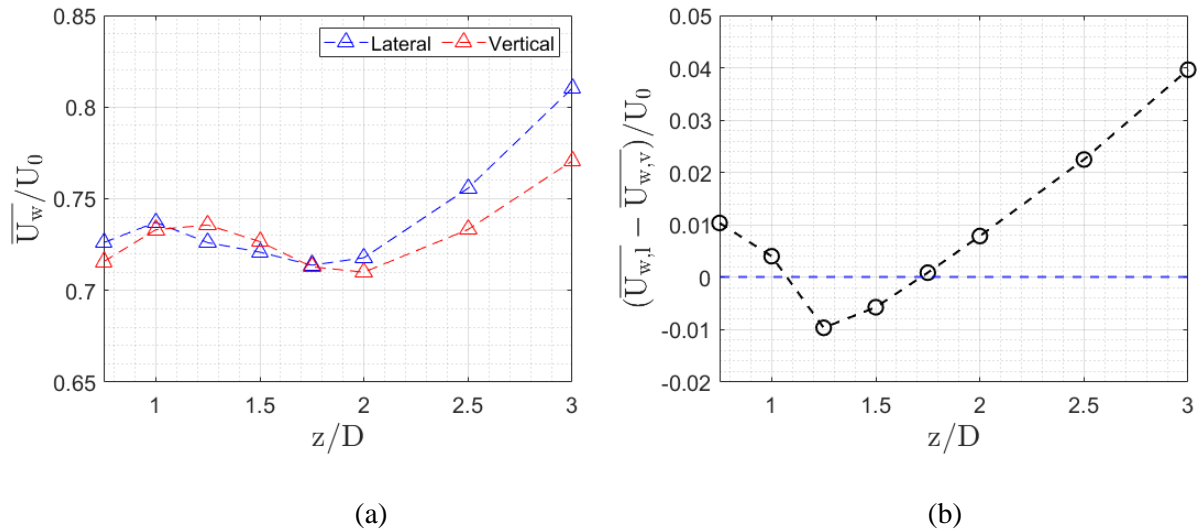


**Figure 3. 7.** The mean wake velocity in the vertical and lateral directions.

From Fig. 3.7(a), the mean wake velocity was fluctuating until  $z/D = 1.75$ . Meanwhile, both directions have almost the same rate of wake recovery, as shown in Fig. 3.7(b). Afterward, the recovery rate in the lateral direction becomes faster than in the vertical direction, observably starting from  $z/D = 2$ . The suppression of the wake recovery in the vertical direction might be due to the presence of the

ground, which may restrain the wake from expanding freely as in the lateral direction. In addition, the difference in the mean velocity between both directions was found to be more significant as the downstream distance increased. It means that the wake recovery tends to have a linear relationship with the downstream distance.

Considering the conservation of mass and momentum, the higher rate of wake recovery in the lateral direction indicated a wider wake width compared to the vertical direction. Hence, the wake expansion is effectively anisotropic. These observations are also consistent with the previous investigations regarding the wake expansion of an isolated wind turbine along the axial direction [6], [28]. Based on Fig. 3.7(b), the cross-sectional area of the wake may have an elliptical shape. The shape could become more apparent when the velocity data points spread out on a broader range, particularly within the far-wake region. The fact that the wake grows unequally in vertical and lateral directions should gain more attention among researchers to consider the anisotropic nature of the wake expansion, specifically for analytical wake modeling.

### 3.5 Conclusion

In this study, the wake velocity data from high-fidelity LES were used to investigate the near-wake behavior behind an isolated NREL 5 MW HAWT. The interaction between the uniform incoming velocity without turbulence and the rotating rotor was observed just after the domain inlet, starting from about  $z/D = 0.9$  upstream of the wind turbine. Afterward, the interaction got intense within the upstream induction zone before the rotor, where the reference incoming velocity gradually decreased due to the blockage effect from the rotating rotor. The contour of streamwise velocity from the LES result shows that the streamwise inflow velocity significantly diminished within the near-wake region downstream of the turbine. It was observed that the magnitude of the velocity deficit tended to be higher around the blade mid-span compared to its surroundings. Meanwhile, the wake recovery on the centerline profile was relatively slow. This occurrence might be due to the laminar inflow condition upstream of the turbine that slowed down the turbulence mixing from the wake boundary to the centerline, thus resulting in a slow wake recovery. As a result, a longer downstream distance would be needed for the wake centerline to regain its undisturbed condition.

Moreover, it was clarified from the LES result that the spatial distribution of the wake profile in both lateral and vertical directions within the near-wake region tends to form a DG shape. This tendency underpins the feasibility of the DG function to estimate the streamwise velocity profile distribution within the near-wake region where the effect of turbine geometry is salient. At  $z/D = 0.75$ , a significant velocity deficit towards the centerline was observed in both vertical and lateral directions, mainly due to the remaining influence of the hub blockage. As the downstream distance increased, the effect of the blockage around the centerline was diminished. Therefore, the DG shape distribution was more ideally produced at the remaining evaluated distances. As the downstream distance increased, the wake center

shifted slightly below the centerline in the vertical direction and towards the negative side from the centerline in the lateral direction. In addition, the discrepancy of wake velocity located at two local minima around the blade mid-span and the wake center became insignificant. Moreover, the two local minima shifted toward the centerline, thus the wake distribution has the potential to transform into the SG shape at further downstream distance.

In the analyzed LES result, the wake recovery rate in the lateral and vertical directions was likely to increase as the downstream distance increased. In addition, the difference in the mean velocity between both directions was found to be more significant as the downstream distance increased. This means that the wake recovery tends to have a linear relationship with the downstream distance. Moreover, it was observed that the wake tends to recover in an anisotropic way in which the wake recovery rate in the vertical direction is less than in the lateral direction. The suppression of this wake recovery in the vertical direction might be due to the presence of the ground, which may restrain the wake from expanding freely as in the lateral direction. Hence, for analytical wake modeling, it is recommended to consider the DG shape function with anisotropic expansion for better accuracy of streamwise velocity prediction within the near-wake region.

## Chapter 4

# Anisotropic DG analytical wake model for an isolated HAWT

### *Attribution*

*Q. M. B. Soesanto, T. Yoshinaga, and A. Iida, "Anisotropic double-Gaussian analytical wake model for an isolated horizontal-axis wind turbine," Energy Sci. Eng., vol. 10, no. 7, pp. 2123–2145, 2022, doi: <https://doi.org/10.1002/ese3.1120> is made available under the terms of the Creative Commons Attribution License (CC BY 4.0), with minor modification.*

### 4.1 Overview

An anisotropic DG wake model for analytical wake modeling to predict the streamwise wake velocity behind an isolated non-yawed HAWT is proposed. The proposed model is based upon the conservation of mass and momentum inside Streamtube control volume. The wake growth rate parameters to distinguish the wake expansion rate between lateral and vertical directions were tuned based on numerical and measurement data of utility-scale turbines. It was found that the proposed model can give feasible predictions within a full-wake region under different inflow conditions. In addition, the other analytical models based on the top-hat shape and single Gaussian approaches were evaluated for comparison. The root-mean-square error (RMSE) statistical analysis was used to evaluate the performance of each examined model under different flow conditions. In general, the proposed model outperformed the other examined models in all wake region categories, particularly within the near-wake and the onset of the far-wake region which is beyond the scope of the conventional approach for analytical wake modeling. This advantage gives the potential for the proposed model to provide a better prediction for the wake flow estimation within tightly packed wind farms.

### 4.2 Introduction

By considering the sustainable development scenario, wind energy becomes the main player for renewable resources projected to provide 21% of electricity supply worldwide by 2040 [35]. One of the challenging topics in wind energy research is to fully understand the aerodynamics of wind turbine wake since any turbine placed inside this wake region will undergo power losses and structural failures [12]. The wake itself is roughly identified as a plume-like region that evolves downstream the turbine where the wind velocity diminished and turbulence intensity escalated [36]. It is prevalent to characterize the wake flow behavior by predicting its velocity field. Since the available wind energy which can be extracted to generate electricity is proportional to the cube of the wind velocity, thus incorrect estimation of wake velocity of the upstream turbines can lead to inaccurate prediction of power generation by the downstream turbines.

Given the paramount of this wake velocity prediction, many investigations have been conducted to model the detailed velocity field within the wake region. Generally, the wake velocity field can be

modeled with simple analytical models [5], [6], [22], [26], [43] or more sophisticated numerical approaches based on computational fluid dynamics (CFD) [44]. Despite being less accurate than CFD-based approaches, the simplicity of analytical models and its low computational cost makes the analytical approach the preferred choice for optimizing the wind farm layout [4], [36]. Knowing that this analytical-based approach is feasible to give a practical solution in a wind industry sector, the presented study focuses on the analytical wake model development.

Analytical wake model provides fundamental insight into the physics where their formulations rely on the derivation of fluid flow conservation equations. The flow physics inside the wind turbine wake itself can be roughly divided into two main regions: (i) near-wake region, which is roughly taken as the area just behind the rotor, and (ii) far-wake region, which is the region beyond the near wake [1]. Inside the near-wake region, the flow field characteristics are strongly influenced by the turbine geometry. Meanwhile, the flow characteristics of the far wake become more dependent on atmospheric and topographic conditions [45]. Since the wake is fully developed in this far-wake region and, in the hypothetical absence of ambient shear flow, the perturbation profiles of velocity deficit and turbulence intensity are assumed to be axisymmetric and have self-similar distributions in the wake cross-sections. These self-similar and axisymmetric properties then become the basis of analytical models to predict the wake velocity profiles either by using top-hat shape [20], [21] or Gaussian shape distribution [5], [6].

One of the pioneering works in analytical wake modelling is the top-hat shape wake model proposed by Jensen in his technical report [20] and polished by Katic et al [21]. This model was derived by only considering the mass conservation equation. The wake velocity was described in a much-idealized way. The velocity inside the wake region was considered constant. Later work by Frandsen et al [22] used the same top-hat shape assumption for the rectangular distribution of the wake velocity profiles. Their work also considered the momentum conservation and the mass equation and was formulated to encompass velocity deficit for both small and large regular wind farms with rectangular shapes. Although those top-hat models were derived without violating the general principles of conservation equations, in fact, the actual wake shape distribution tends to follow a Gaussian shape function [1], [37], [38]. By considering this reality, some recently developed analytical models were based on this Gaussian function to estimate the streamwise flow field within the wake region [5], [46].

Moreover, another Gaussian model considered the non-axisymmetric shape of the wake area because the wake expands in an anisotropic manner under different atmospheric conditions [6]. However, those mentioned Gaussian wake models were based on a single Gaussian (SG) approach, which may be valid only for velocity deficit estimation within the far-wake region. While in the near-wake region, it was clarified both numerically and experimentally that the wake profiles resemble the DG distribution, which contains two local minima corresponding to maximum lift points along the blades [2]. Hence, it is worth considering the DG shape function to better approximate velocity distribution inside the near-wake region.

To date, the analytical investigations that focused on the wake development within the near wake region are few. Therefore, further investigations will be needed to elucidate accurately the aerodynamic behavior of tightly spaced wind farms, which might be out of the prediction capability from the standard wake models. Related to the near-wake study, Aitken et al [47] developed a set of statistical models for the characterization of wind turbine wakes, including an analytical wake model for the near-wake region using the DG approach. However, the parameter for velocity deficit amplitude was not derived directly but was estimated using data fitting from the Doppler Lidar measurement instead. More recently, Keane et al [48] proposed an analytical wake model based on the DG approach to predict the wake velocity for all downstream distances by applying conservation of mass and momentum. However, Schreiber et al [26] found some issues in the original Keane model, which primarily related to its inconsistency to satisfy the conservation of mass and momentum. Hence, some previously derived expressions were reformulated. In addition, a new wake expansion function was defined using Streamtube control volume, which is a simplified approach to analyze complex airflow through a horizontal-axis wind turbine. Although recent work by Keane [48] improved his previously published DG-based wake model, however, none of those mentioned DG models explicitly consider the anisotropic behavior of wake expansion which is inevitable, particularly under different types of atmospheric stability [28]. Furthermore, the radial position of local minima of the DG wake profile needed to be tuned case by case, thus limiting its generality.

This study complements the previous study regarding analytical wake modeling using the DG function [26] to model the streamwise wake velocity behind isolated non-yawed HAWTs. The anisotropic nature of the wake growth rate downstream of the wind turbine is considered, thus facilitating its usability under different atmospheric stabilities. Moreover, the additional empirical coefficient for utility-scale turbines is added to the original formula of far-wake onset [29] to calculate the stream tube outlet position instead of tuning. Meanwhile, the constant value of Gaussian minima  $r_0$  for utility-scale turbines is suggested based on the root-mean-square error (RMSE) evaluation. Finally, the effectiveness of the proposed DG model within a full-wake region was validated against the CFD dataset and lidar measurements of utility-scale turbines. In addition, the prediction results from the top-hat shape and anisotropic SG analytical wake models were also included for comparison.

## 4.3 Methodology

### 4.3.1 Anisotropic DG wake model

A simple approach is needed to consider the energy extraction process of the turbine, one of which is by employing the actuator disc theory. In this approach, the rotor is replaced by a circular disc where the airstream flows inside the Streamtube control volume. Fig. 4.1 illustrates this control volume scheme where the airflow in a streamwise direction comes from the inlet section  $A_0$  with the undisturbed velocity at  $U_0$  and exits from the outlet section  $A_w$  with the wake velocity  $U_w$  where the air pressure has

regained its undisturbed condition,  $p_w = p_0$ . The actuator disc with its permeable surface partially blocks the incoming flow for extracting the wind energy and causes the pressure drop  $\Delta p$  over the disc area, which is proportional to axial thrust force  $T$ . The incoming velocity that decreases at the disc due to the thrust force  $T$  would be even smaller in the wake section  $A_w$ . Since the mass flow rate  $\dot{m}$  is conserved throughout the flow, the cross-sectional area increases at the disc and continues to expand at the wake area  $A_w$ .

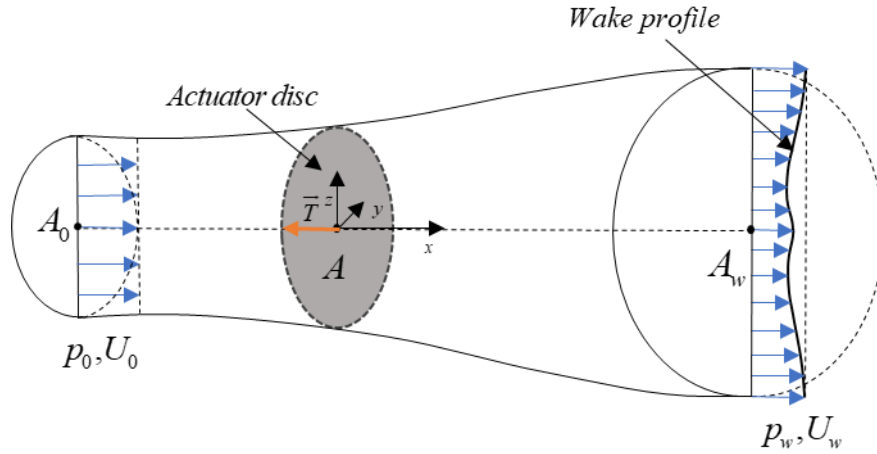


**Figure 4. 1.** Streamtube control volume of horizontal-axis wind turbine rotor modelled by an actuator disc.

By using the same approach by Frandsen et al [22] where shear forces on the control volume and the acceleration, pressure, and gravity terms are neglected, in addition, if the pressure at the inlet and outlet of the Streamtube is equal, the axial momentum equation on the control volume that assuring the conservation of mass and momentum can be formulated as follows:

$$\rho \int_{A_w} U_w (U_0 - U_w) dA_w = T, \quad (4. 1)$$

where  $\rho$  denotes the air density. The axial thrust force can also be expressed as the function dimensionless parameter for the rotor performance, thrust coefficient  $C_T$ , using the following correlation:

$$T = \frac{1}{2} \rho C_T A U_0^2, \quad (4. 2)$$

where  $A = \frac{\pi D^2}{4}$  is rotor cross-sectional area and  $D$  is the rotor diameter. The velocity difference between  $U_0 - U_w$  is the velocity deficit downstream of the turbine  $\Delta U$ . Suppose the deficit is normalized against the undisturbed flow velocity and the anisotropic wake expansion of the wake profile in Gaussian shape is considered, an expression for normalized velocity deficit can be written as follows:

$$\frac{\Delta U}{U_0} = C(\sigma(x))f(r(y, z), \sigma(x)), \quad (4.3)$$

where  $C(\sigma(x))$  is amplitude function which defines the normalized maximum velocity deficit,  $\sigma(x) = \sqrt{\sigma_y(x)\sigma_z(x)}$  is the standard deviation of the velocity deficit which represents the wake expansion function, and  $f(r(y, z), \sigma(x))$  is the Gaussian shape function which represents the wake profile distribution. In this study, the proposed analytical model for estimating wake development is intended to cover the wake prediction within the near-wake region, therefore a DG-based approach for the wake distribution is used. The DG shape function for anisotropic wake expansion is formulated as follows:

$$f(r(y, z), \sigma(x)) = \frac{1}{2} \left( e^{DG^+} + e^{DG^-} \right), \quad DG^\pm = -\frac{1}{2} \left( \sqrt{\frac{y^2}{\sigma_y^2} + \frac{(z - z_h)^2}{\sigma_z^2}} \pm \frac{r_0}{\sigma} \right)^2, \quad (4.4)$$

where  $r_0$  denotes the radial position of Gaussian minima, which is assumed to be equal for both sides from the wake center at each lateral ( $y$ ) and vertical ( $z$ ) direction. In this study, its value was derived empirically from the CFD data and lidar measurements. Meanwhile,  $\sigma_y$  and  $\sigma_z$  are wake expansion function at lateral and vertical directions, respectively. By referring to Schreiber et al [26] for deriving isotropic DG wake model from momentum and mass conservation equations, the following equation for anisotropic DG wake model is obtained using the substitutions of Eqs. (4.3) and (4.4) into Eq. 4.1):

$$T = \frac{1}{2} \rho U_0^2 C(\sigma(x)) \int_{A_w} \left( e^{DG^+} + e^{DG^-} - \frac{C(\sigma(x))}{2} (e^{2DG^+} + e^{2DG^-} + 2e^{DG^+ + DG^-}) \right) dA_w. \quad (4.5)$$

In this study, the DG function is integrated over the wake cross-sectional area  $A_w$ , expanding to infinity on the entire two-dimensional rotor plane (Y-Z plane). Since the integration was performed over all real numbers, thus the integral limits can be set as twofold of integral from zero to infinity. The integral forms of anisotropic two-dimensional DG function can be encapsulated using the following forms:

$$T_A = 4 \times \left( \underbrace{\int_0^\infty \int_0^\infty e^{DG_+} dydz}_{T_1} + \underbrace{\int_0^\infty \int_0^\infty e^{DG_-} dydz}_{T_2} \right), \quad (4.6)$$

and

$$T_B = 2 \times \left( \underbrace{\int_0^\infty \int_0^\infty e^{2DG_+} dydz}_{T_3} + \underbrace{\int_0^\infty \int_0^\infty e^{2DG_-} dydz}_{T_4} + 2 \underbrace{\int_0^\infty \int_0^\infty e^{DG_+ + DG_-} dydz}_{T_5} \right). \quad (4.7)$$

To ease the integration, the parameters of  $T_A$  and  $T_B$  are decomposed into two terms ( $T_1$  and  $T_2$ ) and three terms ( $T_3$ ,  $T_4$ , and  $T_5$ ), respectively. Integrating the first term of  $T_A$  yields

$$T_1 = \frac{\pi}{4} \left( 2\sigma_y \sigma_z e^{-\frac{r_0^2}{2\sigma_y \sigma_z}} + \sqrt{2\pi} r_0 \sqrt{\sigma_y \sigma_z} + \sqrt{2\pi} r_0 \sqrt{\sigma_y \sigma_z} \operatorname{erf} \left( \frac{r_0}{\sqrt{2} \sqrt{\sigma_y \sigma_z}} \right) \right), \quad (4.8)$$

where  $\operatorname{erf}$  is Gauss error function defined as:

$$\operatorname{erf}(x) = \frac{2}{\sqrt{\pi}} \int_0^x e^{-t^2} dt.$$

Implementing the complementary error function  $\operatorname{erfc}(x) = 1 - \operatorname{erf}(x)$  and taking account of the identity  $\operatorname{erf}(-x) = -\operatorname{erf}(x)$ , the expression for  $T_1$  can be defined in more simple expression as follows:

$$T_1 = \frac{\pi}{4} \left[ 2\sigma_y \sigma_z e^{-\frac{r_0^2}{2\sigma_y \sigma_z}} - \sqrt{2\pi} r_0 \sqrt{\sigma_y \sigma_z} \operatorname{erfc} \left( \frac{r_0}{\sqrt{2} \sqrt{\sigma_y \sigma_z}} \right) \right]. \quad (4.9)$$

Similarly, the second term of  $T_A$  can be integrated and yields

$$T_2 = \frac{\pi}{4} \left( 2\sigma_y \sigma_z e^{-\frac{r_0^2}{2\sigma_y \sigma_z}} + \sqrt{2\pi} r_0 \sqrt{\sigma_y \sigma_z} \operatorname{erfc} \left( \frac{-r_0}{\sqrt{2} \sqrt{\sigma_y \sigma_z}} \right) \right). \quad (4.10)$$

Finally, the parameter  $T_A$  can be obtained by performing summation from integral solutions of  $T_1$  and  $T_2$ . Employing the Gauss error function via  $\operatorname{erf}(x) = 1 - \operatorname{erfc}(x)$  and its identity property, the final expression of  $T_A$  can be formulated to a more compact form as follows:

$$T_A = 2\pi \underbrace{\left( 2\sigma_y \sigma_z e^{-\frac{r_0^2}{2\sigma_y \sigma_z}} + \sqrt{2\pi} r_0 \sqrt{\sigma_y \sigma_z} \operatorname{erf} \left( \frac{r_0}{\sqrt{2} \sqrt{\sigma_y \sigma_z}} \right) \right)}_M. \quad (4.11)$$

Analogous to the integration procedures explained above, the integral terms of  $T_3$ ,  $T_4$ , and  $T_5$  can be solved and compactly written as follows:

$$T_3 = \frac{\pi \sigma_y \sigma_z}{4} \left( e^{\frac{-r_0}{\sigma_y \sigma_z}} + \frac{\sqrt{\pi} r_0 \operatorname{erf} \left( \frac{r_0}{\sqrt{\sigma_y \sigma_z}} \right)}{\sqrt{\sigma_y \sigma_z}} - \frac{\sqrt{\pi} r_0}{\sqrt{\sigma_y \sigma_z}} \right), \quad (4.12)$$

$$T_4 = \frac{\pi \sigma_y \sigma_z}{4} \left( e^{\frac{-r_0}{\sigma_y \sigma_z}} + \frac{\sqrt{\pi} r_0 \operatorname{erf} \left( \frac{r_0}{\sqrt{\sigma_y \sigma_z}} \right)}{\sqrt{\sigma_y \sigma_z}} + \frac{\sqrt{\pi} r_0}{\sqrt{\sigma_y \sigma_z}} \right). \quad (4.13)$$

Afterwards, combining terms  $T_3$  and  $T_4$  gives:

$$T_3 + T_4 = \frac{2\pi\sigma_y\sigma_z}{4} \left( e^{\frac{-r_0}{\sigma_y\sigma_z}} + \frac{\sqrt{\pi}r_0 \operatorname{erf}\left(\frac{r_0}{\sqrt{\sigma_y\sigma_z}}\right)}{\sqrt{\sigma_y\sigma_z}} \right). \quad (4.14)$$

Next, the solution for the last term  $T_5$  after integration can be expressed as follows:

$$T_5 = \frac{2\pi\sigma_y\sigma_z}{4} e^{\frac{-r_0^2}{\sigma_y\sigma_z}}. \quad (4.15)$$

Combining all integrated forms of  $T_3$ ,  $T_4$ , and  $T_5$  resulting in the following formula of  $T_B$

$$T_B = 2\pi \underbrace{\left( \sigma_y\sigma_z e^{\frac{-r_0^2}{\sigma_y\sigma_z}} + \frac{\sqrt{\pi}}{2} r_0 \sqrt{\sigma_y\sigma_z} \operatorname{erf}\left(\frac{r_0}{\sigma_y\sigma_z}\right) \right)}_N. \quad (4.16)$$

Finally, the following expression can be obtained:

$$T = \pi\rho U_0^2 C(\sigma(x)) (M - C(\sigma(x))N), \quad (4.17)$$

where

$$M = 2\sigma_y\sigma_z e^{\frac{-r_0^2}{\sigma_y\sigma_z}} + \sqrt{2\pi}r_0\sqrt{\sigma_y\sigma_z} \operatorname{erf}\left(\frac{r_0}{\sqrt{2}\sqrt{\sigma_y\sigma_z}}\right), \quad (4.18)$$

and

$$N = \sigma_y\sigma_z e^{\frac{-r_0^2}{\sigma_y\sigma_z}} + \frac{\sqrt{\pi}}{2} r_0 \sqrt{\sigma_y\sigma_z} \operatorname{erf}\left(\frac{r_0}{\sqrt{\sigma_y\sigma_z}}\right). \quad (4.19)$$

Next, the amplitude function  $C(\sigma(x))$  for the DG distribution, which maintains the momentum conservation can be defined by substituting Eq. 4.2 into Eq. 4.17. By employing the quadratic formula, the realistic solution for the amplitude function is as follows:

$$C(\sigma(x)) = \frac{M - \sqrt{M^2 - 1/2NC_T D^2}}{2N}. \quad (4.20)$$

If  $\sqrt{M^2 - 1/2NC_T D^2} < 0$ , then the solution is approximated using absolute value or modulus of a complex number as proposed by Keane [27]:

$$C_c(\sigma(x)) = \frac{\left(M^2 + \left|M^2 - 1/2NC_T D^2\right|\right)^{\frac{1}{2}}}{2N}. \quad (4.21)$$

Thus, for  $\sqrt{M^2 - 1/2NC_T D^2} < 0$ , the expression for normalized velocity deficit as formulated in Eq. (4.3) becomes:

$$\frac{\Delta U}{U_0} = C_c(\sigma(x))f(r(y, z), \sigma(x)). \quad (4.22)$$

In this study, the wake expansion function in the lateral direction  $\sigma_y$  and vertical direction  $\sigma_z$  are defined explicitly instead of using the same expansion function  $\sigma$  for all directions. Thus, the wake expansion functions from the isotropic DG wake model [26] are reformulated as follows:

$$\frac{\sigma_y(x, y)}{D} = k_y \frac{(x - x_0)}{D} + \varepsilon, \quad (4.23)$$

$$\frac{\sigma_z(x, z)}{D} = k_z \frac{(x - x_0)}{D} + \varepsilon. \quad (4.24)$$

Since the rate of wake expansion is considered anisotropic, thus the lateral growth rate of the wake in the lateral direction  $k_y$  and vertical direction  $k_z$  are set differently. Meanwhile,  $x_0$  denotes the downstream position of the Streamtube outlet where the pressure has regained its undisturbed flow ( $p_w = p_0$ ). This position represents the onset of the far-wake region which can be calculated based on the formula proposed by Bastankhah and Porté-Agel [29]. However, the parameter in this formula was derived empirically based on wind tunnel measurements, therefore its compatibility for the actual utility-scale turbine needs to be re-evaluated. This is mainly because the Reynolds numbers  $R_e$  in wind tunnel measurements is significantly lower than those of actual turbines. Hence, a coefficient  $c$  is added to the original formula as a scale factor to fit with the utility-scale turbines. Hence, in this study, the far-wake onset formula for an isolated non-yawed utility-scale HAWT is formulated as follows:

$$\frac{x_0}{D} = \frac{1 + \sqrt{1 - C_T}}{\sqrt{2c} \left( 4\alpha TI_u + 2\beta \left( 1 - \sqrt{1 - C_T} \right) \right)}, \quad (4.25)$$

where  $\alpha=0.58$ ,  $\beta=0.077$ .

In this study, several cases from LES simulations and lidar measurements for the wake flow behind utility-scale turbines (some information can be found in Table 1) were used to find the best fit values of the parameter  $r_0$  and coefficient  $c$  using RMSE analysis. The result is shown in Fig. 4.2.

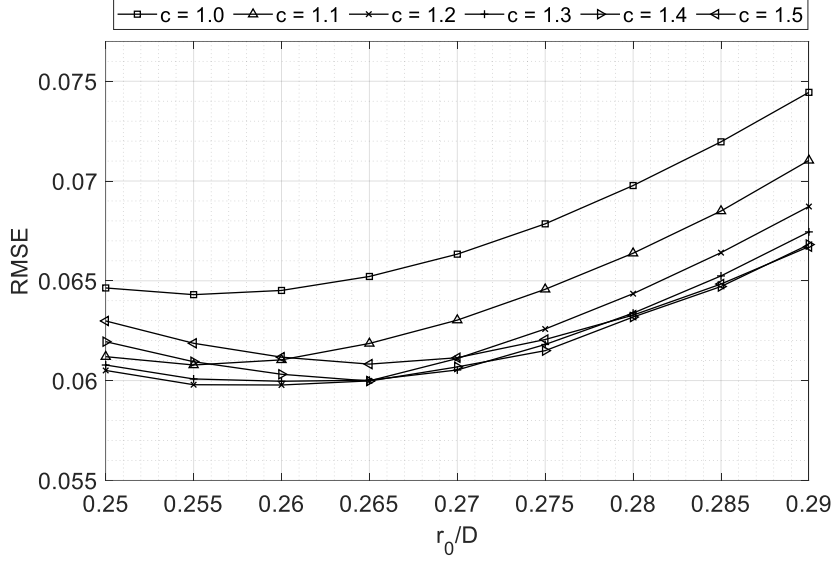


**Figure 4. 2.** Case-averaged total RMSE against LES simulations and lidar measurements for pairs of parameters  $r_0$  and coefficient  $c$  (Eq. 4.25).

Fig. 4.2 shows that  $r_0 = 0.26$  and  $c = 1.2$  have the best fit against the analyzed LES simulations and lidar measurements for wake flow behind isolated utility-scale wind turbines. Hence, these values are used in the present study for all evaluated cases and is also suggested for utility-scale wind turbines.

Considering the mass conservation inside the Streamtube control volume, the wake expansion at the outlet  $\mathcal{E}$  as derived in [26] is used. If we assume that there is no incoming flow into the control volume through its surface, the wake expansion at the outlet may be obtained according to the mass conservation equation within the wake region. Thus, by equating the total mass flow deficit at the position just behind the turbine  $\dot{m}_1(x = 0)$  [22] and at the Streamtube outlet  $\dot{m}_2(x = s_{out})$  where the anisotropic expansion is considered, the wake expansion at the outlet can be approximated using the following expression:

$$\frac{D^2\beta}{8} \left( 1 - \sqrt{1 - \frac{2}{\beta} C_T} \right) = M(\varepsilon) \frac{M(\varepsilon) - \sqrt{M(\varepsilon)^2 - \frac{1}{2} N(\varepsilon) C_T D^2}}{2N(\varepsilon)}, \quad (4. 26)$$

where  $\beta$ , which is the ratio between the initial wake area immediately after the wake expansion  $A_1(x = 0)$  and the rotor area  $A$ , is expressed as the function of thrust coefficient  $C_T$  by:

$$\beta = \frac{1}{2} \frac{1 + \sqrt{1 - C_T}}{\sqrt{1 - C_T}}. \quad (4. 27)$$

The left side in Eq. 4.26 is the mass flow deficit rate at downstream distance  $x = 0$  obtained using the Frandsen model [22]. Meanwhile, the right-hand side is derived from the mass flow deficit rate at the Streamtube outlet from the DG model. Based on Eq. 4.26, the quantity of  $\varepsilon$  would be complicated to be defined explicitly, thus the solution is obtained numerically.

After the parameters of amplitude and Gaussian functions are obtained using the previously described formulas, the wake velocity behind an isolated wind turbine can be estimated. Another essential factor that needs to be included in calculating wake velocity is the incoming flow condition. It should be noted that the conservation equation which underlies the proposed formulas is assumed to have uniform inflow distribution. Therefore, the wind shear function cannot be integrated directly into the formula. To overcome this limitation, a simple approach is employed to consider the non-uniformity of the incoming flow using superposition of incoming streamwise velocity and the predicted velocity deficit. By using this assumption, the normalized wake velocity  $\frac{U_w(x,y,z)}{U_0}$  is predicted as follows:

$$\frac{U_w(x, y, z)}{U_0} = \frac{U_{in}}{U_0} - \frac{\Delta U}{U_0}, \quad (4.28)$$

where  $U_{hub}$  is the incoming velocity at the hub height and  $U_{in}$  denotes the incoming velocity at the relative height from the ground either in uniform, power-law, or logarithmic profile distribution.

The proposed anisotropic DG model was first tested to predict the wake velocity behind a HAWT with a rotor diameter  $D$  of 178.3 m and a hub height of 119 m, INNWIND 10 MW [49]. The wake prediction was validated against the SOWFA simulation results conducted under CL-Windcon project [50]. The turbine thrust coefficient  $C_t$  is 0.75, was resulted under ABL inlet with moderate incoming turbulence of 8.5%. A total of 121 points at the hub height in the lateral direction ( $-1.5D:0.025D:1.5D$ ) and 88 points in the vertical direction ( $-\text{hubheight}:0.25:1.5D$ ) centered at the rotor, were used to measure the wake velocity. The residuals between the simulation and analytical results were measured using the root-mean-square error (RMSE). Pair of RMSEs from both lateral and vertical directions at each evaluated downstream distance were averaged ( $\overline{RMSE_{lat,ver}}$ ) to quantify the mean error of analytical prediction. There are 11 downstream distances in total for the evaluation. The residual measurement result is shown in Fig. 4.3.

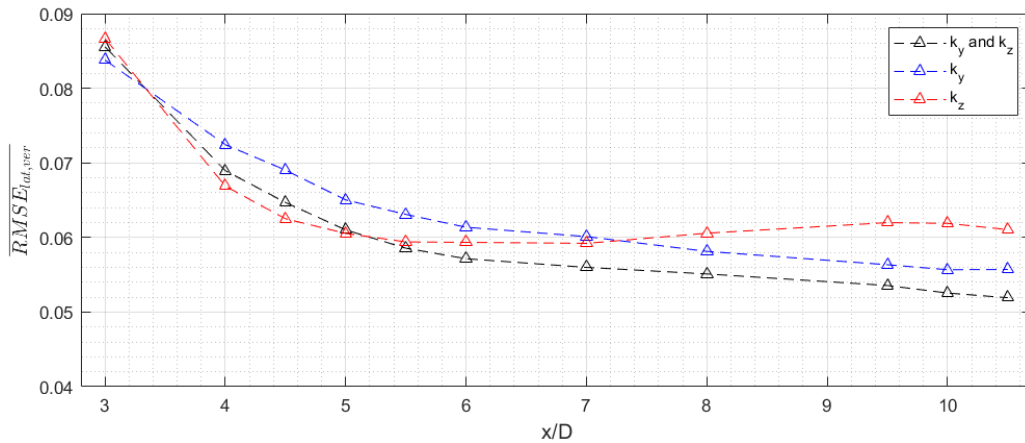


**Figure 4. 3.** RMSEs averaged from both lateral and vertical directions at each evaluated downstream distance ( $\overline{RMSE_{lat,ver}}$ ).

The wake expansions in both directions were fitted to the SOWFA data, where the wake velocity in the lateral direction expanded faster ( $k_y=0.037$ ) than in the vertical direction ( $k_z=0.02$ ). As shown in Figure 4.x, the proposed anisotropic DG model can give a better prediction from the resulting  $RMSE_{lat,ver}$ , particularly at the further downstream distance, compared to the isotropic model, in which either lateral ( $k_y$ ) or vertical expansion ( $k_z$ ) was used in both directions. This noticeable anisotropy wake expansion at a further downstream distance is reasonable since the wakes were observed to expand linearly with the downstream distance [28]. The proposed anisotropic DG model will be evaluated further in the following chapter using several cases of the wake expansion behind utility-scale turbines.

### 4.3.2 Model validation

The effectiveness of the proposed model for the prediction of wake velocity profiles for both lateral and vertical directions was validated against CFD simulation and experimental measurement of utility-scale turbines. Table 1 shows the relevant cases used in this study to validate the proposed DG model.

**Table 4. 1.** Relevant cases from CFD simulation and LiDAR measurements to validate the proposed DG model.

Cases	Turbines	$D$ (m)	$Z_h$ (m)	$U_0$ ( $\text{ms}^{-1}$ )	$TI_u$	$C_T$
1	NREL 5 MW	126	95	11.4	-	0.645
2	INNWind 10 MW	178.3	119	7.87	0.051	0.767
3				7	0.082	0.82
4	AREVA M5000	116	90	9	0.073	0.81
5				11	0.068	0.79

Several relevant cases for wake flow measurements behind HAWTs, as tabulated in Table 1, were used in this study for validation purposes. In this study, the utility-scale wind turbines in the typical MW-class turbine sizes range were chosen to represent the actual large turbines.

In Table 4.1, case 1 corresponds to high-fidelity large eddy simulation (LES) of a utility-scale reference wind turbine from National Renewable Energy Laboratory (NREL), NREL 5MW reference HAWT. Further details regarding the turbine can be found in Jonkman et al [41]. The LES simulation of full-scale analysis of the turbine was conducted using a non-commercial CFD solver FrontFlow/blue (FFB) [51], and was performed on Japan's Supercomputer Fugaku. The FFB solver uses the finite-element method (FEM) to solve the unsteady incompressible Navier-Stokes (NS) equations numerically under cartesian coordinates. A structured hexahedral mesh was used in the entire computational domain with a total number of 375960278 elements. Meanwhile, the blade geometry was directly modeled, thus the detailed vortical structures around the rotating blades were expected to be reasonably produced. By concentrating only on the details of the natural development of the wake flow field induced by the turbine, uniform inlet condition  $U_0$  of 11.4 m/s without turbulence was set at the domain inlet. The mean of fully developed wake flow field data from the last six revolutions was used to validate the

effectiveness of the proposed DG model, particularly within the near wake region where the influence of turbine presence is dominant.

The second case in Table 1 was simulated using SOWFA (Simulator fOr Wind Farm Applications), an LES solver developed by NREL for wind farm simulations [52]. The indirect approach for blade modeling was used by employing the actuator line model (ALM). Since the ALM uses the aerodynamic information of each blade element, thus an accurate representation of the blade aerodynamics can be obtained. An isolated non-yawed utility-scale reference wind turbine INNWIND 10 MW [49] was used in the SOWFA simulation. The computations were carried out under CL-Windcon project, and the LES data are opened publicly as a public database upon request [50]. The averaged data of fully-developed wake flow from the last 600 seconds of the simulation time were processed as a numerical benchmark. In the simulation, the turbine was operated under the ABL with the reference velocity at the hub height  $U_0=7.87$  m/s with the incoming streamwise turbulence intensity  $TI_u$  of 5.1%. Pairs of streamwise wake velocity profiles in lateral and vertical directions were sampled at several downstream distances (up to  $22D$ ) behind the turbine for validation purposes.

The cases 3-5 in Table 4.1 correspond to lidar measurements of streamwise velocity along the wake centerline at hub height behind the actual offshore wind turbine AREVA M5000 [53]. The turbine is located within Alpha Ventus Offshore wind farm located in the North Sea 45 kilometers north of the island of Borkum, Germany. Based on long-term measurement (2011 to 2018) from the meteorological mast FINO 1, which is located upstream of the AREVA turbine, the average incoming wind speed at the hub height of 90 m towards the turbine was about 9 m/s [54]. Thus, the lidar measurement (ten-minute averaging period) from that mean incoming velocity of 9 m/s was chosen. In addition, two resulting wake centerline profiles filtered from lidar data originating from the reference velocity of 7 and 11 m/s were also analyzed. In cases 3-5, the extracted data of streamwise turbulence intensity from FINO1 followed the definition from IEC 61400-3 standard for offshore turbulence intensity, which is based on an approximation of the 90<sup>th</sup> percentile of the standard deviation of streamwise wind velocity at hub height [55]. An open-source semi-automated tool WebPlotDigitizer [56] was used to approximate the cited data sets initially published in the image format, resulting in the 90<sup>th</sup> percentile of streamwise turbulence intensity  $TI_{u,90} \approx 8.2, 7.3, 6.8\%$  [55] and the turbine's  $C_t \approx 0.82, 0.81, \text{ and } 0.79$  [57] at the mean incoming velocities of 7, 9, and 11 m/s, respectively.

### 4.3.3 Model calibration

In this study, the parameters of wake growth rate in both lateral and vertical directions ( $k_y$  and  $k_z$ ) in the proposed-DG model were calibrated against the benchmark data sets. The calibration minimized the residuals between the measured and the predicted values by optimizing the adjusted parameters using the MATLAB function *fminsearchcon* [42]. In addition, the Jensen model [20], which is popular as an industry-standard wake model, was also evaluated for comparison. Meanwhile, the anisotropic SG model, which considers the anisotropic wake expansion as proposed by Xie *et al.* (XA-SG) [6], was also

examined for the same purpose. Here, the formula of initial wake expansion  $\varepsilon=0.2\sqrt{\beta}$  in the original anisotropic SG model led to complex solutions of wake velocity within the near-wake region. Therefore, the initial wake expansion formula was redefined to  $\varepsilon=0.25\sqrt{\beta}$ , which is resulted from analytical derivation [5], thus resulting in real solutions as expected. The wake expansion parameters of those analytical models were also calibrated to get their optimal performances for the given cases. The tuning results are shown in Table 4.2, and the details of flow condition and turbine characteristics of each case are informed in Table 4.1.

**Table 4. 2.** Tuned wake expansion parameters of the respective wake models for different case studies.

Cases	Turbines	Proposed DG		Anisotropic SG		Jensen model
		$k_y$	$k_z$	$k_y$	$k_z$	$k$
1	NREL 5 MW	0.0025	0.0024	-	-	-
2	INNWind 10 MW	0.018	0.02	0.011	0.016	0.027
3		0.045	0.045	0.029	0.029	0.0494
4	AREVA M5000	0.044	0.044	0.03	0.03	0.0488
5		0.038	0.038	0.027	0.027	0.0438

All those analytical models were compared using the benchmark data sets from cases 2-5, which cover the full-wake regions. It should be noted that the calibrated values in Table 2 are not the universal values of the related parameters, thus it needs to be adjusted case by case. This limitation will become a subject of future work to derive the universal expression of the expansion parameters under different flow field conditions.

#### 4.3.4 Model performance evaluation

To evaluate the effectiveness of the proposed model and the other analytical models quantitatively, the root-mean-square error (RMSE), the standard deviation of residuals or errors, is employed. The general formula is as follows:

$$RMSE = \sqrt{\overline{(u_{\text{expr}} - u_{\text{est}})^2}}, \quad (4. 29)$$

where  $u_{\text{expr}}$  is the measured velocity,  $u_{\text{est}}$  is the estimated velocity, and the overbar ( $\bar{\quad}$ ) means the average of residuals from evaluated data points at the specific direction. In the present study, the directional RMSE, which is based on the evaluated directions at each downstream distance  $x/D$ , is calculated as follows:

$$\textit{Directional RMSE} = \overline{RMSE_{dir}}, \quad (4.30)$$

where *dir* covers lateral, vertical, and streamwise directions. Meanwhile, the average RMSE, which represents the directional RMSE along the evaluated downstream distances within the evaluated region, is expressed as follows:

$$\textit{Average RMSE} = \overline{\textit{Directional RMSE}_{x/D}}. \quad (4.31)$$

Finally, the total RMSE, which represents the average RMSE for overall evaluated incoming velocities of the respective cases, is defined as follows:

$$\textit{Total RMSE} = \overline{\textit{Average RMSE}_{U_0}}. \quad (4.32)$$

## 4.4 Results and discussion

### 4.4.1 Streamwise wake velocity of NREL 5 MW HAWT within a near-wake region

The high-fidelity LES simulation was conducted to provide the details of the wake flow behavior, particularly streamwise velocity distribution within the near-wake region. To focus only on the turbine-induced wake, therefore, mean reference velocity  $U_0$  at the inlet was conditioned uniform without turbulence. Since the NREL 5MW HAWT model was simulated according to its full-scale size, thus the Reynolds number was on the order of  $10^7$ , which is typical for MW-class large wind turbines. Pairs of wake profiles in lateral and vertical directions resulting from the simulation and its prediction by the proposed DG model are shown in Figs. 4.4 and 4.5, respectively.

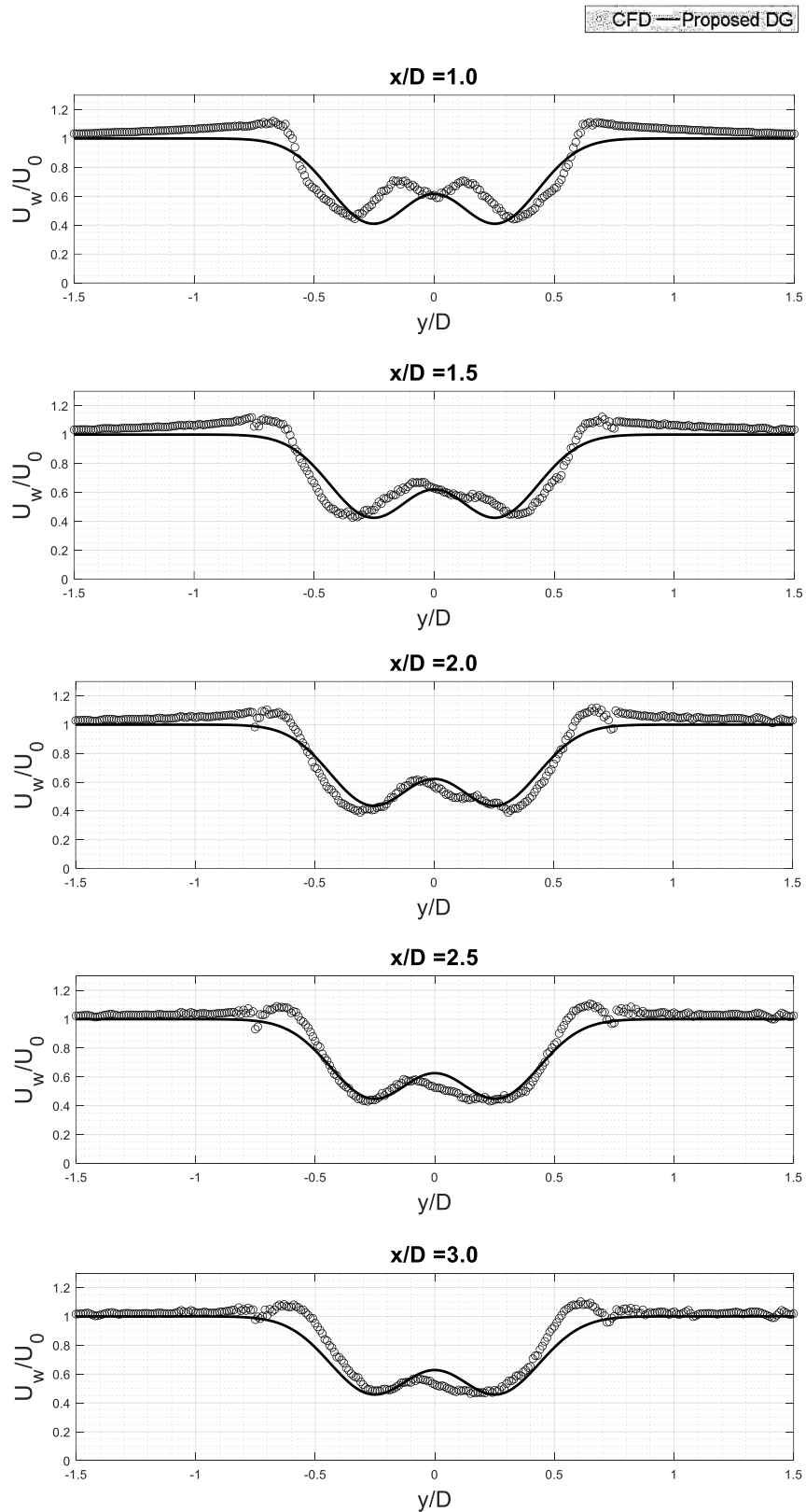


**Figure 4. 4.** Streamwise wake velocity profiles of NREL 5MW HAWT in the lateral direction within the near-wake region.

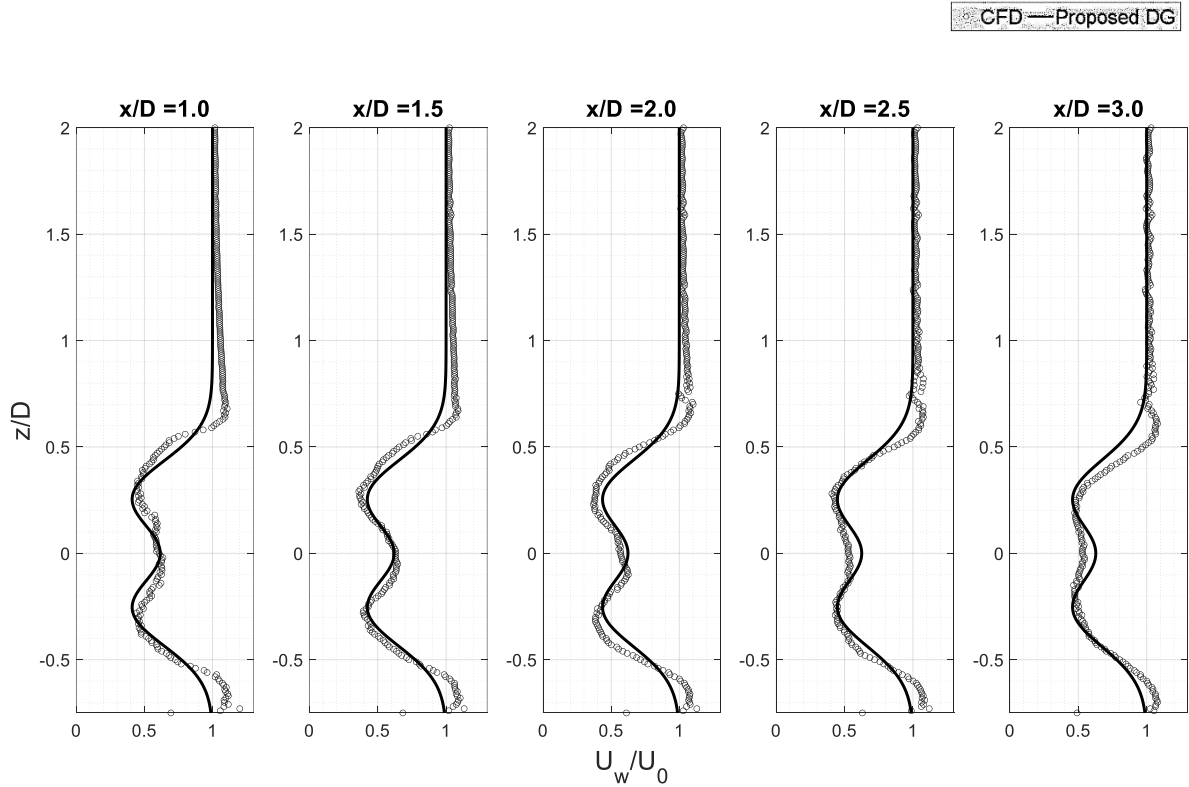


**Figure 4. 5.** Streamwise wake velocity profiles of NREL 5MW HAWT in the vertical direction within the near-wake region.

Referring to the CFD results as depicted in Figs. 4.4 and 4.5, the DG shape was clearly observed within the near-wake region. The appearance of this DG profile shape has been explained by a very small lift generated around the blade root as the result of its suboptimal shape and the lift is further reduced at the blade tip due to tip vortices [2]. This causes a less significant velocity deficit around these regions. Consequently, the wake velocity is still high around the blade root region and almost regained to its undisturbed velocity, particularly around the tip region. Meanwhile, the optimum lift is generated about the mid of the blades, causing a significant velocity deficit around those positions. Thus, minimum lift around the root and tip of the blade and maximum lift about the mid-blade position create two local minima that formed the DG velocity profile distribution within the near-wake region.

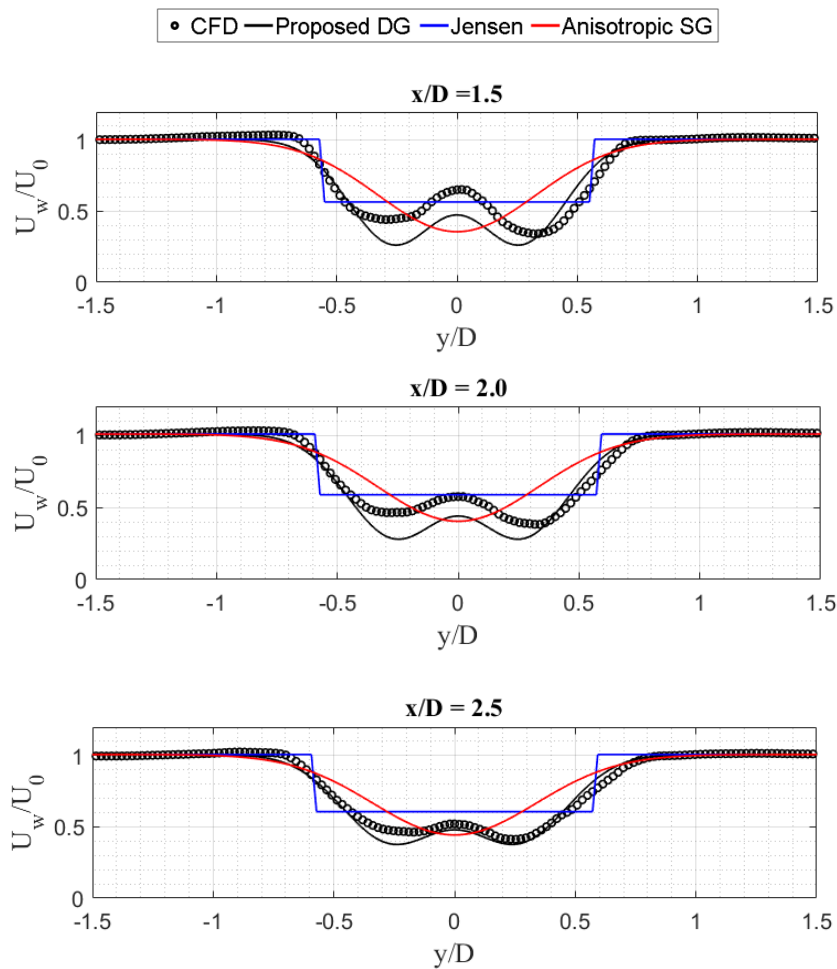
At the downstream distance just behind the turbine  $x/D = 1.0$ , the streamwise wake velocity around the hub center position ( $y/D = 0$ ) was slightly lower than its surrounding due to the nacelle blockage effect. However, this near-wake appearance was not clearly observed for the vertical direction at the same downstream distance. As the downstream distance increased, the effect of the blockage was slowly faded, thus resulting in a smoother transition of the wake shape between the hub center and its surroundings. This occurrence created a clear double-Gaussian (DG) shape within the near-wake region.

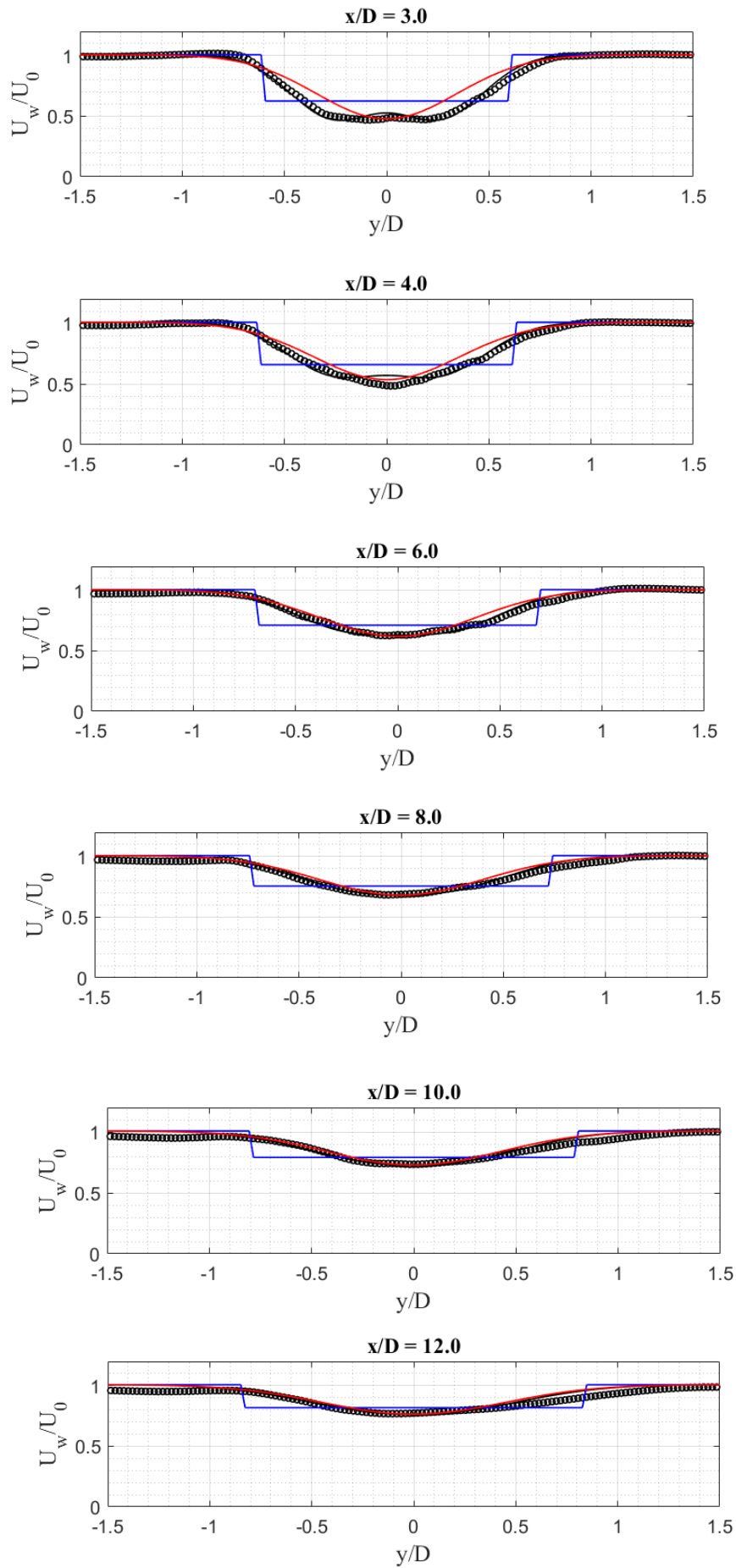
The same behavior was still observed until the domain's outlet. Moreover, it was found that the wake recovery was so slow since the DG shape distribution was still salient at the domain's outlet. This occurrence is reasonable since the onset of the far-wake region is inversely proportional to the incoming

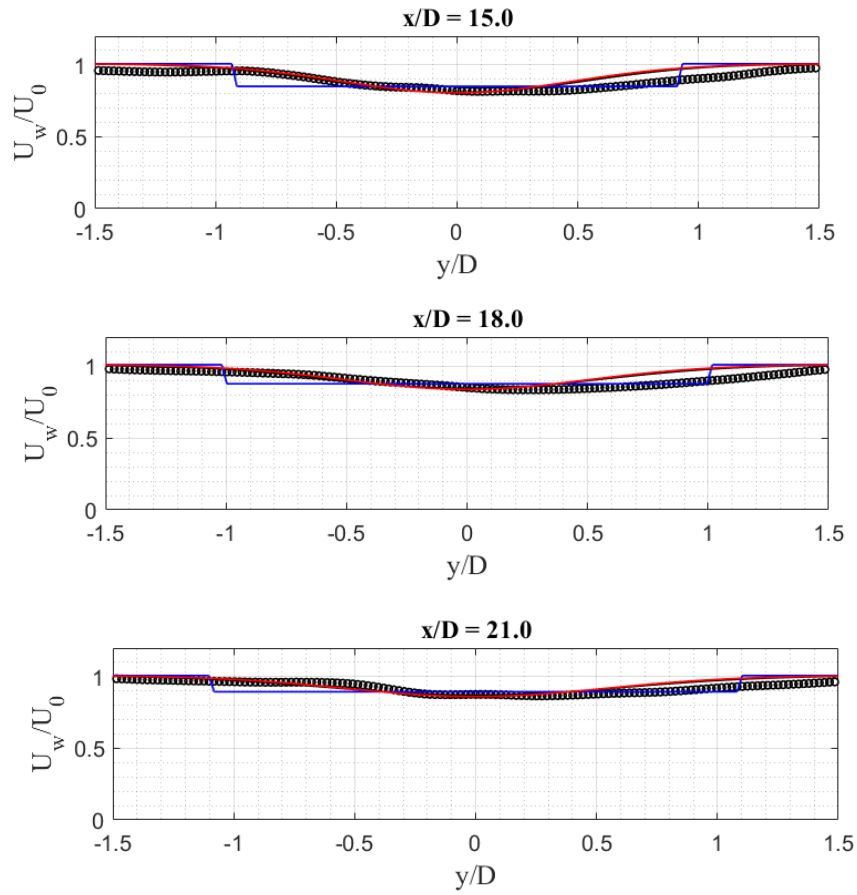
streamwise turbulence intensity. Therefore, the transition from the DG to the SG shape profile becomes farther from the turbine, particularly when the incoming turbulence intensity is zero. It also makes the wake growth rates are slow. From those CFD results, it is confirmed that the proposed DG model shows its effectiveness in predicting streamwise wake profile within the near-wake region. In this case, the best fit of wake growth rates in lateral and vertical directions were about 0.0025 and 0.0024. This means that the wake spreads anisotropically.

#### 4.4.2 Streamwise wake velocity of INNWIND 10 MW HAWT within a full-wake region

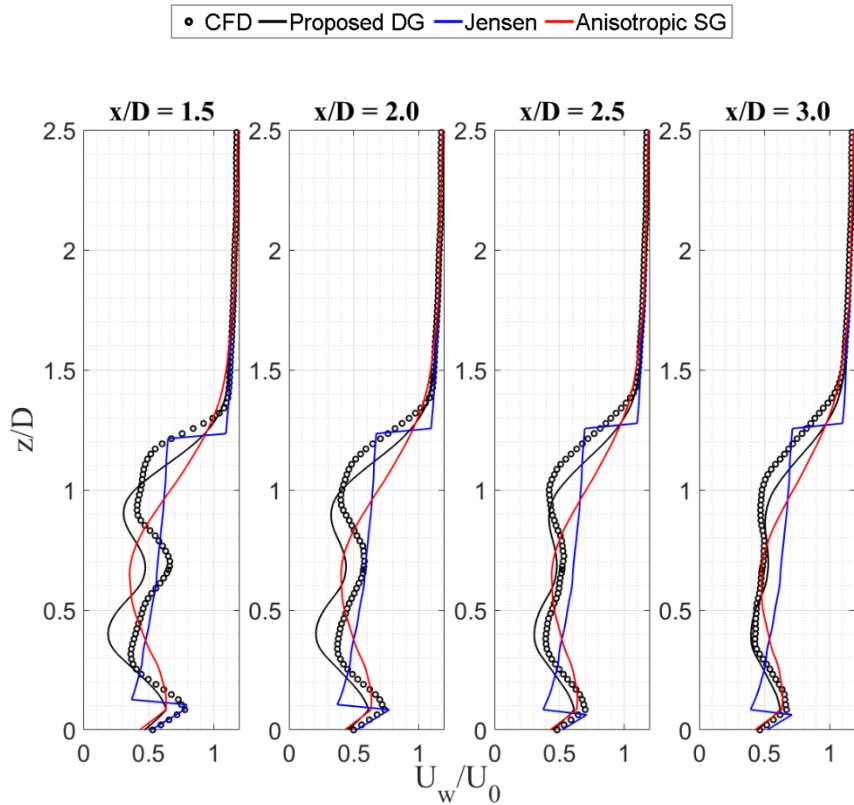
Pairs of streamwise wake velocities in lateral and vertical directions were used to evaluate the effectiveness of the proposed DG model within the full-wake region behind an isolated HAWT. Therefore, the LES simulation data of a utility-scale INNWIND 10 MW HAWT were used. The turbine was operated under ABL with incoming streamwise turbulence intensity of  $\approx 5\%$ . In addition, the Jensen and anisotropic SG models were examined for comparison. Those models are known for their robustness for wake velocity estimation within the far-wake region. The predictions of mean wake profiles of INNWIND 10 MW HAWT in lateral and vertical directions are shown in Figs. 4.6 and 4.7, respectively.







**Figure 4. 6.** Streamwise wake velocity profile of INNWIND 10 MW HAWT in the lateral direction within a full-wake region.



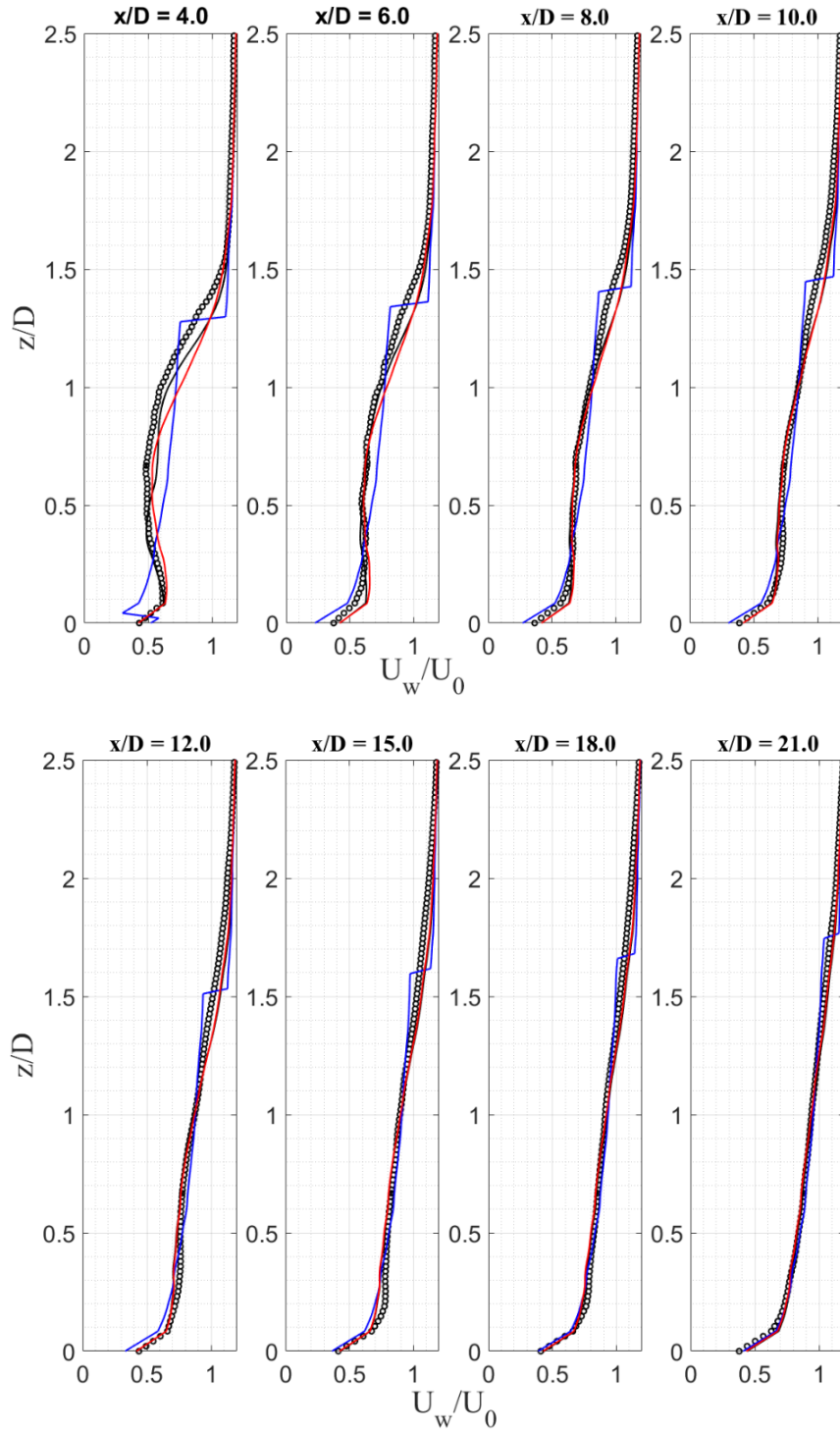


**Figure 4. 7.** Streamwise wake velocity profile of INNWIND 10 MW HAWT in the vertical direction within a full-wake region.

Within the near-wake region, the proposed DG shape could better reproduce the wake shape distribution in both lateral and vertical directions among the other examined models. However, at the downstream distance up to about  $x/D=2$ , the DG model underpredicted the wake deficit value in both directions. This underprediction was mainly due to the acceleration term in the momentum equation, where the model relied upon, being neglected for the sake of simplicity. Therefore, this underprediction

was reasonable since within the distance just behind the turbine, acceleration is more likely to happen because of the significant effect of internal turbulence generated by the turbine. As the downstream distance increased, the internal turbulence effect on the wake flow field gradually decreased, thus allowing the DG model to better estimate the velocity deficit, as it can be seen starting around  $x/D=2.5$ .

The transition from the DG to SG shape was found to occur at about  $x/D=4$ , which represented the onset of the far-wake region. The predictions from the proposed DG and the anisotropic SG model were almost similar at the wake centerline around the hub height. Nevertheless, the Jensen model overpredicted its values up to about  $x/D=12$ . This was mainly due to the isotropic approach being used for the wake expansion in this model, which caused an overprediction of the wake area, thus resulting in an overestimation of the streamwise wake velocity. Hence, the anisotropic behavior of the wake expansion becomes essential to be considered for a better estimation of the wake velocity, particularly within the far-wake region.

Basically, the proposed DG model and the anisotropic SG model rely upon the same simplification of the momentum equation and by ensuring the conservation of mass and momentum. This assumption makes both models almost have the exact estimation for the wake profiles within the far-wake region, which can be observed from Figs. 4.4 and 4.5 at the downstream distance of  $x/D \geq 6$ . Meanwhile, for the downstream distance  $x/D < 6$ , the SG model overpredicted the wake shape distribution, azimuthally in the area between the blade mid-span and tip. On the contrary, the model underpredicted its values when approaching the wake centerline, which can be observed up to  $x/D=2.5$ . Afterward, the accuracy of velocity deficit prediction along the centerline improved. These results re-emphasize the major drawback of the anisotropic SG model regarding its lack of accuracy within the near-wake region, where the wake flow is highly affected by the detailed features of the turbine, such as turbine characteristics and geometry. This drawback is reasonable since the SG-based models are based on a pragmatic approach where the wind turbine micro siting is commonly placed inside the far-wake region, thus the near-wake region is not of interest. To address this shortcoming, the proposed DG model considers the influence of the rotor presence within the near-wake region resulting in a better estimation of the formed DG shape and taking into account the anisotropic behavior of wake expansion, thus increasing its usability under different atmospheric stabilities.

#### **4.4.3 Wake velocity centerline of utility-scale AREVA 5 MW HAWT within a full-wake region**

Inside the wake region, the wake centerline was located approximately downstream of the rotor center at the hub height level. Along this centerline, the maximum velocity deficit occurred, particularly within the near-wake region. The processed lidar data of the mean velocity profile (ten minutes averaged) along the wake centerline behind utility-scale AREVA M5000 HAWT were used to investigate this behavior further. In this study, the lidar data were utilized as an experimental benchmark to evaluate the effectiveness of the proposed and the other examined models for the wake centerline prediction. Since the analyzed wake data are only a function of the downstream distance  $x/D$ , one-

dimensional fitting is sufficient for each analytical model to estimate the wake centerline profile at the hub height level. The measurement results and their estimations from each analytical model are shown in Fig. 4.8.

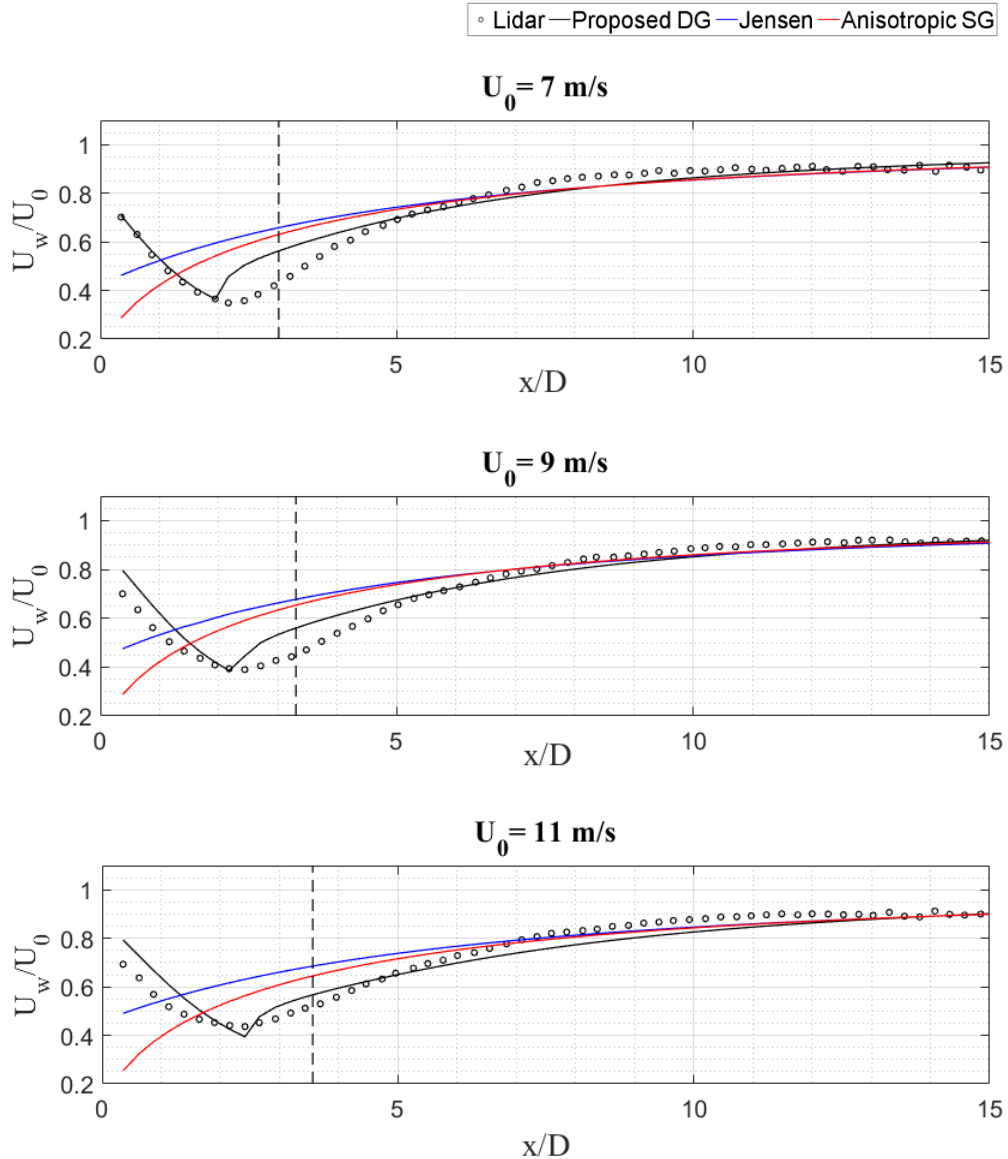


**Figure 4.8.** The wake centerline profile downstream of the AREVA 5MW HAWT at different incoming streamwise velocities.

From Fig. 4.8, the wake velocity centerline profile had the maximum velocity deficit of about  $x/D \approx 2$  downstream of the turbine. However, its magnitude increased slightly when the inflow velocity was higher. Notable results were also found regarding the wake expansion under different incoming streamwise turbulence intensities. For the analyzed lidar cases, as the inflow velocity increased, the incoming turbulence and the wake growth rate became weaker. This behavior can be seen from the centerline profile, where the wake recovered faster at the higher turbulence intensity. In this case, the fastest recovery happened at the incoming velocity of 7 m/s. The dependence of turbulence intensity on

the wake recovery rate can be represented by the onset of the far-wake region as formulated in Eq. 4.25. Since the onset of the far-wake is conversely proportional to the incoming turbulence, therefore for higher turbulence intensity, the wake recovers faster. This behavior has been confirmed by the analyzed utility-scale wake measurements, as shown in Fig. 4.8 where the onset of the far-wake region became closer to the turbine as the turbulence rose. This occurrence is marked by black-dashed vertical lines in the figure.

In general, the wake growth rates from all examined analytical models show the same tendency, where their tuned values increased with the higher turbulence intensity. This means that the turbulence intensity is worth to be considered for analytical wake modelling, particularly to get a better understanding of the wake recovery rate. From Fig. 4.8, it was observed that within the near-wake region, particularly from the downstream distance just behind the turbine to the distance where the maximum velocity deficit occurred ( $x/D \approx 2$ ), the DG model provided a better estimation of the wake centerline profile compared to the other analytical models. The onset of the far-wake region estimated by Eq. (4.25) in the analyzed cases is at  $3.0 < x/D < 3.6$ , which is still in the range for far-wake onset ranging from  $2-4D$  downstream of the turbine [4]. Around the onset of the far-wake region, the DG model outperformed the other models for the wake centerline prediction. However, its prediction slightly deviated observably starting from  $x/D \approx 6$ , where the model underestimated the centerline profiles. Afterward, the accuracy improved from  $x/D \approx 11$  for  $U_0 = 7$  m/s and  $x/D \approx 13$  for  $U_0$  of 9 and 11 m/s. Meanwhile, around the onset of the far wake region, both Jensen and Anisotropic SG models significantly overestimated the wake centerline from the overall reference velocities. Subsequently, the accuracy of these models was found improved started from  $x/D \approx 6$  for  $U_0 = 7$  m/s and  $x/D \approx 7$  for  $U_0$  of 9 and 11 m/s. Yet, the same trend of deviations for wake centerline prediction within the far-wake was also observed in both Jensen and Anisotropic SG models, specifically from  $x/D \approx 6$  for  $U_0$  of 7 and 11 m/s and  $x/D \approx 7$  for  $U_0$  of 9 m/s up to  $x/D \approx 12.5$  for the overall reference velocities.

Qualitatively, the evaluation of the analyzed wake models based on the available lidar data revealed that the DG-based model could give a better estimation of the wake centerline profiles within the near-wake to the far-wake regions about  $x/D \approx 6$ . Surpassing that downstream position, all the evaluated models offered a feasible prediction with relatively trivial errors against the measurement data. These errors might also be caused by the presence of downwind turbines or overlapping wakes at the far-field, thus leading to a deviation from the typical wake flow field behind an isolated HAWT. The possibility of these trivial errors made the prediction accuracies from the examined analytical models within the far-wake region were more acceptable.

#### 4.4.4 Statistical evaluation

This evaluation aimed to quantify the residuals between the proposed model and the other examined models against the benchmark wake data sets from utility-scale turbines using the root mean square

error (RMSE) statistical model. The previously evaluated cases from LES simulation and lidar measurements were used to further analyze the performance of the proposed DG and the other analytical models quantitatively. For the CFD results, only the wake data sets from SOWFA simulation for wake simulation behind an isolated INWIND 10 MW HAWT were evaluated further since it covers a full-wake region. Perfect wake model performance would give an RMSE value of zero.

In this study, the RMSE analyses from the examined wake models were categorized into four main regions: near-wake, far-wake, full-wake, and practical regions. Here, the near-wake region refers to the downstream distance between the turbine and the onset of the far-wake region, which is approximated using Eq. 4.25. Meanwhile, the far-wake region started from the onset of the far-wake region and beyond. Next, the full-wake region comprises the overall wake region ranging from the near to the far-wake regions. The last region is the practical region, which is based on the actual inter-row spacing between wind turbines in operational wind farms. This region ranges from  $x/D=2.4$ , used as the inter-row spacing between the installed turbines in 20 MW Middelgrunden offshore wind farm [58], up to  $x/D=11.0$ , which is around the maximum inter-row spacing between the turbines in specific wind direction ( $10.4D$  at  $\theta_{wind}=312^\circ$ ) within Horns Rev offshore wind farm [59]. It is expected that the set range for the practical region ( $2.4 \leq x/D \leq 11$ ) could cover all of the actual wind turbines micro-siting inside the operational wind farms nowadays thus the effectiveness of the examined wake models can be evaluated comprehensively.

The first case to be evaluated is from lidar measurements for wake centerline velocity profiles behind utility-scale offshore wind turbine AREVA 5MW HAWT. The performance of each model was examined into four main categories within the wake region (up to  $x/D=15$ ) resulting from different incoming velocities. In the present case, the onsets of the far-wake region according to Eq. (4.25) are  $\approx 3, 3.3,$  and  $3.56D$  for the incoming velocities of 7, 9, and 11 m/s, respectively. The evaluation results in terms of average RMSE for the near, far, and full-wake regions at the incoming velocities of 7, 9, and 11 m/s are shown in Figs. 4.9, 4.10, and 4.11, respectively.

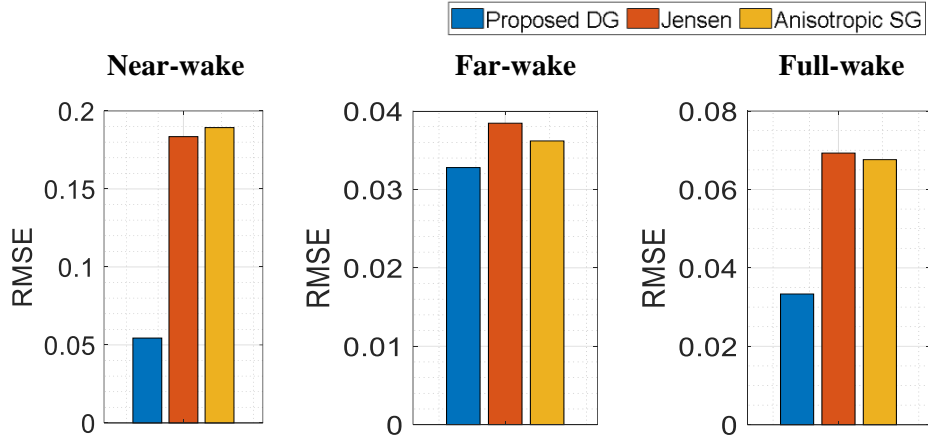


**Figure 4. 9.** Average RMSE against lidar measurement (case 3) within the near-wake, far-wake, and full-wake regions at the incoming reference velocity of 7 m/s.

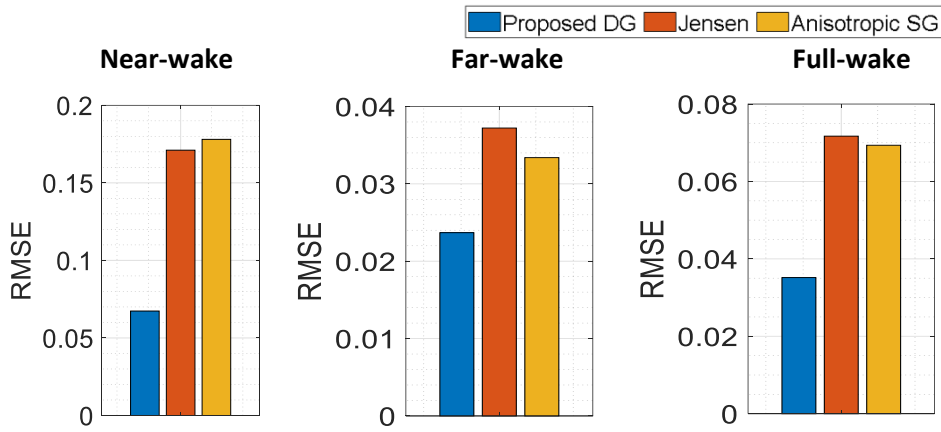


**Figure 4. 10.** Average RMSE against lidar measurement (case 4) within the near-wake, far-wake, and full-wake regions at the incoming reference velocity of 9 m/s.

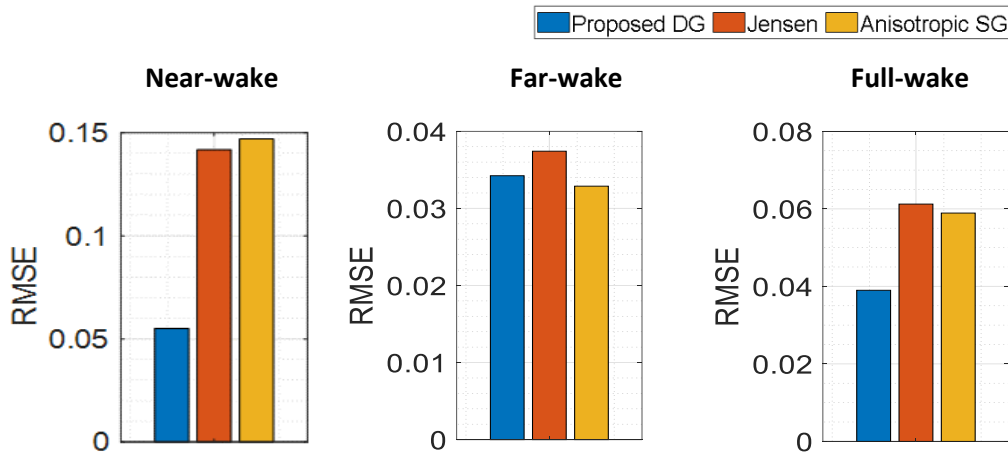


**Figure 4. 11.** Average RMSE against lidar measurement (case 5) within the near-wake, far-wake, and full-wake regions at the incoming reference velocity of 11 m/s.

From the RMSE results, the proposed DG model gave the most accurate prediction for the wake centerline profiles among the other examined models within the near-wake region. This is mainly due to the model's ability to reproduce the velocity degradation of the wake centerline profiles. Meanwhile,

It is interesting to note that the top-hat shape from the Jensen model outperformed the centerline prediction by the anisotropic SG model at each of the incoming velocities in the near-wake region. In contrast, the anisotropic SG model showed its robustness within the far-wake region by outperforming the prediction from the Jensen model at each incoming velocity and only at  $U_0$  of 11 m/s for the proposed DG model. On average, the RMSE results within the far-wake region showed comparable performance among the evaluated models, except for  $U_0$  of 9 m/s, where the proposed DG was much more precise than the others. For the full-wake analyses, the proposed DG provided the best estimation of the wake centerline, then followed by the anisotropic SG model and the Jensen model afterward. Finally, the total RMSE of each examined model is plotted in Fig. 4.12.

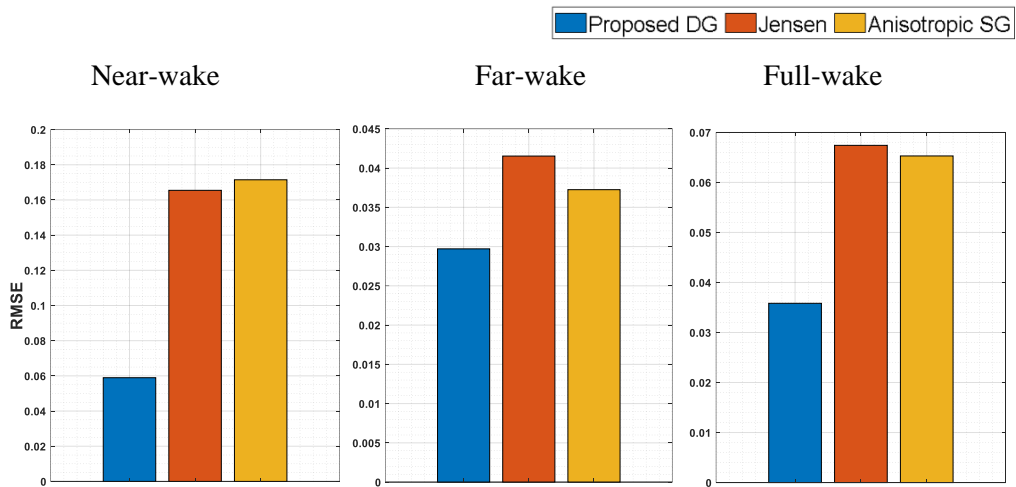
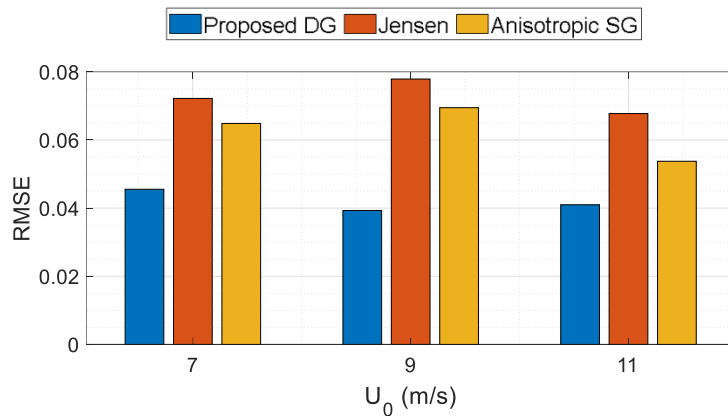


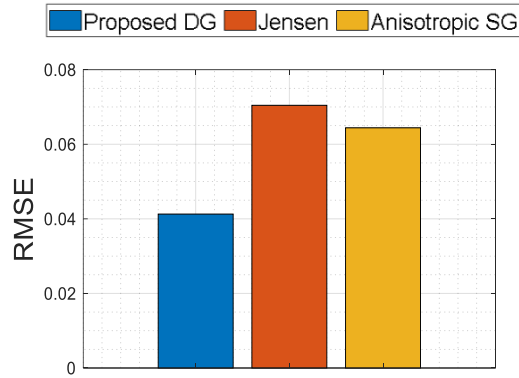
Figure 4. 12. Total RMSE against lidar measurements (cases 3-5) within the near-wake, far-wake, and full-wake regions.

Total RMSE in Fig. 4.12 was calculated based on the mean deviation for the wake centerline predictions under overall evaluated incoming velocities. The results revealed that the proposed DG has the best prediction within the near, far, and full-wake regions. The most notable performance from the proposed DG was its prediction accuracy within the near-wake region, which was significantly better than the other examined models. This evaluation result also reaffirms the limitation of the Jensen and anisotropic SG model, which are unsuitable for the wake centerline estimation within the near-wake region. It is also interesting to note that the proposed DG model had the best accuracy among the other models, even in the far-wake region. This was plausible due to the DG model's capability to roughly model the wake centerline transition between the near and far-wake regions. As a result, its accuracy around the onset of far-wake became better than the other models, thus enhancing its overall performance within the far-wake region and likewise in the full-wake region. It was observed that within the full-wake region, the Jensen model was least accurate among the other models. However, its prediction was not so different from a more complex anisotropic SG model and still relatively good for a simple top-hat shape approach being used.

The last category is the practical region, which covers the minimum to the maximum inter-row spacing between the actual wind turbines in operational wind farms. The average RMSE evaluation for each evaluated turbine at each incoming velocity within this region is shown in Fig 4.13. Meanwhile, the total RMSE resulting from each model at the overall evaluated incoming velocities is shown in Fig. 4.14. The proposed DG model had better performance than the other examined models for the given incoming velocities and followed by the anisotropic SG model and the Jensen model, respectively. Averaged from the practical region, the proposed model gave much better performance over the other models as expected. This was mainly due to its robust performance, particularly around the onset of the far-wake region, which significantly strengthens its overall performance. Otherwise, the inability of both Jensen and Anisotropic DG models to reproduce the centerline profile around the onset of the far wake region made those models work effectively after  $x/D \approx 6$  based on the analyzed lidar cases. The trend was the same, where both models significantly overestimated the wake centerline profiles at each evaluated incoming velocity around the onset of the far-wake region. Since the available wind energy is the cube of wind velocity, thus this significant overestimation may bring a significant error in predicting the energy output, particularly in tightly packed wind farms.

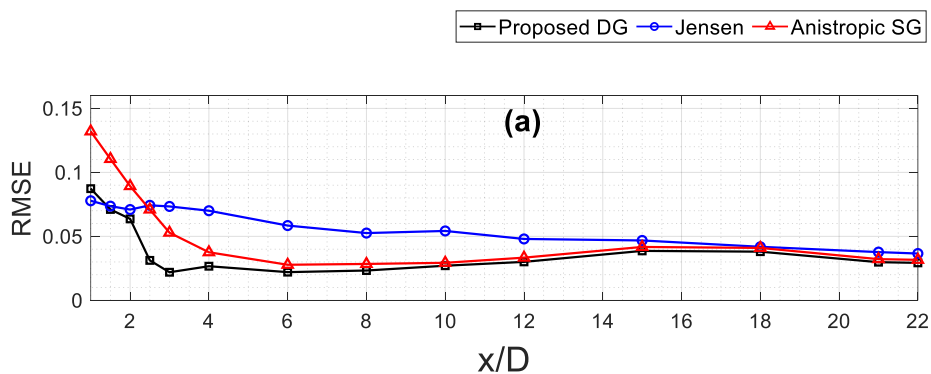


**Figure 4. 13.** Average RMSE against lidar measurements (cases 3-5) within the practical region at different incoming streamwise velocities.



**Figure 4. 14.** Total RMSE against lidar measurement (cases 3-5) within the practical downstream distance.

It should be noted that the lidar data were obtained from the wake centerline measurements in the streamwise direction to represent the wake velocity recovery. Therefore, for the sake of completeness, further wake evaluations that consist of RMSE analysis of the wake expansion in both lateral and vertical direction along a full-wake region are still needed to comprehensively examine the evaluated model performances. Therefore, pairs of directional streamwise wake expansions (in lateral and vertical directions) resulting from CFD simulation behind an isolated utility-scale INWIND 10 MW HAWT were used to achieve this purpose. The wind turbine was simulated under ABL with incoming turbulence. The onset of the far-wake region was located at  $x/D=4.41$ , according to Eq. 4.25. The wakes were numerically measured along the downstream distances ranging from  $1 \leq x/D \leq 22$  on cross-sectional planes, which centralized from the hub center towards  $1.5D$  blade span of both sides (+ and -) of each of the lateral and vertical directions. The evaluation results of directional RMSE for the wake profile prediction are shown in Fig. 4.15.



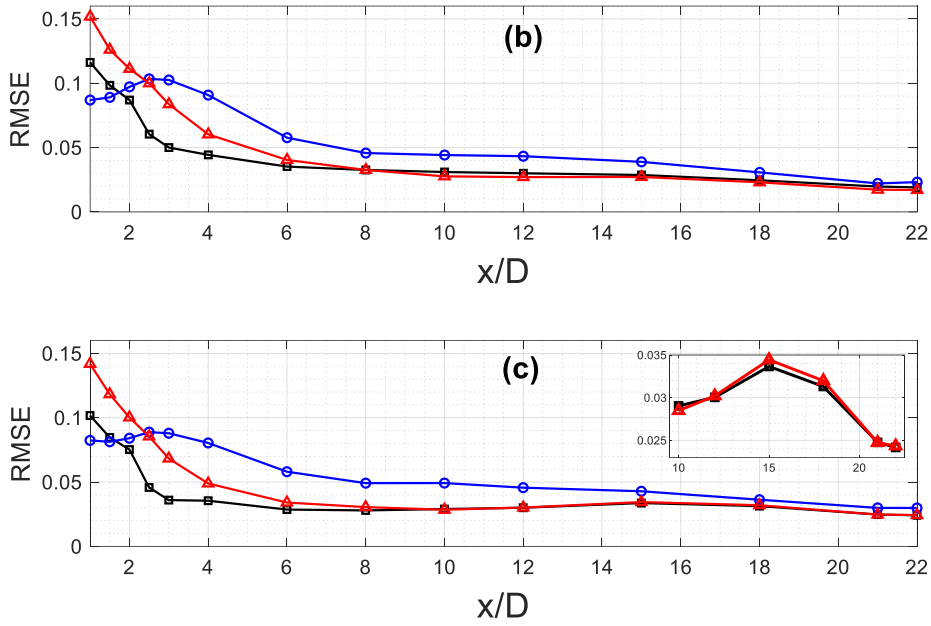


**Figure 4. 15.** RMSE against LES simulation of INWIND 10 MW (case 2) at different directions. (a) lateral direction; (b) vertical direction; (c) all directions.

Figs. 4.15(a) and (b) show the directional deviations of the examined wake models against the CFD data for wake profile predictions in lateral and vertical directions, respectively. Meanwhile, Fig. 4.15(c) displays the average deviations in both directions along the evaluated downstream distances. Starting with the simplest wake model, the top-hat shape approach from the Jensen model had the least accurate prediction of the wake profiles among the other models. It was observed that the residual gap between this top-hat model and the Gaussian-based models was significant until  $x/D=18$ , where the largest gap area was found in the lateral direction. This occurred mainly due to its top-hat simplification for the wake distribution, which in reality tends to form a Gaussian shape. Therefore, as long as the wake velocity has yet to recover significantly, the overall disparity of the wake distribution towards the blade span direction will remain prominent. However, its prediction for the streamwise wake centerline may improve faster after the onset of the far-wake region as in the previous lidar cases.

On average, the proposed DG performance within the near-wake region was better than the other models. Its prediction almost coincided with the anisotropic SG model at further downstream distances but with lower residuals, observably starting from  $x/D=6$ . This statistical result also points out the effectiveness of the proposed model within the far-wake region. It is also interesting to note that the anisotropic SG model showed its robustness from  $x/D=6.0$ , which is consistent with the analyzed lidar cases. This observation emphasizes the SG model compatibility for wake prediction that started from the downstream distance of  $6D$  behind the turbine. Furthermore, its accuracy, especially the Jensen model, was not so good around the onset of the far-wake region either in the present CFD case or previous lidar cases. This drawback could become another advantage of the proposed DG model among the other examined models for its effectiveness around the onset of far-wake.

The average RMSE evaluation of the wake model performance based on wake regional categories is shown in Fig. 4.16. Within the near-wake region, the proposed DG had the best accuracy for wake profile estimation in both lateral and vertical directions among the other models then, followed by Jensen and anisotropic SG models, respectively. Meanwhile, the anisotropic SG model outperformed the Jensen model performance in the far-wake region. There was less difference in the overall deviations between the proposed DG and anisotropic SG models within the far-wake region, mainly due to the similarity of the Gaussian approach being used, particularly when the DG shape profile has transformed into the fully SG shape profile. Nonetheless, the proposed DG model still provided the best accuracy among the other models in this region. Next, the RMSE result for wake profiles within the full-wake region showed that the proposed DG had the best accuracy along the evaluated wake region behind the turbine and was followed by anisotropic SG and Jensen models, respectively. In addition to the DG model's ability to model a single wake shape within the far-wake region, the model capability to predict the wake shape transition, which tends to form a flat-like shape from around the blade mid-span to the wake center, becomes its another advantage that might be difficult to reproduce by the other examined models.

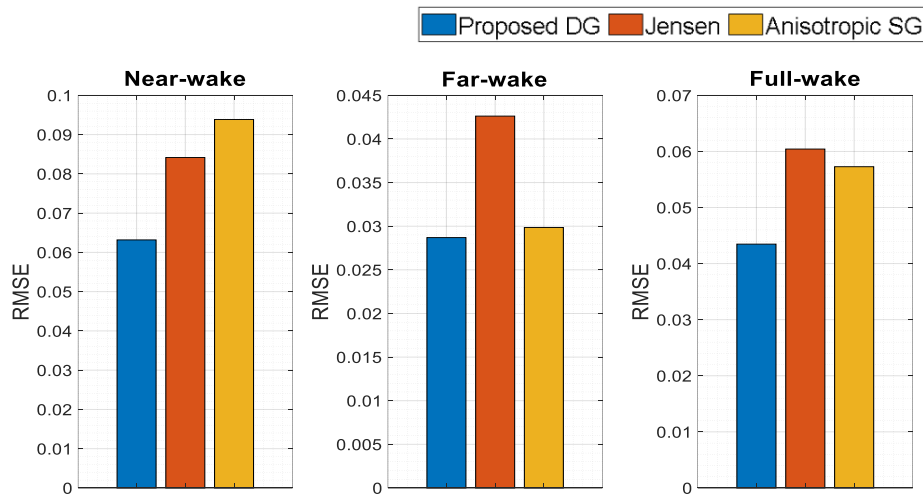


**Figure 4. 16.** Average RMSE against LES simulation of INWIND 10 MW (case 2) within the near-wake, far-wake, and full-wake regions.

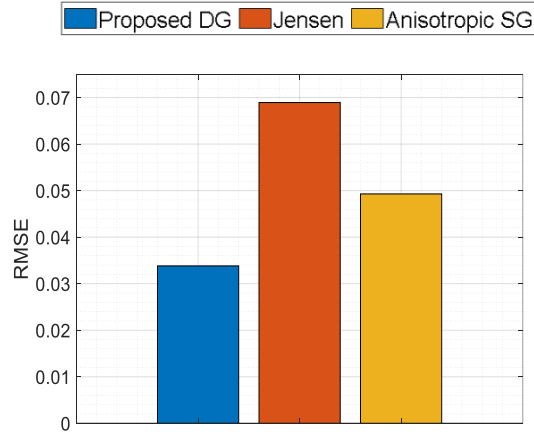


**Figure 4. 17.** Average RMSE against LES simulation of INWIND 10 MW (case 2) within the practical downstream distance.

Finally, the average RMSE within the practical region is presented in Fig. 4.17. The average deviation along the evaluated region showed that the proposed DG model had the best fit against the benchmark CFD data sets. It was observed that the inaccuracy of the Jensen model prediction within the practical region was inevitable due to the top-hat shape assumption being used, which is not consistent with the actual wake profile shape. Meanwhile, the performance of the SG model in this region was much better than the Jensen model. However, its significant deviations from the beginning of the practical region to around the onset of the far-wake negatively affected its whole performance in the practical region. Thus, the proposed DG still outperformed its performance. As mentioned previously, the proposed DG model has an advantage regarding its higher accuracy among the other examined models, particularly within the near-wake region to around the onset of the far-wake region, which is beyond the scope of the conventional approach for analytical wake modeling. Hence, the proposed model could be employed to fill this gap by offering a better estimation for the wake prediction, without exception around the onset of the far-wake region.

#### 4.5 Conclusion

A DG model for analytical wake modeling is proposed to complement the previously developed DG model in predicting the streamwise velocity distribution behind an isolated non-yawed horizontal-axis wind turbine (HAWT). The anisotropic nature of the wake growth rate downstream of the wind turbine is considered, thus facilitating the model's usability under different atmospheric stabilities. Moreover, constant values of the radial position of Gaussian minima  $r_0$  and scale factor  $c$  in Eq. (4.25), which were determined empirically, are suggested for the DG-based wake modeling behind utility-scale HAWTs. Finally, the effectiveness of the proposed model was validated against LES simulations and lidar measurements of the wake flow field behind utility-scale wind turbines.

The validation results showed that the proposed model could well reproduce the DG shape of the wake profiles within the near-wake region. Meanwhile, a single Gaussian like wake shape distribution

within the far-wake region could also be well estimated by the proposed model, thus confirming its compatibility within a full-wake region. Furthermore, a comprehensive evaluation was performed to examine the model performance under different inflow conditions and wake regions using RMSE statistical analysis. In general, the proposed DG model provided a feasible prediction within all wake region categories and outperformed the other examined wake models. It was found that the model has an advantage regarding its higher accuracy within the near-wake to around the onset of far-wake, which is beyond the scope of the conventional approach for analytical wake modeling. Thus, the proposed model may have the potential to give a better prediction for the wake flow field within tightly packed wind farms with relatively low computational cost.

In the proposed model, the wake growth rate parameters still needed to be tuned case by case. This limitation will be considered in future work to determine the universal expression for the parameters based on the different flow field conditions. In addition, some wake flow fields resulting from high-fidelity LES simulation will be employed to achieve this goal.

## Chapter 5

# A linear wake expansion function for the DG analytical wake model

### *Attribution*

*Q. M. B. Soesanto, T. Yoshinaga, and A. Iida, "A linear wake expansion function for the double-Gaussian analytical wake model," Energy Sci. Eng., In press, 2023, doi: <https://doi.org/10.1002/ese3.1427> is made available under the terms of the Creative Commons Attribution License (CC BY 4.0), with minor modification.*

### 5.1 Overview

The DG approach for analytical wake modeling leads to a better understanding of the wake transition mechanism within a full-wake region behind a non-yawed HAWT. To date, a key parameter of the wake expansion in the DG model still has yet to be defined explicitly instead of tuning, thus limiting its usability for practical applications. The present work aims to overcome this limitation by proposing a simple linear wake expansion function for the DG model constructed from the existing parameters based on the conservation of mass and momentum. Considering the physical and statistical approaches, the proposed function is specifically intended to approximate the wake expansion downstream of a non-yawed HAWT under turbulence inflow. Seven case studies from wind tunnel measurements and large eddy simulations under different inflow conditions were used to examine the effectiveness of the proposed function. In general, the evaluation results in the present study show the effectiveness of the proposed expansion function for the DG wake model to predict the wake expansion and its recovery behind a non-yawed HAWT without a prior adjustment or tuning of the wake expansion parameter.

### 5.2 Introduction

Wind energy exploitation is rapidly increasing worldwide due to its tremendous potential to supply a vast amount of clean energy for large-scale power generation. The development in wind turbine technology nowadays enables project developers to manufacture and operate megawatt-type HAWTs with hub heights of 100 meters or more [60]. When those HAWTs are integrated into a cluster with a specific array arrangement known as a wind farm, they could produce a total nameplate capacity up to the Gigawatt scale. Thus, the massive deployment of wind farms in onshore and offshore terrains could significantly contribute to decarbonizing electricity generation worldwide. However, any downstream turbines inside the wind farm will experience

power losses due to the upstream turbine's wakes, thus decreasing the overall power generation of the farm [61].

A HAWT wake can be defined as a plume-like region downstream of a wind turbine characterized by reduced wind speed and increased turbulence intensity [12]. Given the importance of wake aerodynamics on the overall wind farm performance, several investigations have been conducted to elucidate the wake behavior using an experimental [38], numerical [62], or analytical approach [5], [22], [26]. Among the other approaches, analytical modeling is known for its computationally inexpensive and less time-consuming of giving a practical prediction of the wake flow field, thus providing a relatively efficient solution for wind farm layout optimization methodology [4], [36]. Due to its suitability for practical applications, such as in the wind industry sector, the present study is focused on analytical wake modeling.

The wake shape distribution from analytical wake modeling is mainly divided into two based approaches: (1) top-hat (TH); (2) single-Gaussian (SG). However, the TH approach is a less accurate assumption to represent the shape of velocity deficit behind the HAWT since it generally forms the Gaussian distribution [5]. The SG models were designed to typically perform within the far-wake region where most downstream turbines are located. The HAWTs within a wind farm are commonly installed up to  $11D$  for the inter-row spacing. Within this inter-row distance, it was observed experimentally [5] and numerically [6], [28] that the single HAWT wakes expanded linearly under different turbine operating and inflow conditions. Thus, some existing wake models considered the linear expansion for the wake growth rate downstream of the turbine [5], [20], [21]. However, their expansion coefficients were determined empirically based on specific case studies, which may require additional tuning under more varying inflow conditions.

Since the SG-based approach was based on a practical perspective that focused on the far-wake region where most of the utility-scale downstream HAWTs were installed, thus the existing SG models may not give a satisfying result of wake velocity prediction within the near-wake region. This region is characterized by the double-Gaussian (DG) velocity distribution due to optimum lift around the blade mid-span and very small lift around the blade's root and tip [2]. The DG distribution is formed immediately after a significant velocity deficit around the centerline due to the nacelle blockage effect recovered by mixing with the faster air surrounding the nacelle. Since this significant centerline deficit recovered rapidly over a relatively short distance [63], thus the DG-based approach is still reasonable to represent the wake characteristic within the near-wake region.

By giving attention to this near-wake characteristic, Keane et al. laid the foundation of the DG analytical wake modeling based on the conservation of mass and momentum [48]. Later,

Schreiber et al [26] found some issues in the original DG formulation, which resulted in a nonphysical result inconsistent with the conservation equations; thus, some of the original expressions were rederived. Recently, Keane improved the original DG model, providing a viable wake velocity deficit function within the near-wake through the use of a complex solution, and introduced the effective rotor diameter as the entire extent of the DG wind velocity deficit [27].

It is worth noting that DG wake models also effectively predict the wake distribution and recovery within the full-wake region, which encompasses the near and far-wake regions. This advantage was confirmed using computational fluid dynamics (CFD) data, where the root mean square error results showed the superiority of the DG model against the SG model for lateral velocity deficit predictions within a full-wake region [26]. Most recently, the anisotropic DG model proposed by Soesanto et al. was compared to the anisotropic SG model referring to large eddy simulation (LES) and lidar data [63]. The results showed that the anisotropic DG model could perform better than the anisotropic SG model within the full-wake region, thus reconfirming the effectiveness of the DG-based wake model.

Although several attempts have been made to improve the reliability of the DG wake model, the practical use of this model is still difficult since the wake expansion parameter has yet to be defined explicitly instead of tuning. It should be noted that this expansion parameter controls the wake recovery development and eventually determines the accuracy of the wake velocity prediction. Since the wind power varies with the cube of wind velocity, the inaccurate prediction of the wake velocity would result in significant errors in power prediction.

Given the importance of the wake expansion parameter, the present work aims to construct a simple physically-based linear wake expansion function for the DG model incorporated from the existing parameters based on the conservation of mass and momentum. To the best of our knowledge, this is the first expansion function for the DG wake model that can be used directly without expansion parameter tuning. The validity of the proposed expansion function was examined with seven case studies of single HAWT wakes under different operating and inflow conditions. In addition, the tuning results from the existing expansion function were also evaluated for comparison. Finally, the effectiveness of the proposed function on the given case studies was evaluated using statistical measures in terms of NRMSE and R correlation coefficient.

## 5.3 Methodology

### 5.3.1 Linear wake expansion function for the DG analytical wake model

Based on turbine micro-siting practices, the HAWTs within a wind farm are rarely installed over  $11D$  for the inter-row spacing [63]. Within this spacing distance, it was observed both experimentally [5] and numerically [6], [28] that the single HAWT wakes expanded linearly under different turbine operating and inflow conditions. In analytical wake modeling, Jensen and Katic already considered linear expansion for the wake growth behind the HAWT with their top-hat wake model [20], [21]. In this model, the wake radius at the HAWT's rotor plane  $r_{w0}$  ( $x=0$ ) was assumed equal to the rotor radius ( $r_0$ ). However, by employing the rotor disc approach to simplify the rotor aerodynamics, the area over which the thrust  $T$  acting shall extend beyond the disc area, on the assumption that the thrust coefficient  $C_T$  is fixed [27]. Hence, the previous simplification regarding  $r_{w0}=r_0$  should be redefined to  $r_{w0}>r_0$  for a more detailed approximation of the wake radius at the rotor plane. This consideration is crucial to locate the outset from which the wake expands linearly within the practical inter-row turbine spacing. An illustration of linear wake expansion in the present study is shown in Fig. 5.1.

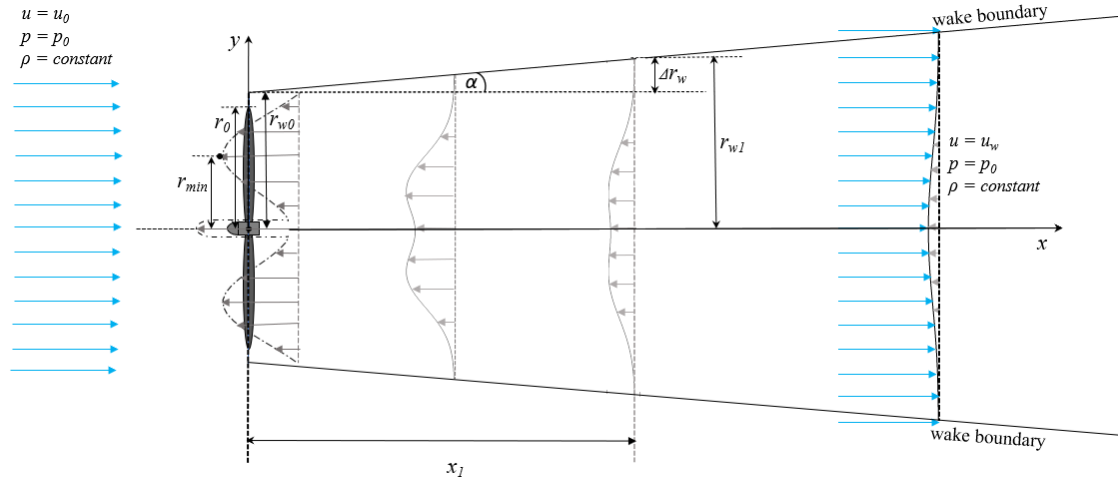


**Figure 5. 1.** Illustration of the proposed expansion function for the analytical DG wake model. The wake expands linearly in the lateral direction ( $y$ ) at the hub height ( $z=0$ ) along the distance  $x$  downstream of the rotor.

In the proposed function,  $r_{w0}$  should satisfy the condition  $r_{w0}>r_0$ . Based on the physical approach, Bastankhah and Porté-Agel derived a semi-empirical formula for the standard deviation of the SG velocity deficit profile at the rotor plane  $\sigma_{w0}$  [5]. Combining the existing  $\sigma_{w0}$  formula [5] with the statistical approach, thus  $2.58\sigma_{w0}$  that covers 99% values of Gaussian distribution [64] and satisfies the condition  $r_{w0}>r_0$ , is used to estimate  $r_{w0}$  in rotor diameter unit [ $D$ ] as follows:

$$r_{w0} = 0.516\sqrt{\beta}, \quad (5.1)$$

where  $\beta$  is expressed as [22]:

$$\beta = \frac{1}{2} \frac{1 + \sqrt{1 - C_T}}{\sqrt{1 - C_T}}. \quad (5.2)$$

Meanwhile, the standard deviation of velocity deficit at the onset of far-wake region  $\sigma_{w1}$  [D] can be approximated using the DG wake expansion at the stream tube outlet [26], which here is written using the following relation:

$$\frac{\beta}{8} \left( 1 - \sqrt{1 - \frac{2}{\beta} C_T} \right) = M(\sigma_{w1}) \frac{M(\sigma_{w1}) - \sqrt{M(\sigma_{w1})^2 - \frac{1}{2} N(\sigma_{w1}) C_T}}{2N(\sigma_{w1})}, \quad (5.3)$$

where  $M$  and  $N$  are the integral solutions for the amplitude function of velocity deficit in the DG-based approach, which is relied on the conservation of mass and momentum. Their formulations will be defined later. It would not be straightforward to obtain  $\sigma_{w1}$  from Eq. 5.3. Thus, it should be solved numerically, one of which is by employing the Matlab function *vpsolve*. After numerically solving  $\sigma_{w1}$ , the wake radius at the far-wake onset  $r_{w1}$  [D] located at  $x/D = x_1$  can be expressed as follows:

$$r_{w1} = r_{min} + 2.58\sigma_{w1}, \quad (5.4)$$

where  $r_{min}$  [D] denotes the radial position of Gaussian minima and its value has been determined empirically equal to  $r_{min}=0.26$  [63]. Meanwhile, the streamwise position of the far-wake onset,  $x_1$  [D], is approximated using the following formula [29], [63]:

$$x_1 = \frac{1 + \sqrt{1 - C_T}}{\sqrt{2c} \left( 4aTI_{x,hub} + 2b(1 - \sqrt{1 - C_T}) \right)}, \quad (5.5)$$

where  $a = 0.58$  and  $b = 0.077$  [29],  $c=1.2$  and  $r_{min} = 0.26$  [63], and  $TI_{x,hub}$  is the streamwise turbulence intensity of the incoming streamwise velocity at the hub height.

Here, the three primary parameters of  $r_{w0}$ ,  $r_{w1}$ , and  $x_1$  are incorporated to formulate the linear wake expansion function for the DG model. Since the wake expansion is assumed linear, the key parameter  $\alpha$ , which is the angle between  $r_{w0}$  and  $r_{w1}$  can be calculated using the following relation:

$$\alpha = \tan^{-1}\left(\frac{\Delta r_w}{x_1}\right), \quad (5.6)$$

where  $\Delta r_w = r_{w1} - r_{w0}$ . In a more general form, Eq. 5.4 can be rewritten using the following expression:

$$r_w(x) = r_{\min} + 2.58\sigma_w(x), \quad (5.7)$$

thus yielding:

$$\sigma_w(x) = \frac{r_w(x) - r_{\min}}{2.58}. \quad (5.8)$$

By employing Eq 5.6, The wake radius at any downstream distance  $r_w [D]$  can be calculated as follows:

$$r_w(x) = \left(\frac{r_{w1} - r_{w0}}{x_1}\right)x + r_{w0}. \quad (5.9)$$

After substituting Eq. 5.9 into Eq. 5.8,  $\sigma_w [D]$  can be rewritten as follows:

$$\sigma_w(x) = \frac{(r_{w1} - r_{w0})x + r_{w0}x_1 - r_{\min}x_1}{2.58x_1}. \quad (5.10)$$

Using the expressions above of  $r_{w0}$ ,  $r_{w1}$ , and  $r_{\min}$ , then Eq. 5.10 is expressed as follows:

$$\sigma_w(x) = \frac{(0.26 + 2.58\sigma_{w1} - 0.516\sqrt{\beta})x + 0.516\sqrt{\beta}x_1 - 0.26x_1}{2.58x_1}. \quad (5.11)$$

Finally, a more compact form of a linear wake expansion function for the DG model  $\sigma_w [D]$  is formulated as follows:

$$\sigma_w(x) = \frac{(0.1 - 0.2\sqrt{\beta} + \sigma_{w1})x}{x_1} + 0.2\sqrt{\beta} - 0.1. \quad (5.12)$$

As formulated in Eq. 5.12, the proposed expansion function can be used directly without tuning. It should be noted that this expansion function is only compatible for non-yawed single HAWT wakes under turbulence inflow, which also corresponds to the actual inflow condition where the utility-scale turbine operates. Hence,  $TI_{x,hub}$  becomes another input parameter for the expansion function in addition to  $C_T$ . The proposed function was applied to the existing DG wake model [63], as summarized in Table 5.1.

**Table 5. 1.** The normalized velocity deficit  $\Delta U/U_{hub}$ , the DG shape function  $f(r(y, z), \sigma(x))$ , and the DG amplitude function  $C(\sigma(x))$ .

$\Delta U/U_0$	$f(r(y, z), \sigma(x))$	$C(\sigma(x))$
$C(\sigma(x))f(r(y, z), \sigma(x))$	$\frac{1}{2} \left[ \exp \left( -\frac{1}{2} \left( \sqrt{\frac{y^2}{\sigma_y^2} + \frac{(z-z_h)^2}{\sigma_z^2}} + \frac{r_{\min}}{\sigma} \right)^2 \right) + \exp \left( -\frac{1}{2} \left( \sqrt{\frac{y^2}{\sigma_y^2} + \frac{(z-z_h)^2}{\sigma_z^2}} - \frac{r_{\min}}{\sigma} \right)^2 \right) \right]$	$\frac{M - \sqrt{M^2 - 1/2NC_T D^2}}{2N}$

where  $r$  [ $D$ ] is the radial distance from the wake center defined as  $r = \sqrt{y^2 + (z - z_h)^2}$ . The normalized wake velocity  $U_w/U_0$  within the cartesian coordinate system can be calculated using the following relation:

$$\frac{\Delta U}{U_0} = \frac{U_0 - U_w}{U_0} = C(\sigma(x))f(r(y, z), \sigma(x)), \quad (5. 13)$$

where  $U_0$  [m/s] is the reference streamwise incoming velocity at the hub height. The lateral ( $y$ ) and vertical ( $z$ ) directions are in the rotor diameter unit [ $D$ ]. It is worth noting that the rotor diameter parameter ( $D$ ) in the formulation for  $C(\sigma(x))$  from Table 1 is self-normalized, thus its quadratic value in that formula remains equal to one. Meanwhile, the definitions for  $M$  and  $N$  in Table 5.1 are expressed as follows:

$$M = 2\sigma_y\sigma_z e^{\frac{-r_{\min}^2}{2\sigma_y\sigma_z}} + \sqrt{2\pi}r_{\min}\sqrt{\sigma_y\sigma_z} \operatorname{erf}\left(\frac{r_{\min}}{\sqrt{2}\sqrt{\sigma_y\sigma_z}}\right), \quad (5. 14)$$

$$N = \sigma_y\sigma_z e^{\frac{-r_{\min}^2}{\sigma_y\sigma_z}} + \frac{\sqrt{\pi}}{2}r_{\min}\sqrt{\sigma_y\sigma_z} \operatorname{erf}\left(\frac{r_{\min}}{\sqrt{\sigma_y\sigma_z}}\right). \quad (5. 15)$$

It should be kept in mind that the wake expansion is assumed to be isotropic so that the expansion functions in the lateral direction ( $\sigma_y$ ) and vertical direction ( $\sigma_z$ ) are the same ( $\sigma_w = \sigma_y = \sigma_z$ ). Furthermore,  $M(\sigma_{w1})$  and  $N(\sigma_{w1})$  in Eq. 5.3 are calculated using Eqs. 5.14 and 5.15, respectively, by substituting  $\sigma_y$  and  $\sigma_z$  with  $\sigma_{w1}$  for the wake expansion at the far-wake onset. In Table 2, if  $M^2 - 1/2NC_T D^2 < 0$ , the solution is solved using the absolute value or modulus of a complex number [27]:

$$C(\sigma(x)) = \frac{\left(M^2 + \left|M^2 - 1/2NC_T D^2\right|\right)^{\frac{1}{2}}}{2N}. \quad (5.16)$$

### 5.3.2 Validation

In this study, seven case studies of non-yawed HAWT wake resulting from LESs and wind tunnel measurements were used to evaluate the effectiveness of the proposed expansion function. Since all case studies were configured under neutral atmospheric stability, all the analytical predictions in this study are only relevant to neutrally stratified atmospheric boundary layer without any thermal effects. Further information on the turbine's operating and inflow conditions in each case is shown in Table 5.2.

**Table 5. 2.** Case studies used to validate the proposed expansion function.

Case	Turbine	$D$ [m]	$Z_{hub}$ [m]	Method	Inlet profile	$U_0$ [m/s]	$C_T$	$TI_{x,hub}$ (%)	Data range
1	NREL 5 MW	126	95	LES -FFB	Uniform	11.4	0.67	3	Near- wake region
2								6.8	
3								11.6	
4	G1	1.1	0.8	Exp. – Wind Tunnel	Boundary layer	5	0.75	6.25	Full- wake region
5	INNWIND 10 MW	178.3	119	LES – SOWFA		7.87	0.77	5.1	
6						7.7	0.75	8.5	
7	NREL 5 MW	126	90	LES – EllipSys3D		8	0.79	16	

Cases 1-3 resulted from three-dimensional high-fidelity LESs using a noncommercial CFD solver FrontFlow/Blue (FFB) [51]. The solver uses the finite-element method (FEM) to solve the unsteady incompressible Navier-Stokes (NS) equations numerically. The reference turbine used was NREL 5 MW HAWT, developed by National Renewable Energy Laboratory (NREL) for research purposes [41]. Main components of the turbine, such as the rotor blades, tower, and nacelle, were directly modeled to provide detailed information of the flow field within the near-wake region. The computational domain of the FFB simulations consisted of about 360 million elements of structured hexahedral meshes. The simulations were running on the Japanese supercomputer Fugaku.

The data range of Cases 4-7 in Table 5.2 covers the full-wake region. In this study, the terminology of “full-wake region” means the wake data are selected from the near and far-wake regions,

but it does not certainly mean that the analyses must include all the downstream distances and start exactly from  $x=0$ . In Case 4, six selected downstream distances ( $x/D=1.7, 2, 3, 4, 6, \text{ and } 9$ ) from wind-tunnel measurements of the wake profile behind the G1 turbine model were cited from Schreiber et al [26]. Turbulent boundary layer inflow had the hub-height reference velocity ( $U_0$ ) $\approx 5$  m/s and the hub-height turbulence intensity ( $TI_{hub}$ ) $\approx 5\%$ . Since no specific direction was mentioned for the inflow turbulence, the  $TI_{hub}$  of the inflow was interpreted as the total  $TI_{hub}$  ( $TI_{total,hub}$ ). Thus, in the present study, the hub-height turbulence intensity in the streamwise direction ( $TI_{x,hub}$ ) of the incoming flow was approximated using the IEC 61400-1 standard, where  $TI_{x,hub} \approx TI_{total}/0.8$ , resulting in  $TI_{x,hub}$  of about 6.25%.

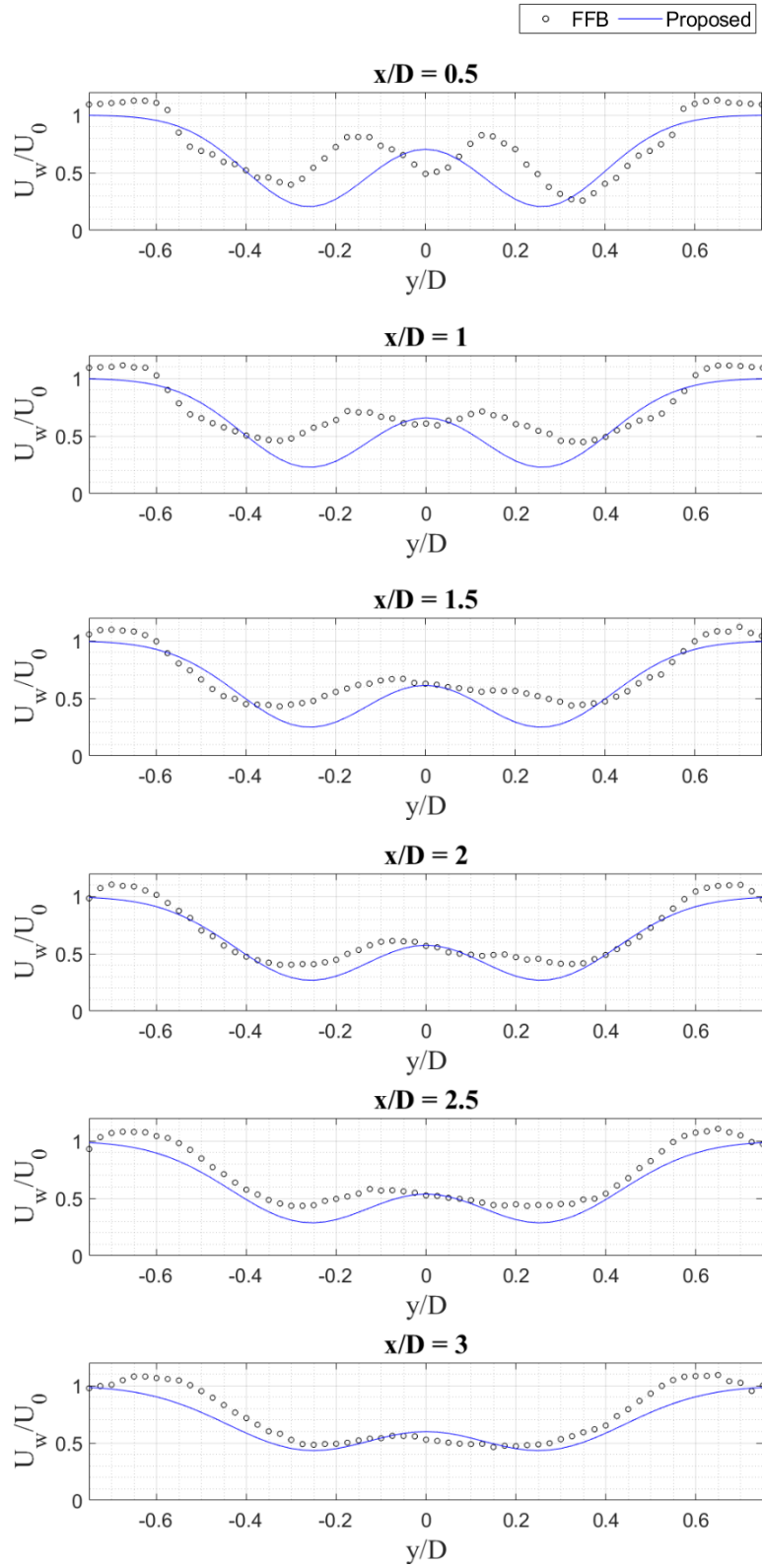
Ten selected downstream distances ( $x/D=1.5, 2, 3, 4, 5, 6, 7, 8, 10, \text{ and } 12$ ) in Cases 5-6 were cited from research data under CL-Windcon project for LESs of INNWIND 10 MW HAWT wakes using the LES solver for wind farm simulations, SOWFA (Simulator fOr Wind Farm Applications) [50], [52]. The rotor was indirectly modeled using the actuator line method. Meanwhile, the turbine's nacelle and tower were not modeled. The LES data from the last 600 s simulation time of the fully-developed wake flow field were processed for validation. The turbine was operated under turbulent boundary layer, with the reference velocity of  $U_0=7.87$  m/s and the incoming  $TI_{x,hub}=5.1\%$  in Case 5. Meanwhile,  $U_0=7.7$  m/s and the incoming  $TI_{x,hub} = 8.5\%$  for Case 6. Relatively low and medium incoming  $TI_{x,hub}$  from the selected datasets were considered realistic for offshore environments with flat terrain.

Ten selected downstream distances ( $x/D=1, 1.5, 2, 2.5, 3, 4, 5, 6, 7, 8$ ) of the wake dataset In Case 7 were cited from Technical University of Denmark (DTU) database for LES of NREL 5 MW wake [65] obtained using the in-house incompressible finite volume code EllipSys3D [66]. The indirect method for rotor modeling was used as the actuator disk with a fixed force distribution based on a rotor-resolved detached eddy simulation [65]. The HAWT wake was simulated under turbulent boundary layer with the reference velocity of  $U_0 = 7.87$  m/s and the incoming  $TI_{x,hub}$  of about 16%. The dataset represents an onshore situation with characteristically high  $TI_{x,hub}$ , possibly due to high ground surface roughness and the presence of complex terrain or obstacles.

## 5.4 Results and discussion

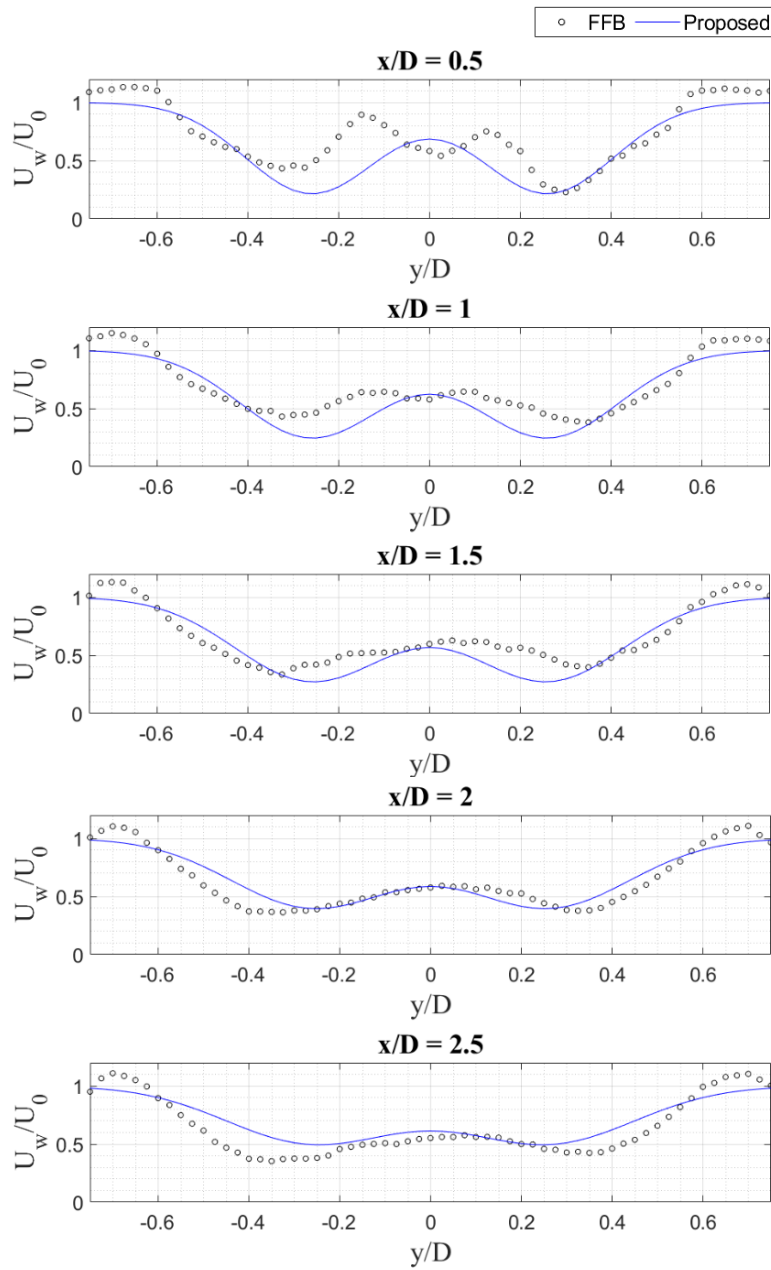
### 5.4.1 The near-wake region

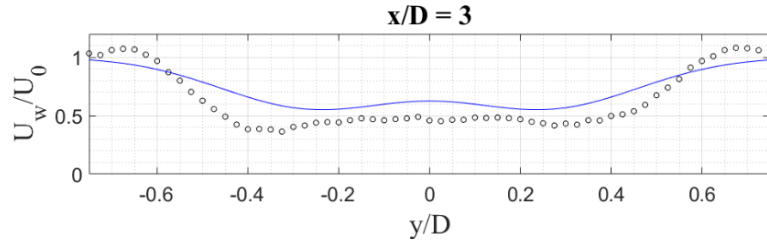
This section provides the LES-FFB results and their analytical predictions for Cases 1-3, focusing on the wake velocity distribution at the hub height in the lateral direction within the near-wake region. The wake profiles from Case 1 are shown in Fig. 5.2.



**Figure 5. 2.** Wake velocity profiles at the hub height under uniform inlet with  $U_0 \approx 11.4$  m/s and incoming  $TI_{x, \text{hub}} \approx 3\%$  within the near-wake region (Case 1).

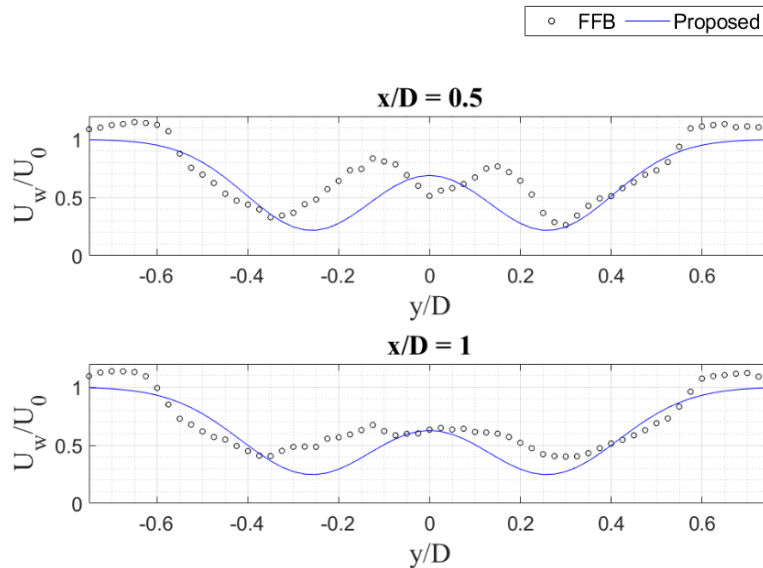
The high-fidelity LES results captured the influence of rotor geometry on the produced wake flow field indicated by the DG shape velocity profiles formed within the near-wake region. The proposed function could give reasonable predictions of the wake recovery at the centerline ( $y=0$ ,  $z=z_{hub}$ ), except for  $x/D = 0.5$ , where the wake velocity from LES gradually reduced towards the centerline due to the nacelle blockage effect. As the downstream distance increased, the blockage effect became insignificant, thus causing better agreement with the LES data. The LES results in Case 2 and their analytical estimations are shown in Fig. 5.3.





**Figure 5. 3.** Wake velocity profiles at the hub height under uniform inlet with  $U_0 \approx 11.4$  m/s and incoming  $TI_{x,hub} \approx 6.8$  % within the near-wake region (Case 2).

Case 2 was set under the same uniformly distributed inlet velocity as the previous case but with a higher incoming  $TI_{x,hub}$ . The wake recovery at the selected distances within the near-wake region is almost the same as in Case 1. The maximum velocity deficit around the blade mid-span gradually reduced as the downstream distance increased. The top-hat profile from the LES result around the blade mid-span position to the wake centerline at  $x/D=3$  might indicate the rotor presence's attenuation on the wake flow field. At the same downstream distance, the proposed function gave a faster wake recovery than the LES result, causing an overestimation of the wake velocity prediction. However, the proposed function could still provide a reasonable representation of wake recovery within the near-wake region, as indicated by decent estimations of the centerline velocity at the selected distances. Another LES result of the single HAWT wake under the ABL inlet with moderate  $TI_{x,hub}$  (Case 3) is shown in Fig. 5.4.



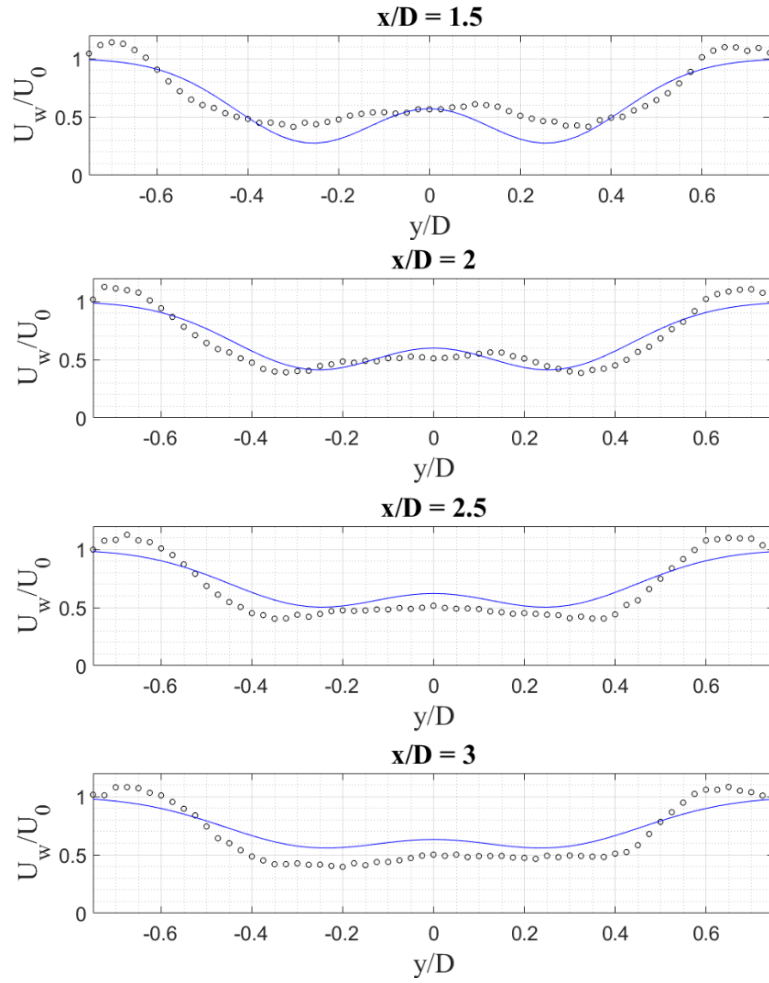


**Figure 5. 4.** Wake velocity profiles at the hub height under ABL inlet with  $U_0 \approx 11.6$  m/s and incoming  $TI_{x,hub} \approx 7.1$  % within the near-wake region (Case 3).

The top-hat profile from the LES result around the blade mid-span to the wake centerline occurred earlier than in Case 2, observably from  $x/D=2.5$ . As in Case 2, the proposed function also overestimated the wake velocity at  $x/D=3$ , with a salient deviation within a rotor swept area. However, the resulting analytical prediction could still reasonably produce the DG velocity distribution at that distance.

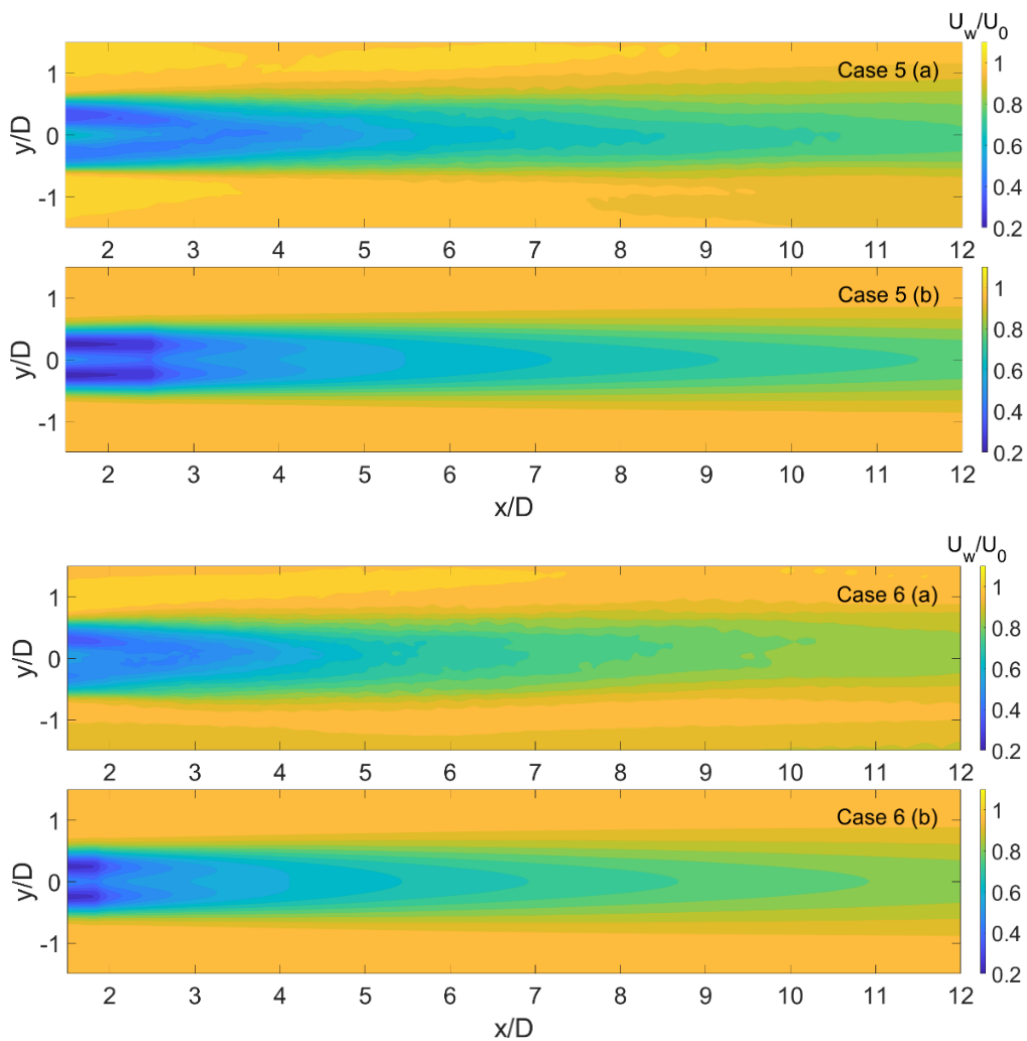
In general, the proposed expansion function could give a rough yet reasonable representation of the wake profile expansion and its recovery within the near-wake region of the evaluated Cases 1-3. Salient velocity deficits were noticed around the centerline due to the nacelle blockage effect, observably up to  $x/D=1.0$ . Afterward, the bimodal distribution formed, which justifies the DG-based approach's feasibility in representing the wake velocity distribution within the near-wake region.

## 5.4.2 The full-wake region

This section highlights the wake characteristics within the full-wake region of Cases 4-7, represented by the hub-height wake velocity distribution and its recovery under different turbine operating and inflow conditions.

### 5.4.2.1 Contour of streamwise wake velocity

Fig. 5.5 shows the hub-height streamwise wake velocity contours within the full-wake region from Cases 5-7. Meanwhile, Case 4 was excluded from contour mapping due to the limitation of measurement data points, which could affect the contour mapping accuracy. By referring to the velocity colorbar, the DG wake profile in Case 5 can be observed from the LES result and its analytical prediction until  $x/D \approx 2.5$ . Afterward, the wake velocity gradually recovered and transformed into the SG profile at further downstream distances. It was found that the maximum velocity deficit was located around the blade mid-span position.



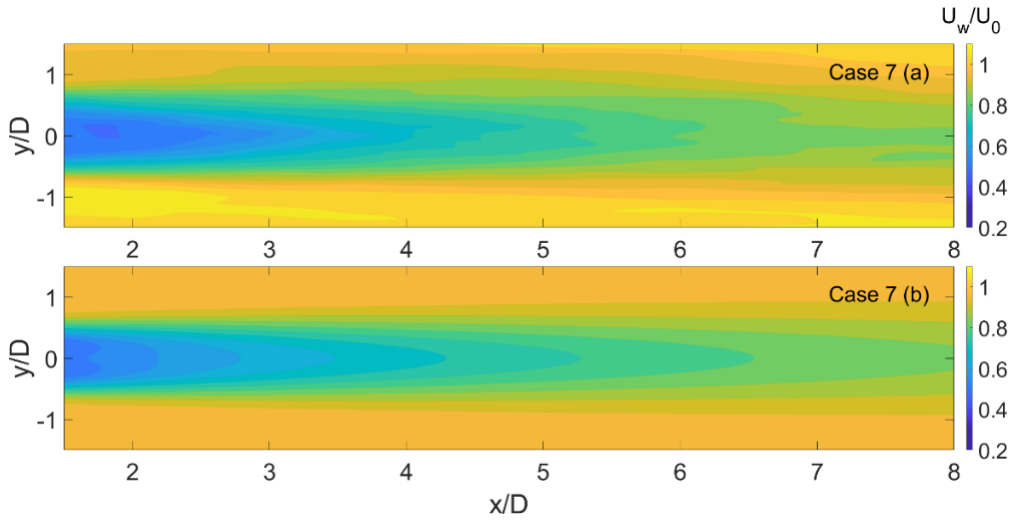


**Figure 5.5.** Contours of streamwise wake velocity on the horizontal plane at the hub height within the full-wake region. (a) LESs (b) DG analytical wake model with the proposed expansion function.

The same wake transformation behavior was found in Case 6 but with faster recovery. Velocity deficit around the blade mid-span was observed to reduce gradually after  $x/D \approx 2$ . Meanwhile, a prominent velocity deficit could not be found in Case 7, either from the LES result or its analytical prediction. Thus, causing the wake velocity around the blade mid-span to the centerline was less varying. This behavior might indicate that the DG profile only took place at a distance just behind the turbine before it eventually merged into the SG profile and quickly recovered at the farther downstream positions.

The discussion above gives a qualitative judgment regarding the consistency between the LES results and their analytical predictions using the DG model with the proposed expansion function for the streamwise velocity field prediction within the full-wake region. Relatively low incoming  $TI_{x,hub}$  as in Case 5, resulted in a slow wake recovery. Meanwhile, the wake recovered faster with a relatively moderate incoming  $TI_{x,hub}$ , as in Case 6. The high incoming  $TI_{x,hub}$  in Case 7 caused the wake to recover faster than the previous Cases 5-6. These results reconfirmed the previous investigations using experimental, theoretical, and numerical studies, which showed that the HAWT wake recovers more rapidly under higher turbulence inflow [5], [6], [28].

### 5.4.2.2 The wake width and centerline velocity deficit

In the present study, the proposed expansion function is compared against the existing expansion function for the DG wake model [26]. The existing function is expressed as follows:

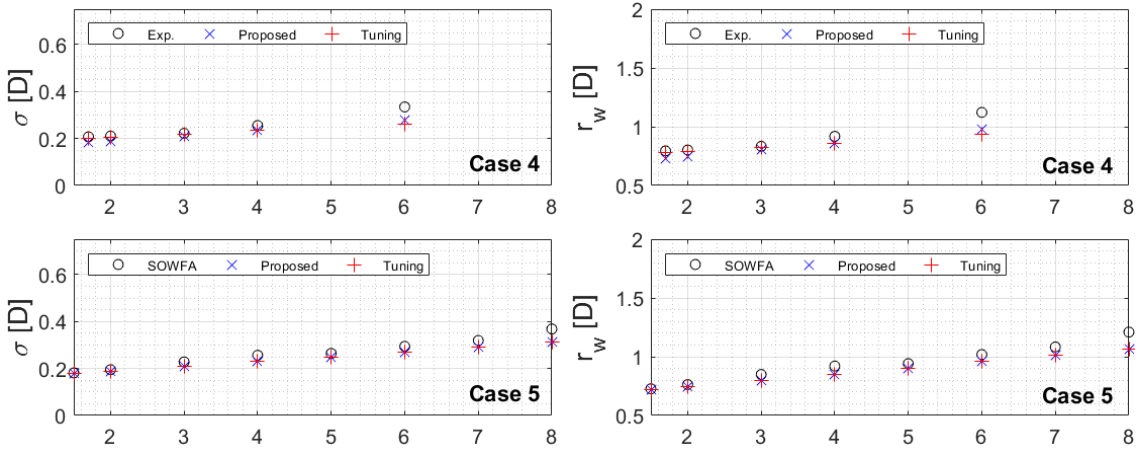
$$\sigma = k^* (x - x_1) + \sigma_{w1} . \quad (5.17)$$

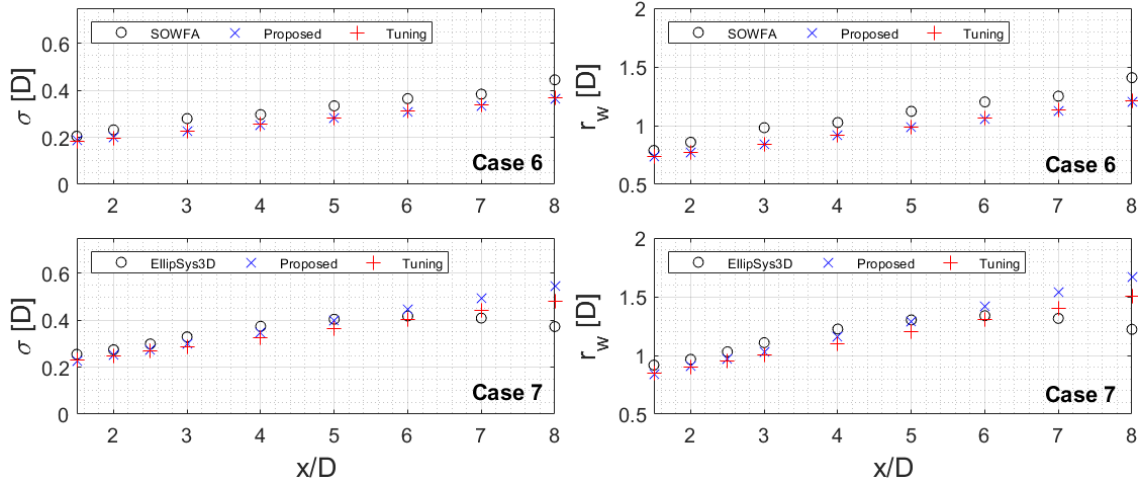
The parameter  $k^*$ , which controls the wake expansion rate, is tuned by case. Here, *fminsearchcon* MATLAB function [42] was employed to find the  $k^*$  values that give the best fit with the benchmark datasets. After applying the DG model described in Table 5.1, the tuned  $k^*$  values that best fit the benchmark data sets are shown in Table 5.3.

**Table 5.3.** Far-wake onset and tuned  $k^*$  parameter for Cases 4-7.

Case	Input parameters		
	Turbine	$x_1/D$ (Eq. 5)	$k^*$ (Tuning)
4	G1	3.98	0.0108
5	INNWind 10 MW	4.41	0.0154
6		3.22	0.0283
7	NREL 5 MW	1.89	0.0387

The estimated far-wake onset values ( $x_1/D$ ) for Cases 4-7 in Table 5.3 were also used by the proposed expansion function. The comparison of wake expansion between the proposed and tuned expansion functions against the benchmark data is shown in Fig. 5.6.

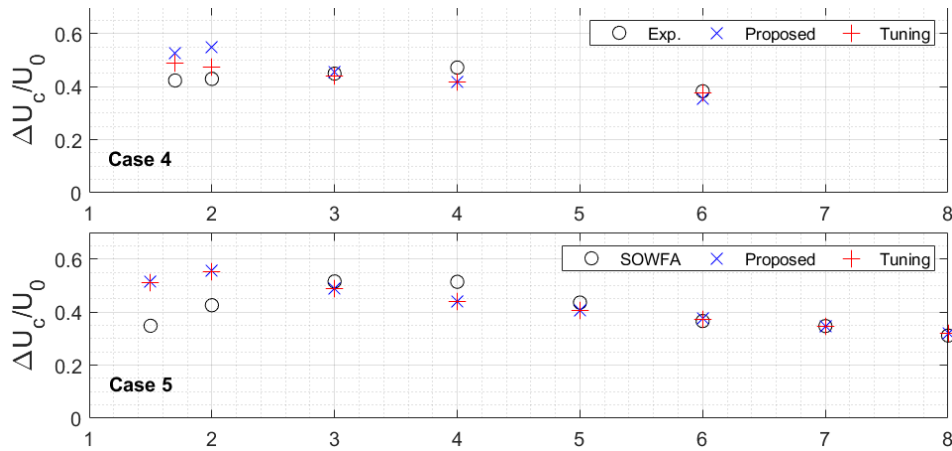




**Figure 5. 6.** Standard deviation of DG velocity deficit profile centered at the local Gaussian minima ( $\sigma$ ) and wake radius ( $r_w$ ) as functions of the normalized downstream distance ( $x/D$ ).

In general, the proposed expansion function could reasonably estimate the wake expansion with relatively small residuals against the benchmark data. The proposed and tuned function predictions for  $\sigma$  and  $r_w$  in Cases 4-6 were nearly identical. However, noticeable differences were found in Case 7, where the wake radius resulting from both expansion functions deviated from the LES result, mainly at  $x/D > 6$ . The  $\sigma$  and  $r_w$  from the LES result were observed to shrink, resulting in a curved expansion. This occurrence may be related to the wake contraction, which is not accounted for in the present DG wake model.

The wake expansion is related to the wake recovery. Thus, the expansion function of the DG wake model has a significant influence on the accuracy of the wake recovery prediction. Fig. 5.7 compares the normalized velocity deficit at the centerline  $\Delta U_c/U_0$  predicted by the DG analytical model using both the proposed and tuned expansion functions.



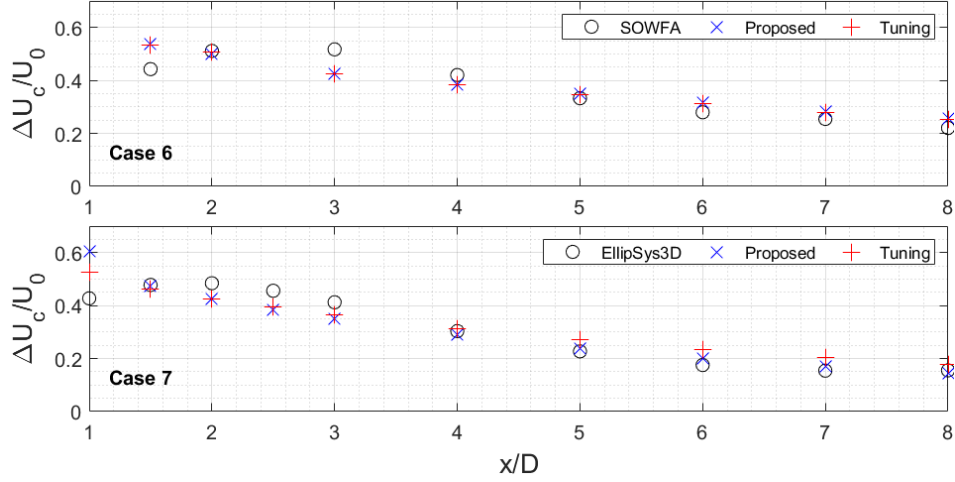


**Figure 5. 7.** The normalized velocity deficit at the centerline  $\Delta U_c/U_{hub}$  for Cases 4-7.

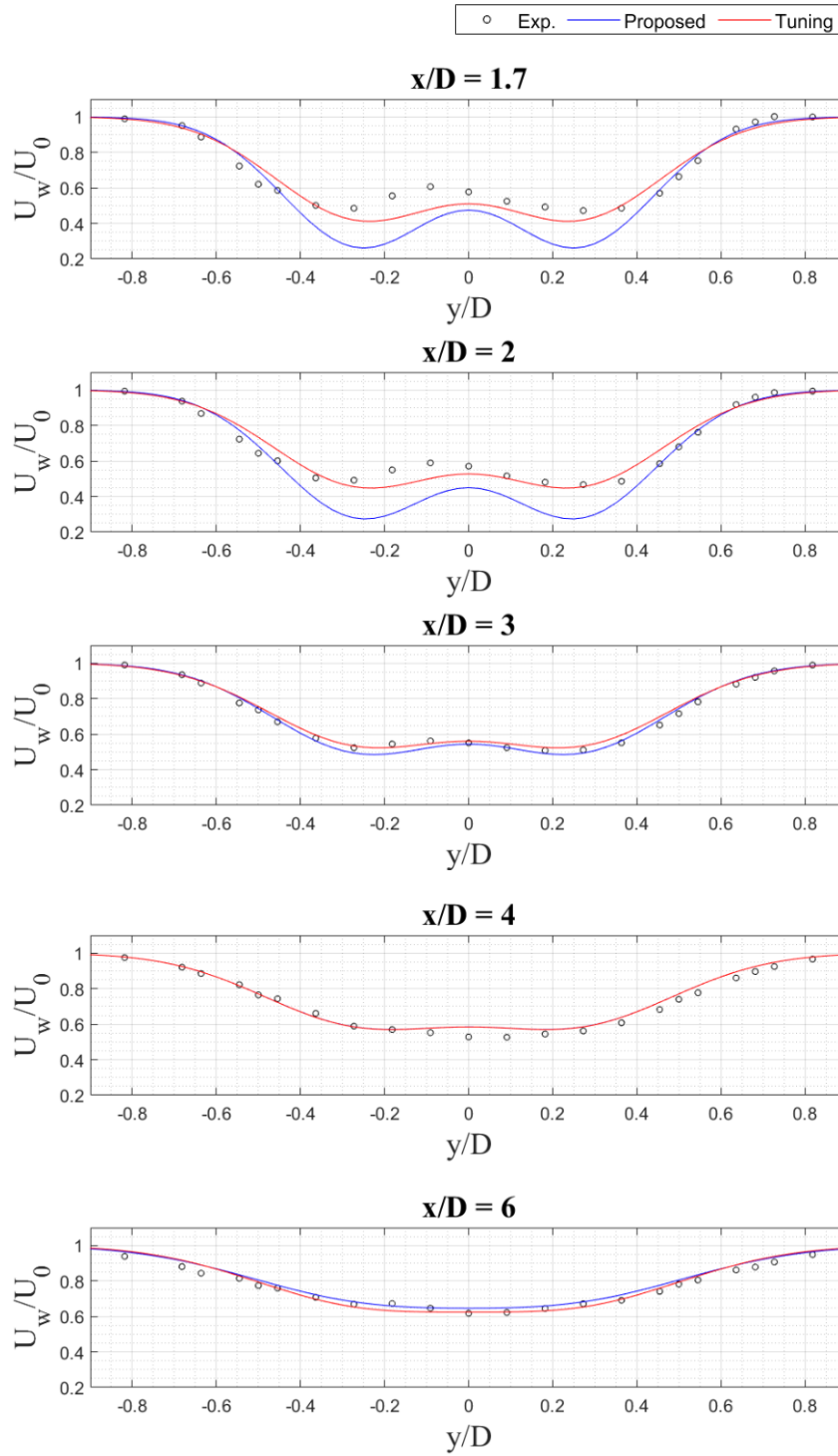
The predictions of  $\Delta U_c/U_0$  from both the expansion functions are in good agreement with most of the benchmark datasets. The centerline velocity deficit  $\Delta U_c/U_0$  gradually diminished as the downstream distance increased, representing the wake recovery at the selected distances. Sampled at the downstream position within the far-wake region where the flow is already stable ( $x/D=8$ ), it was found that the centerline velocity deficit  $\Delta U_c/U_{hub}$  for the Cases 4-7 with the respective incoming  $TI_{x,hub}$  of 6.25, 5.1, 8.5, and 16% were about 0.3, 0.325, 0.225, and 0.15, respectively. As expected, Case 7 with the highest incoming  $TI_{x,hub}$  had the lowest velocity deficit at the distance of interest. In contrast, Case 5, with the smallest incoming  $TI_{x,hub}$ , gave the maximum  $\Delta U_c/U_{hub}$  among the other evaluated Cases. These results confirm the strong dependency of the wake recovery rate on the incoming turbulence intensity.

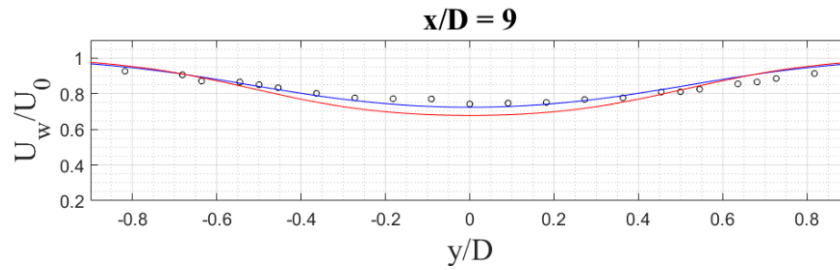
From the evaluated Cases, the proposed expansion function could give comparable performance against the tuning results. For Cases 5-6, both the expansion functions provided almost identical results at all the selected downstream distances. The highest residuals of  $\Delta U_c/U_{hub}$  between the expansion functions and the benchmark data were observed up to  $x/D=2$  for most of the evaluated Cases. Afterward, the analytical model's accuracy improved for all Cases 4-7.

### 5.4.2.3 Streamwise wake velocity

The proposed function's performance within the full-wake region was evaluated using four benchmark datasets of streamwise wake velocity profiles at the hub height in the lateral direction resulting from the wind tunnel measurements (Case 4) and the LESs (Cases 5-7). In addition, the best-fit results from the tuned expansion function were also included for comparison. The evaluation was specifically intended to examine the performance of the proposed function, where

its similarity with the fitting results could also represent its reliability. For Case 4, the measurement results at the selected downstream distances and their analytical predictions are shown in Fig. 5.8.

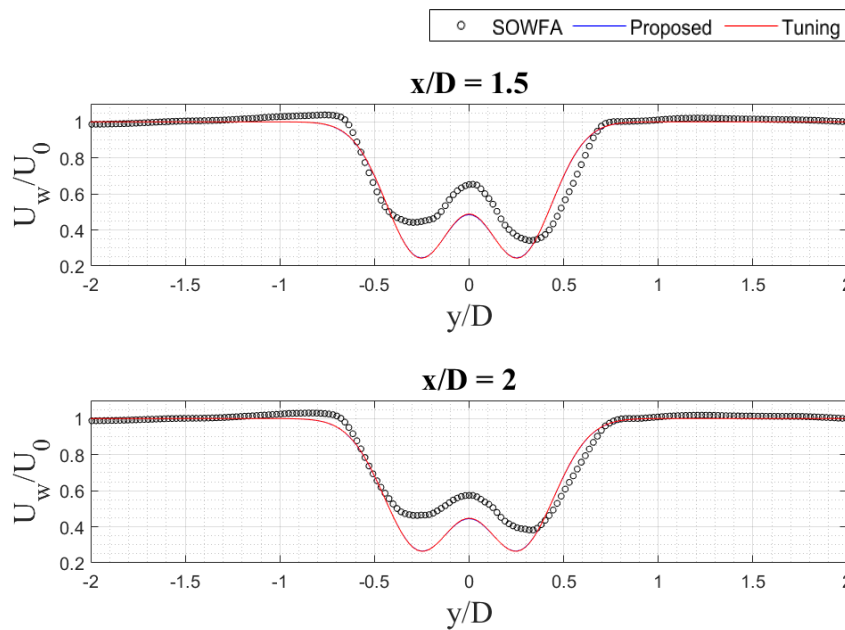


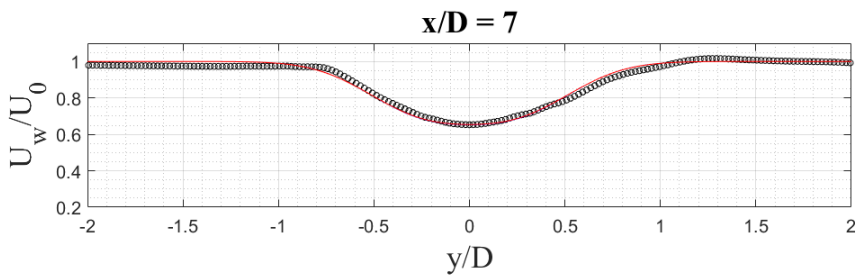
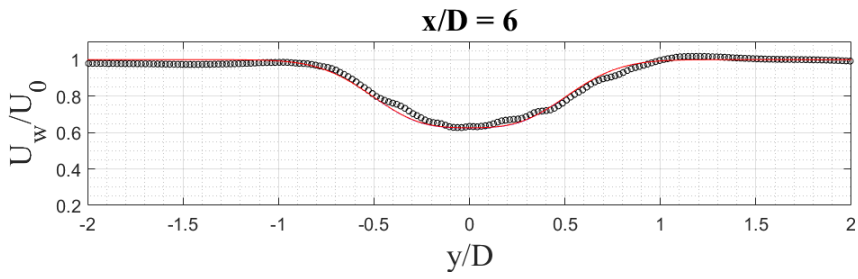
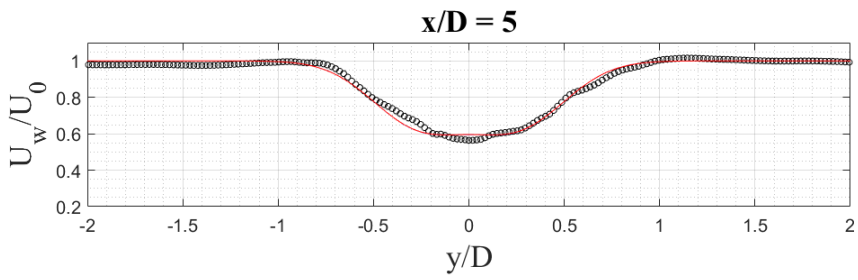
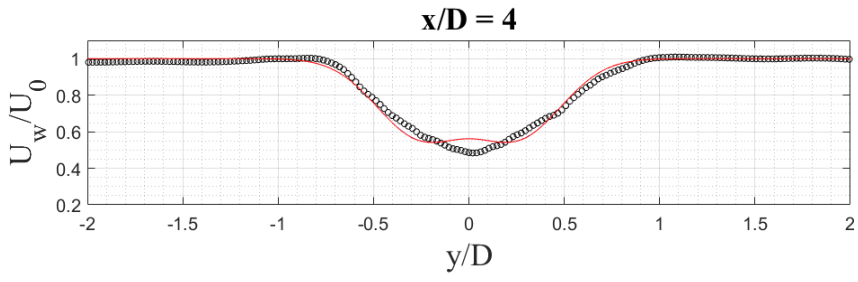
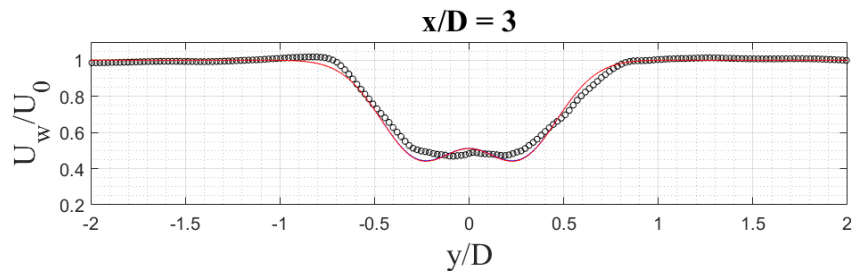


**Figure 5. 8.** Wake velocity profiles at the hub height in the lateral direction behind a G1 model turbine within the full-wake region (Case 4).

Salient residuals of the proposed function’s prediction against the measurement data were observed at the downstream distances of  $x/D=1.7$  and 2, notably around the blade mid-span. Meanwhile, the tuned function better estimated the wake profiles at the same locations. At  $x/D=3$ , the accuracy of the proposed function significantly improved, which was confirmed by its good agreement with the tuning result and the reference data. In addition, the DG distribution can still be observed clearly at  $x/D=3$ . At further distances of  $x/D=4$  and 6, the wake predictions from both the expansion functions were almost identical and tended to form the top-hat shape around the blade mid-span to the centerline. Nevertheless, their accuracies were still relatively high, around 96%, referring to the measurement data. At  $x/D=9$ , both expansion functions fully transformed into the SG shape, and the proposed function outperformed the tuning result.

The LES results for Case 5 and their analytical predictions are shown in Fig 5.9. The wake expansion predictions from the proposed and tuned functions at all the selected distances were quantitatively similar.





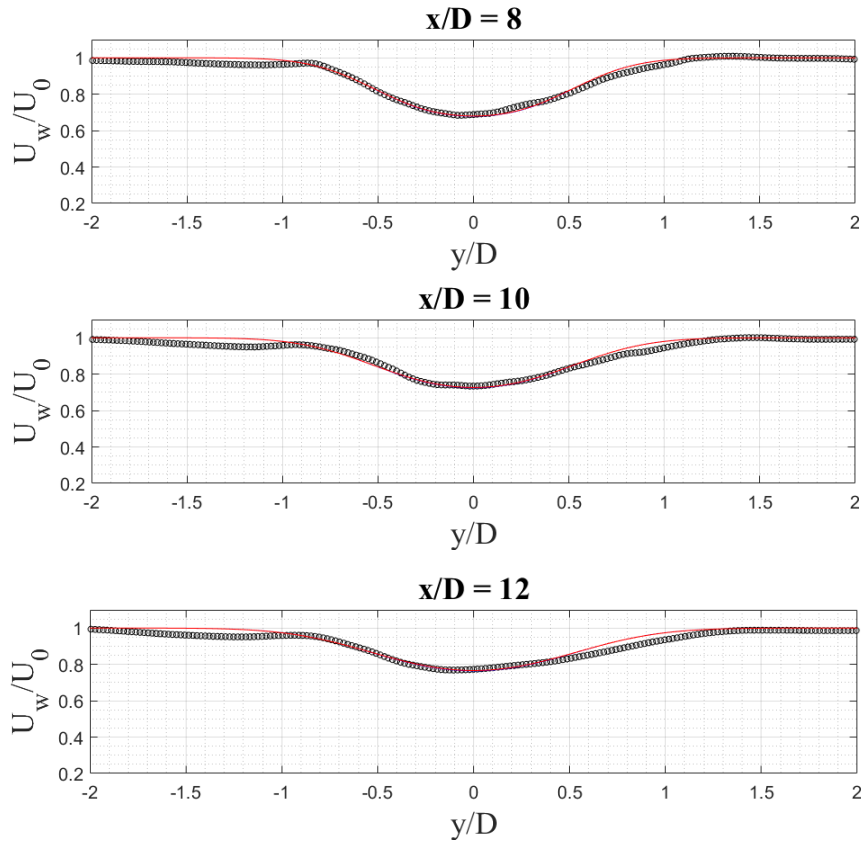
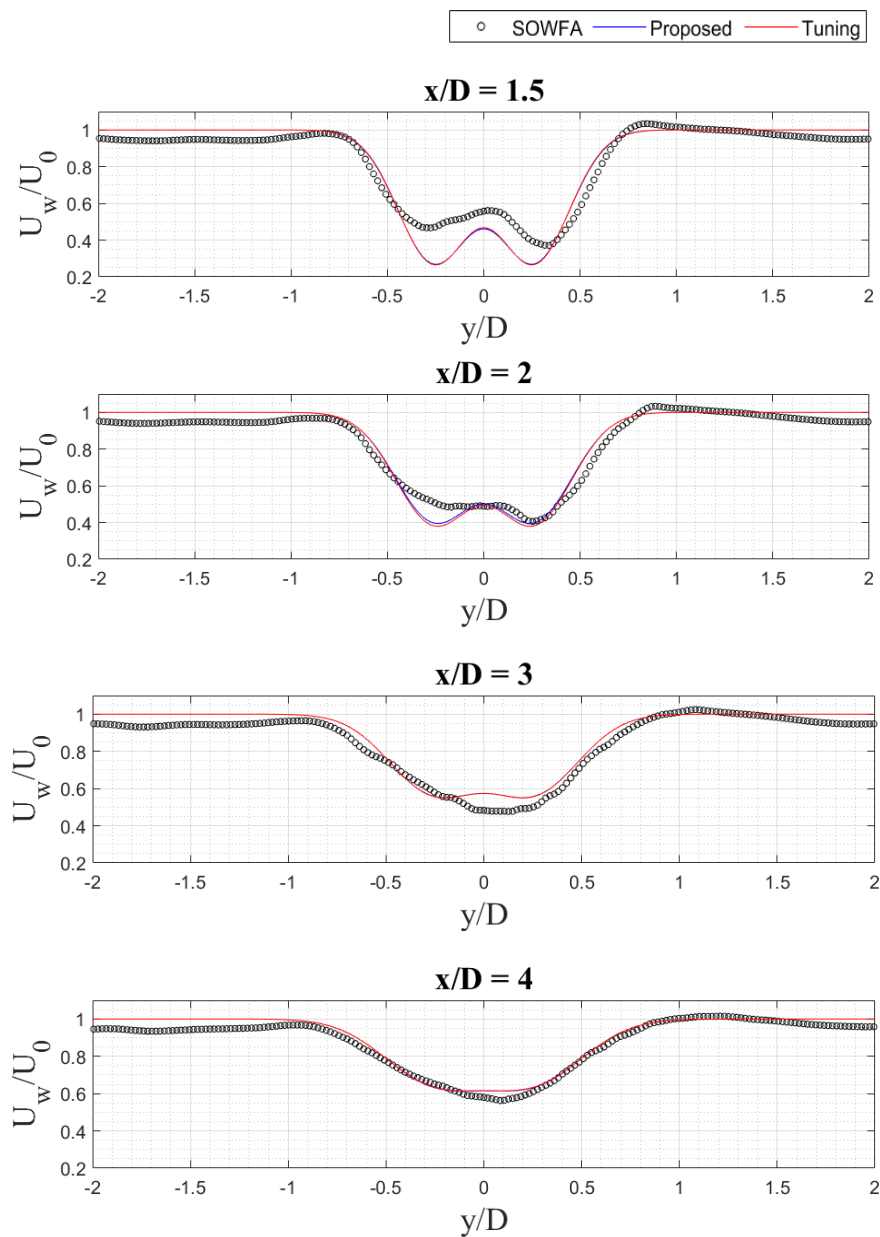


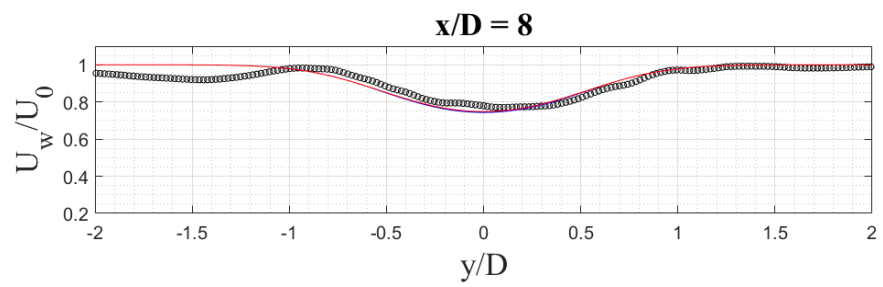
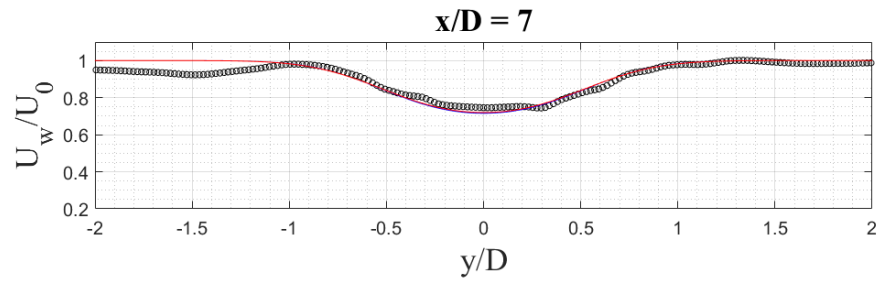
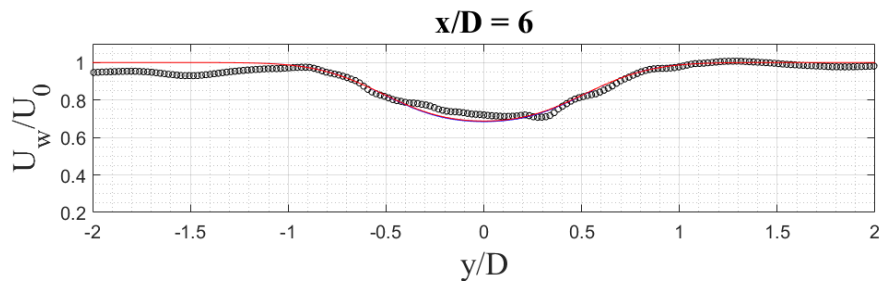
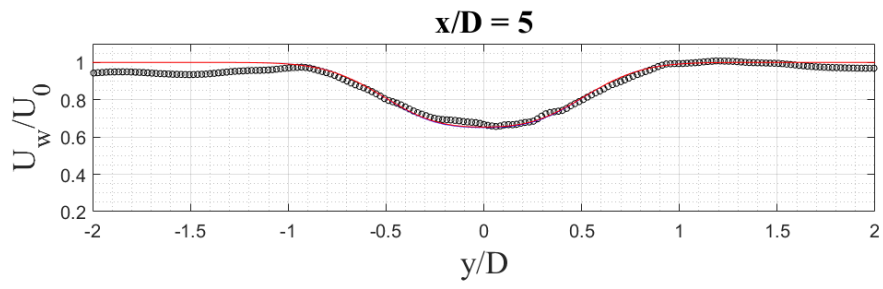
**Figure 5. 9.** Wake velocity profiles at the hub height in the lateral direction behind an INNWIND 10 MW reference turbine within the full-wake region (Case 5).

The DG distributions were observed clearly from the LES and analytical results at the downstream distances of  $x/D=1.5$  and 2. However, noticeable differences were found mainly within the blade mid-span area, where the DG model predictions from both the expansion functions underestimated the LES results. Moreover, the LES results produced asymmetric distributions, where the wake profiles in the negative lateral direction recovered faster than in the opposite direction. These appearances could not be reproduced by the analytical model due to the axisymmetric approach being used.

Meanwhile, better wake profile prediction and recovery were obtained as the downstream distance increased. At  $x/D=3$ , a relatively small discrepancy between the LES result and its analytical predictions were still observed within the blade mid-span area but were less significant. The LES result formed a top-hat profile within this area before eventually transforming into an SG profile at  $x/D=4$ . In general, the accuracies of both the expansion functions for the wake profile predictions were further improved at the farther downstream distances. At  $x/D \geq 6$ , the estimated velocity profiles have fully transformed into the SG distribution, causing accuracy improvement in velocity deficit estimations at the centerline.

The LES results and their analytical predictions in Case 6 are shown in Fig. 5.10. At all the selected distances, the wake profiles from the proposed function almost matched perfectly with the tuning results. However, it was observed that both expansion function predictions underestimated the LES results at  $x/D=1.5$  and 2. The major difference was observed between the blade mid-span and the centerline position, particularly in the negative lateral direction where the LES results showed faster wake recovery, thus creating asymmetric wake profiles. At  $x/D=3$ , the LES result tended to form a top-hat profile around the wake center, while the analytical predictions remained in the DG shape profile. At the distance of  $x/D=4$ , less residuals were observed around the same position.





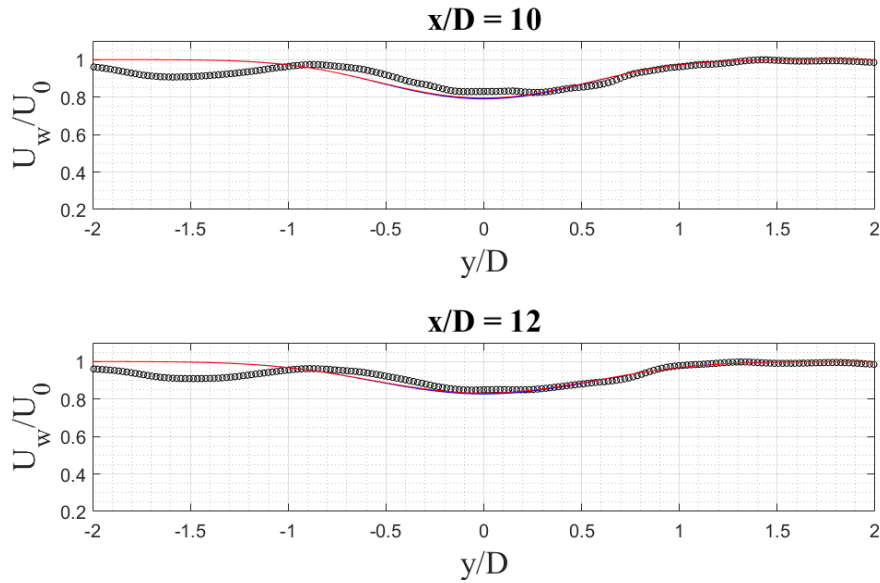


**Figure 5.10.** Wake velocity profiles at the hub height in the lateral direction behind an INNWIND 10 MW reference turbine within the full-wake region (Case 6).

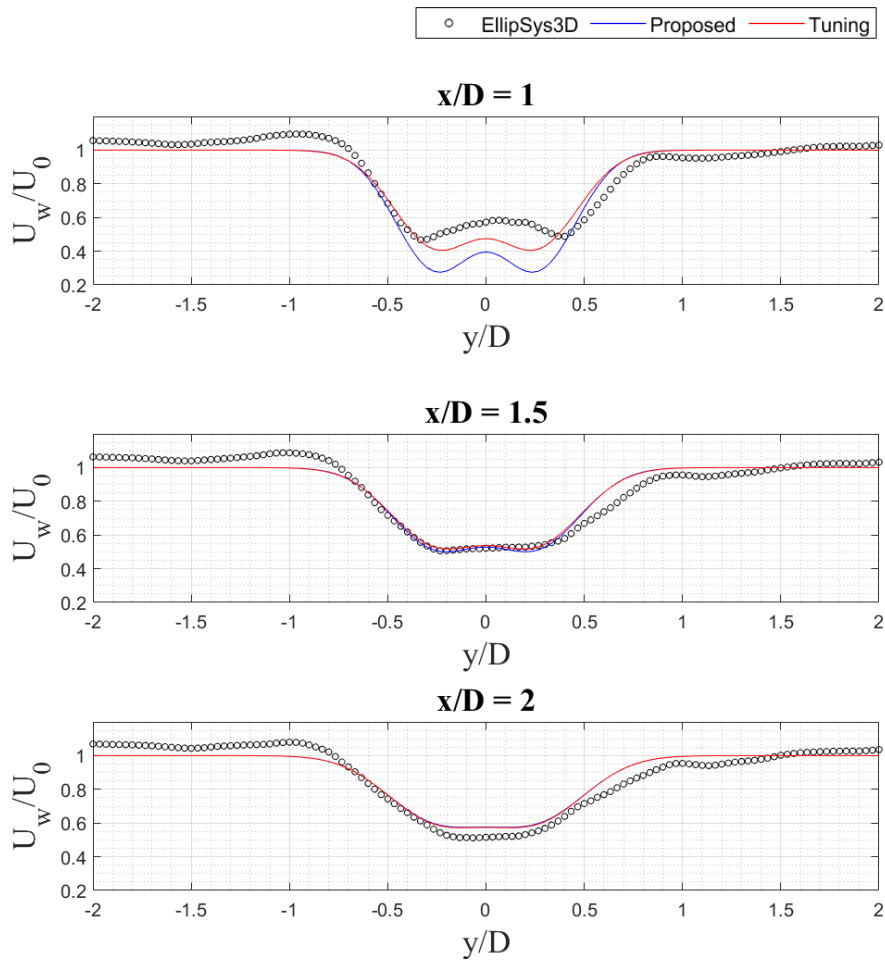
The wake profiles predicted by the DG model eventually transformed into an SG shape starting from  $x/D=5$ , thus reducing the residuals against the LES results. Within  $6 \leq x/D \leq 12$ , the wake center gradually shifted around  $y=0$  toward the positive lateral direction. This occurrence was strongly related to the wake meandering, which made random oscillations with respect to the wake trajectory. Distinct velocity fluctuations were also observed, mainly at the lateral directions of  $y/D \leq -1$ . However, the DG model with the proposed expansion function was still relatively good in predicting the average behavior of the wake profile, especially within the far-wake region.

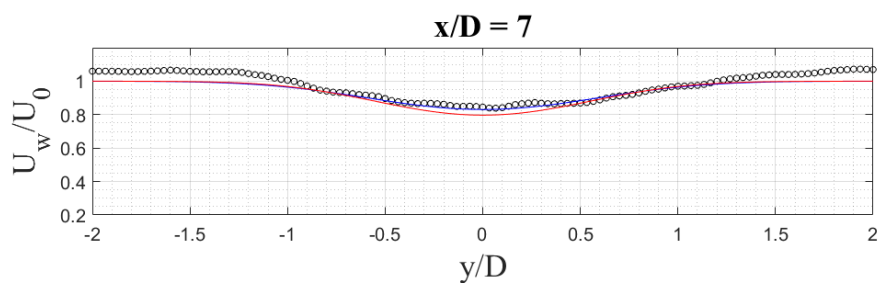
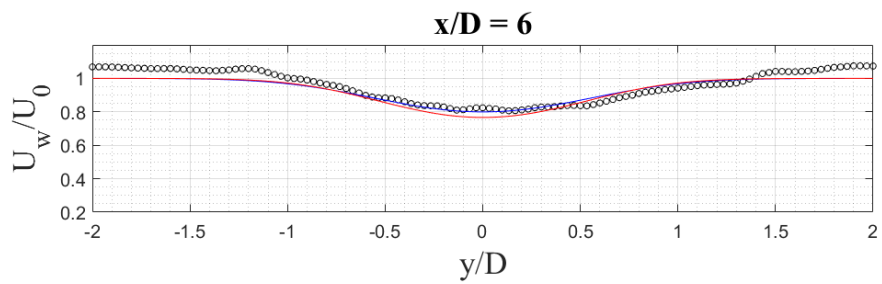
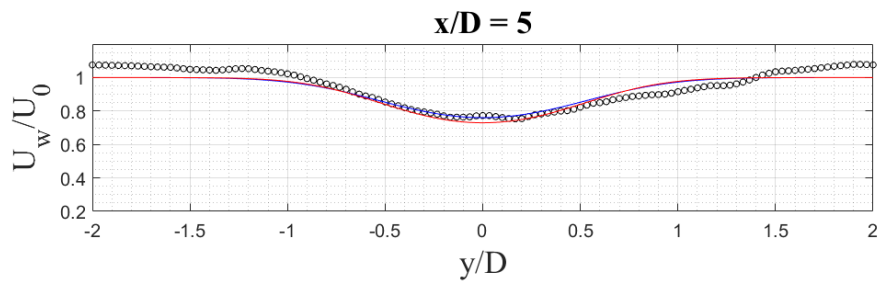
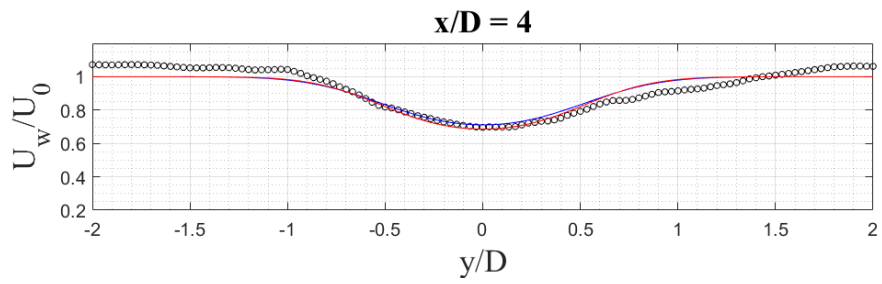
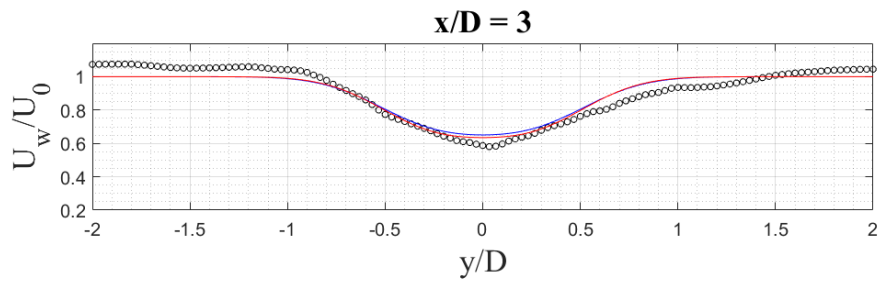
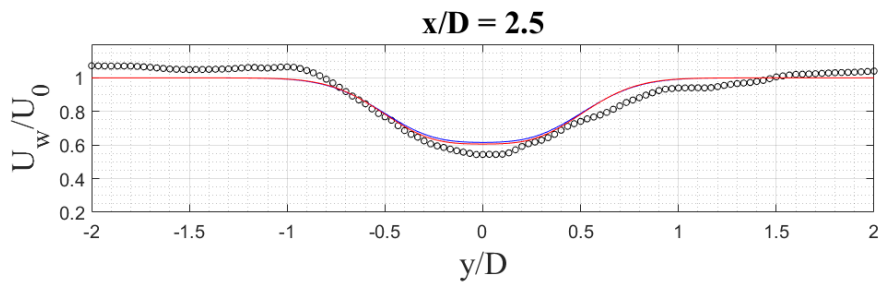
The LES results for Case 7 and their analytical predictions are compared in Fig. 5.11. At the downstream distance of  $x/D=1$ , the DG model, particularly by using the proposed function, underestimated the velocity profile produced by the LES around the blade mid-span to the centerline position. In addition, the wake fluctuation within  $-1.2 \leq y/D \leq -0.7$  from the LES result increased the analytical model residuals against the LES data. At the farther distance of  $x/D=1.5$ , the prediction accuracy from the analytical model improved, where both the expansion functions accurately predicted the wake profile around the centerline. However, the velocity fluctuation still occurred in the LES result with lower intensity.

At the downstream distance of  $x/D=2$ , the wake profiles predicted by both expansion functions almost coincide. The profiles formed a top-hat shape around the blade mid-span to the centerline position and slightly overestimated the LES result. The same behavior was also observed at  $x/D=2.5$  but with lesser residuals. In addition, an obvious transition of the wake profile from top-hat to fully SG shape was observed in the LES result, which indicated a faster wake recovery,

particularly compared with the other evaluated Cases. At the farther downstream distances, discrepancies between the LES results and their analytical predictions around the centerline became narrower, thus increasing the analytical model accuracy at the remaining selected distances.

The wake profiles predicted by the DG model with both expansion functions have fully transformed into SG shape at  $x/D \geq 3$ , yielding better fitness with the LES data. By looking in more detail within  $5 \leq x/D \leq 8$ , the proposed function outperformed the tuning results by giving better accuracy of the wake recovery predictions within the rotor swept area. In general, the ability of the analytical model to predict the general characteristics of the wake velocity profile and its recovery for the evaluated Cases 5-7 is relatively accurate, particularly when considering the huge distinction of computational resources between computational (LES) and analytical approaches.





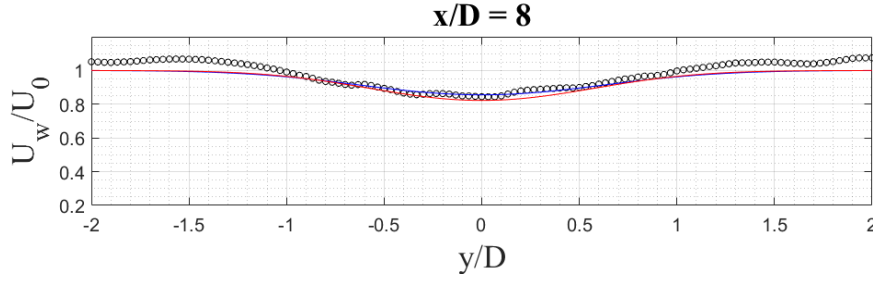


**Figure 5. 11.** Wake velocity profiles at the hub height in the lateral direction behind an NREL 5 MW reference turbine within the full-wake region (Case 7).

### 5.4.3 Statistical evaluations

In this section, statistical measures are used to quantify the effectiveness of the proposed expansion function for the evaluated Cases. The normalized mean square error (NRMSE) was used to measure the residuals from the evaluated expansion functions against the benchmark datasets. Meanwhile, the  $R$  linear correlation coefficient was used to measure a linear dependence between the benchmark datasets and their analytical predictions. It must be stated that these statistical measures only provide a general correlation between the model and the benchmark data from the sampled points. Those statistical measures are formulated as follows:

$$\text{NRMSE} = \sqrt{\frac{\sum_{i=1}^N (E_i - B_i)^2}{\sum_{i=1}^N B_i^2}}, \quad (5.18)$$

$$R = \frac{\overline{(B_i - \bar{B}) \times (E_i - \bar{E})}}{\sigma_B \times \sigma_E}, \quad (5.19)$$

where  $E$  denotes the analytical estimation either using the proposed or tuned function,  $B$  denotes the benchmark data, subscript  $i$  denotes the  $i^{\text{th}}$  point from the total  $N$  points, and the overbar ( $\bar{\quad}$ ) means an average from all  $N$  points. Meanwhile,  $\sigma_B$  and  $\sigma_E$  refer to the standard deviation from the analytical and benchmark datasets, respectively.

The NRMSE and  $R$ , as formulated in Eqs. 5.18 and 5.19, were measured at each selected downstream distance. There were 22 points from  $-0.82 \leq y/D \leq 0.82$  for Case 4, 201 points from  $-2.12 \leq y/D \leq 2.12$  for Cases 5-6, and 121 points from  $-2. \leq y/D \leq 2$  for Case 7, measured at each selected distance for NRMSE and  $R$  analyses. A perfect model would result in NRMSE and  $R$  values of 0 and 1, respectively. It is worth noting that the total number of points ( $N$ ) used in each Case for these statistical evaluations varied according to the data availability. The comparison of

NRMSE and  $R$  between the proposed and tuned expansion functions for the evaluated Cases 4-7 is shown in Fig. 5.12.

For Case 4, NRMSEs of the DG model with the proposed function were higher than the tuning results at  $x/D=1.7$  and 2. These errors occurred due to a significant underestimation of the wake velocity, particularly around the blade mid-span area. In contrast, the  $R$  coefficients for the proposed function were highly correlated and remained high at the evaluated distances. This condition happened due to the high linearity between the analytical and measurement results. Meanwhile, within the evaluated distances of  $3 \leq x/D \leq 9$ , the accuracy of the proposed function significantly improved where the average  $\text{NRMSE} \approx 0.03$ . The same trend applied for the tuned function, except at the distance of  $x/D=9$  with an NRMSE of about 0.06 higher than the proposed function's NRMSE.

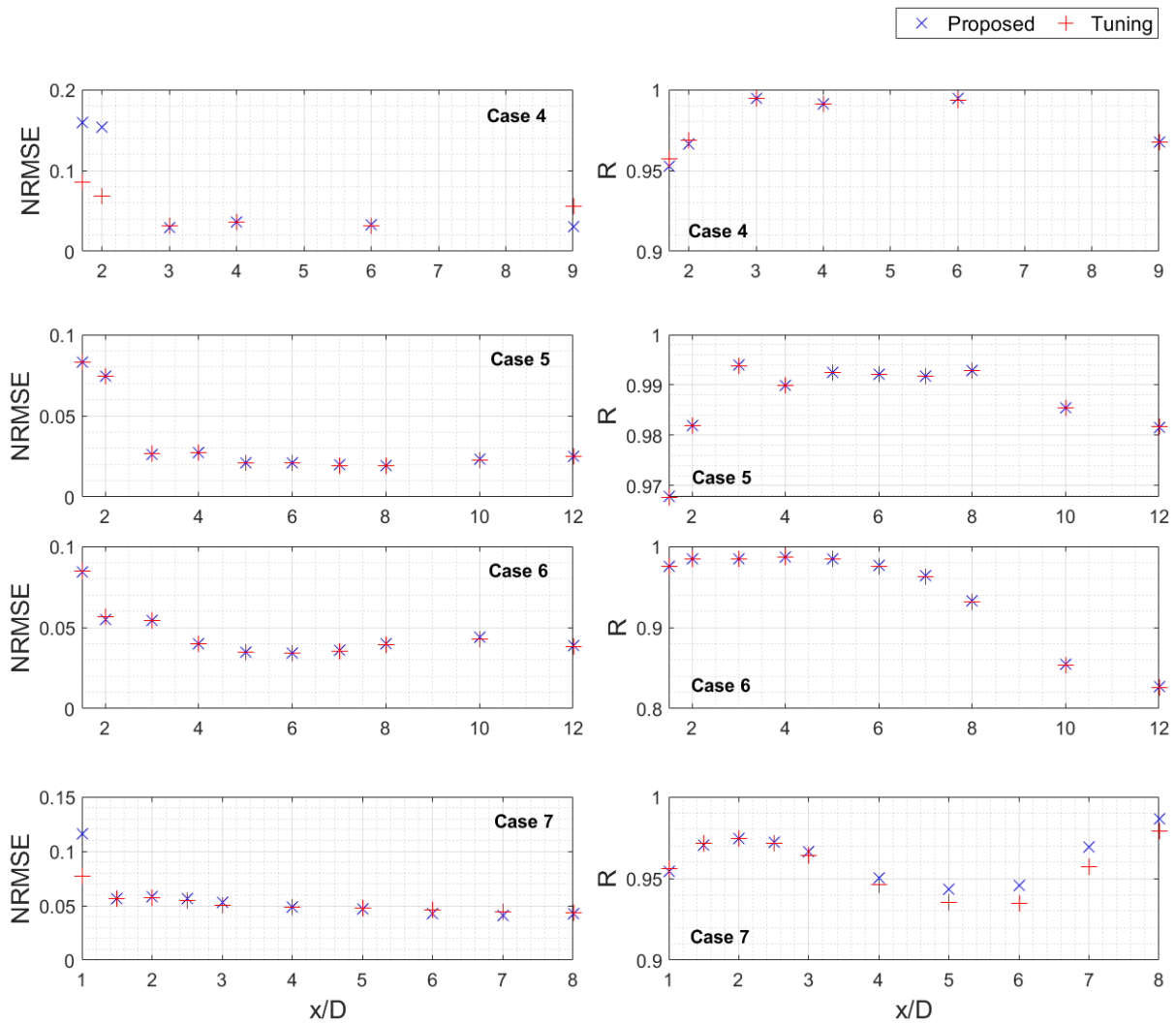


**Figure 5. 12.** Comparison of the normalized root mean square error NRMSE and the linear correlation coefficient  $R$  between the proposed and the tuned expansion functions.

In Case 5, the results of NRMSE and  $R$  obtained from both expansion functions are in close agreement for all distances considered. Prominent NRMSEs from both functions were observed within the distances of  $x/D \leq 2$  and significantly reduced to less than 0.03 at the remaining selected distances. Meanwhile, the  $R$  coefficients of wake shape distribution between expansion function predictions and the LES results show high linearity at all selected distances.

In Case 6, no significant discrepancies between the expansion functions were observed in NRMSEs and  $R$  results. The highest NRMSEs from both the functions against the benchmark datasets were approximately 0.085 at the distance of  $x/D=1.5$ , with relatively high  $R$  coefficients of about 0.98. At the distances of  $x/D=2$  and 3, the NRMSEs from both functions were  $\approx 0.055$  and reduced further to about 0.04 at the remaining selected distances. Besides, the  $R$  correlations from both the expansion functions within  $2 \leq x/D \leq 5$  were approximately 0.98 and substantially decreased to about 0.82 at  $x/D=12$ . This steep reduction was caused by the fluctuation of the wake profiles and shifting of the wake center in the LES results.

In Case 7, the highest residual from both expansion functions was observed at  $x/D=1$ , where the proposed function's NRMSE was about 0.035 higher than the tuning result. Their NRMSEs at the remaining selected distances almost coincide within the range 0.045~0.055. Meanwhile, the  $R$  coefficients resulting from both expansion functions were relatively high at all the selected distances. The amplitude of  $R$  coefficient fluctuation was found to increase with the downstream distance. It should be noted that the  $R$  coefficients obtained from the proposed function were higher than the tuning results at  $x/D \geq 5$ . This was consistent with the NRMSEs within the same distances where the proposed function predictions for the wake profile were more accurate than the tuned function.

#### 5.4.4 Comparison of wind power potential

In a wind farm, energy potential from the wake velocity behind the upstream turbines is extracted by the respective downstream turbines for power generation. By referring to the wind energy theory, wind power varies as the cube of the wind velocity. Therefore, the validity of the power prediction of the downstream turbine is strongly determined by the prediction accuracy of the upstream turbine wake. The wind power potential within the wake region  $P_w$  is calculated using the following formula:

$$P_w = \frac{1}{2} \rho A_0 U_{p,w}^3, \quad (5.20)$$

where  $\rho$  is the air density and  $A_0$  denotes the rotor swept area. In this study, the streamwise wake velocity at the hub height spanned in the lateral direction within the rotor swept area (-

$0.5 \leq y/D \leq 0.5$ ) was averaged to represent the potential wake velocity  $U_{p,w}$ , thus the wind power potential  $P_w$  at each evaluated downstream distance can be estimated using Eq. 5.20. The same method was applied to calculate the reference wind power potential  $P_{ref,w}$  resulting from the reference potential wake velocity  $U_{ref,p,w}$ .

The practical region<sup>38</sup>, located within the downstream distances of  $2.4 \leq x/D \leq 11$ , covers the range of actual HAWTs micro-siting in both onshore and offshore wind farms. Thus, it was considered in this study as the region of interest to be evaluated. The normalized wind power potential  $P_w/P_{ref,w}$  from the benchmark datasets and the DG model using both expansion functions within the downstream distances of  $2.4 \leq x/D \leq 12$  were calculated and compared in Fig. 5.13.

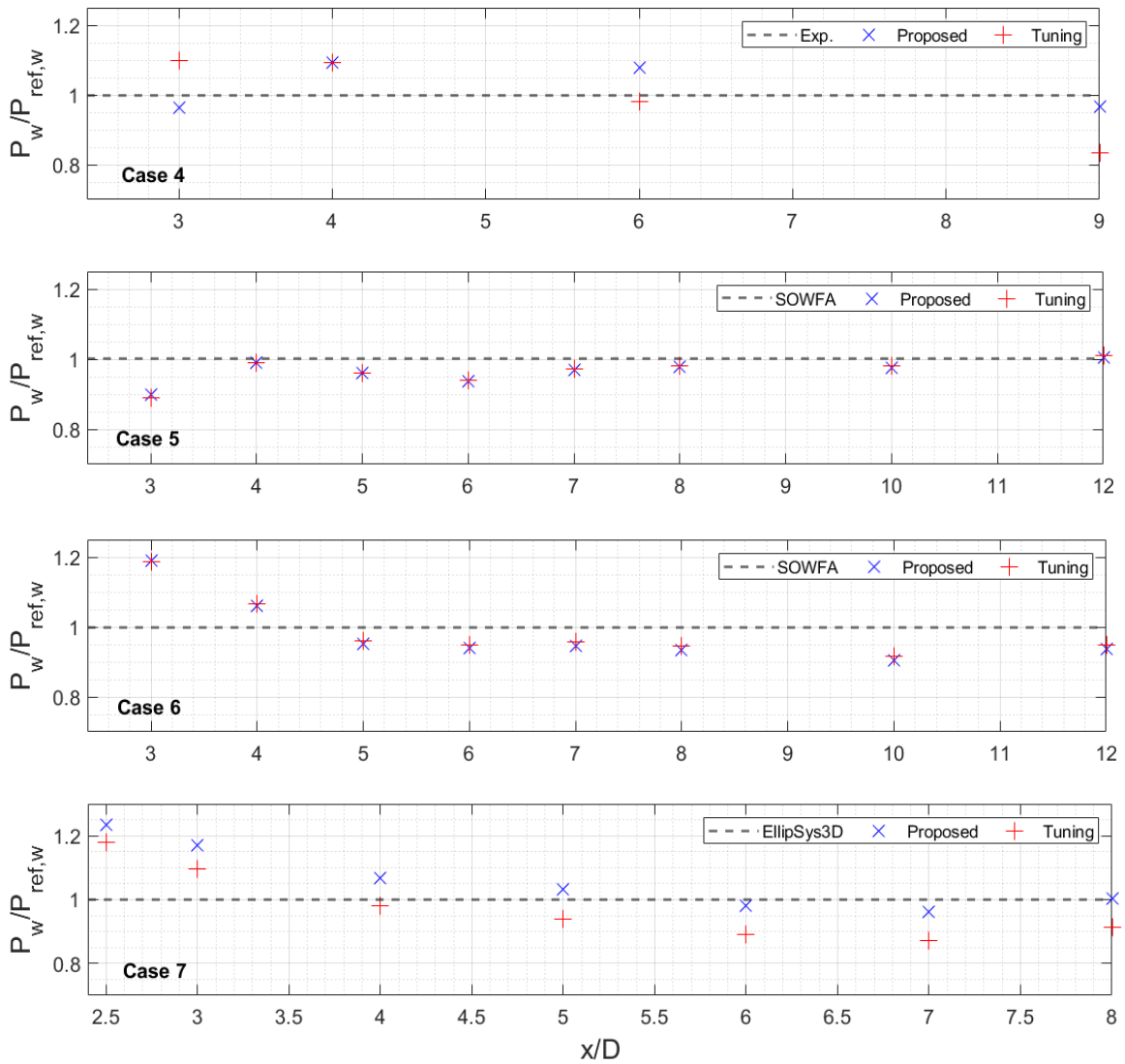


**Figure 5.13.** Comparison of the normalized wind power potential  $P_w/P_{ref,w}$  between the analytical predictions and their benchmark datasets.

In Case 4, four downstream distances ranging from  $3 \leq x/D \leq 9$  were selected. Compared to the tuned function, the proposed function provided a better prediction of wind power potentials at  $x/D=3$  and  $9$  with  $P_w/P_{ref,w}$  of about  $0.96$  and  $0.97$ , respectively. Meanwhile, the worst performance was found at  $x/D=4$ , where both expansion functions resulting almost the same  $P_w/P_{ref,w}$  of about  $1.09$ , which was approximately  $0.09$  higher than the reference value.

In Case 5, results from the proposed function were similar to the tuning results within all selected distances. At  $x/D=3$ , residuals of about  $0.11$  lower than the reference value were obtained from both expansion functions. As the downstream distance increased, the performance of both expansion functions improved with the residuals below  $0.04$  against the reference values. Meanwhile, the highest accuracies from both expansion functions were found at  $x/D=12$ , where their predictions were almost identical to the reference data.

For Case 6, predictions of  $P_w/P_{ref,w}$  by the proposed function were also in good agreement with the tuning results. The highest residuals from both expansion functions were about  $0.19$  higher than the reference value at  $x/D=3$  and significantly reduced to approximately  $0.07$  at  $x/D=4$ . It was also observed that the predictive ability improved at the distances of interest within the far-wake region. The accuracy of both expansion functions at the distances of  $x/D \geq 5$  was almost constant. The average  $P_w/P_{ref,w}$  was approximately  $0.94$ , except at  $x/D=10$ , where the residual was about  $0.09$  lower than the reference line.

In Case 7, the proposed function yielded normalized power differences  $\Delta P_w/P_{ref,w}$  of about  $0.057 \sim 0.096$  higher than the tuning results. Within the selected distances of  $x/D \leq 4$ , the tuned function had better accuracies than the proposed function predictions. At the farther distances of  $x/D \geq 5$ , the proposed function predictions outperformed the tuning results with  $\Delta P_w/P_{ref,w}$  ranging about  $0.091 \sim 0.096$ . Meanwhile, the minimum  $\Delta P_w/P_{ref,w}$  against the benchmark data was about  $0.005$  or  $0.995$  of accuracy at  $x/D=8$ .

#### **5.4.5 The performance comparison of the evaluated Cases 4-7**

The result of mean values of NRMSE,  $R$  coefficient, and  $\Delta P_w/P_{ref,w}$  within the full-wake and practical regions are summarized in Tables 5.4 and 5.5, respectively. The bold values in Tables 5.4 and 5.5 show better performances.

**Table 5. 4.** The mean values of NRMSE,  $R$  coefficient, and  $\Delta P_w/P_{ref,w}$  within the full-wake region.

Case	$\overline{\text{NRMSE}}$		$\bar{R}$		$\overline{\Delta P_w/P_{ref,w}}$	
	Proposed	Tuning	Proposed	Tuning	Proposed	Tuning
4	0,074	<b>0,051</b>	0,978	<b>0,979</b>	0,201	<b>0,082</b>
5	0,034	0,034	0,987	0,987	0,122	0,122
6	0,046	0,046	0,947	0,947	0,118	<b>0,117</b>
7	0,056	<b>0,053</b>	<b>0,963</b>	0,959	0,145	<b>0,127</b>
Average 4-7	0,053	<b>0,046</b>	<b>0,969</b>	0,968	0,147	<b>0,112</b>

**Table 5. 5.** The mean values of NRMSE,  $R$  coefficient, and  $\Delta P_w/P_{ref,w}$  within the practical region.

Case	$\overline{\text{NRMSE}}$		$\bar{R}$		$\overline{\Delta P_w/P_{ref,w}}$	
	Proposed	Tuning	Proposed	Tuning	Proposed	Tuning
4	<b>0,032</b>	0,039	0,987	0,987	<b>0,061</b>	0,094
5	0,023	0,023	0,991	0,991	0,042	<b>0,041</b>
6	0,040	0,040	<b>0,955</b>	0,954	0,082	<b>0,075</b>
7	0,048	0,048	<b>0,962</b>	0,955	<b>0,081</b>	0,097
Average 4-7	<b>0,036</b>	0,037	<b>0,974</b>	0,972	<b>0,066</b>	0,077

For all the selected distances in Cases 4-7, the tuned function resulted in a  $\overline{\text{NRMSE}}$  of 0.046, which was better than the proposed function's  $\overline{\text{NRMSE}}$  of 0.053. It was mainly due to higher residuals from the proposed function's prediction at the downstream distances near the turbine. However, within the practical region, the proposed function could give a  $\overline{\text{NRMSE}}$  of 0.036, slightly better than the tuned function's  $\overline{\text{NRMSE}}$  of 0.037. Meanwhile,  $\bar{R}$  coefficients of the proposed function were better when compared to the tuning results in both the full-wake and practical regions.

Within the full-wake region in Cases 4-7, both the expansion functions yielded relatively high residuals for the mean normalized power difference  $\overline{\Delta P_w/P_{ref,w}}$  predictions. The highest  $\overline{\Delta P_w/P_{ref,w}}$  was obtained from the proposed function, mainly at the selected distances close to the turbine. However, within the practical region, both the expansion functions could obtain the accuracies of  $\Delta P_w/P_{ref,w} > 92\%$ . Specifically, the proposed function yielded  $\overline{\Delta P_w/P_{ref,w}}$  of 0.066, which was more accurate than the tuning result with  $\overline{\Delta P_w/P_{ref,w}}$  of 0.077.

## 5.5 Conclusion

A linear wake expansion function for the DG wake model is proposed to estimate the wake expansion and recovery behind a non-yawed HAWT without the expansion parameter tuning. Seven case studies from the LESs and wind tunnel measurements of non-yawed HAWT's wake under a variety of turbulent inflow conditions were used to examine the effectiveness of the proposed function. For the near-wake analyses in Cases 1-3, the proposed function could give rough but reasonable estimations of the DG wake profile expansion and its recovery from the high-fidelity LES results. For the full-wake analyses in Cases 4-7, the existing DG expansion function with a tunable parameter for the wake expansion was also added for comparison. In general, the full-wake predictions from the proposed and tuned functions for standard deviation  $\sigma$  and the centerline velocity deficit  $\Delta U_c/U_0$  were in good agreement with those of the benchmark datasets. As a result, both expansion functions could reasonably predict the wake expansions and their recoveries at most of the selected distances. It was observed that both expansion functions underestimated the wake velocity near the turbine, mainly due to the strong influence of the near-wake turbulence, which is not considered in the current analytical DG model.

The performances of both expansion functions for the evaluated Cases 4-7 were evaluated and compared using the NRMSE and  $R$  coefficient statistical measures. For all selected downstream distances in the full-wake region, the tuned function resulted in a mean NRMSE of 0.046, which is lower than the proposed function's mean NRMSE of 0.053. It was mainly due to higher residuals from the proposed function's prediction at the downstream distances near the turbine. However, within the practical region, the proposed function could give a mean NRMSE of 0.036, slightly better than the tuned function's mean NRMSE of 0.037. Meanwhile, the mean  $R$  coefficients of the proposed function were better when compared to the tuning results in both the full-wake and practical regions.

Those conducted statistical analyses could represent the proposed function's effectiveness in providing a reasonable estimation of the wake expansion and its recovery under a variety of inflow conditions in Cases 4-7. Moreover, both the expansion functions could provide the accuracies of mean  $P_w/P_{ref,w}$  predictions above 92%. Specifically, the proposed function yielded a mean  $\Delta P_w/P_{ref,w}$  of 0.066, which was more accurate than the tuning function prediction with a mean  $\Delta P_w/P_{ref,w}$  of 0.077. These results become evidence regarding the feasibility of the proposed expansion function to give a reasonable prediction of  $P_w/P_{ref,w}$ .

For future works, the DG model with the proposed function could be combined with the available wake-merging methods to predict the power of clustered HAWTs in a wind farm. Meanwhile, the proposed function could be extended to include the anisotropic nature of the wake

expansion, thus allowing its usability under different atmospheric stabilities. In addition, more data from high-fidelity LESs of HAWT wakes under varying inflow conditions and atmospheric stabilities would be necessary for further evaluations of analytical wake modeling.

## Chapter 6

# Analysis of multiple wakes behind the HAWTs

### 6.1 The wake flowfield of multiple turbines

In this study, the wake interactions between the turbines in a wind farm are represented using multiple wakes of three aligned HAWTs resulting from high-fidelity LES by FFB. The FFB data from the last eleven revolutions were averaged and processed using MATLAB. For the incoming velocity condition, the inlet velocity profile from the FFB simulation was best fitted using the power law profile with the shear exponent  $\alpha=0.1$  and was used as the inlet condition of the analytical modeling. The profile comparison is shown in Fig. 6.1.

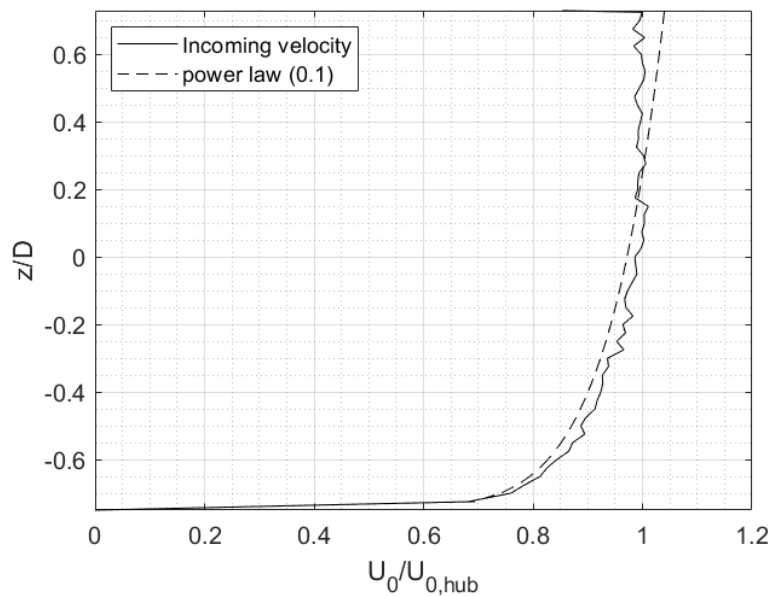


**Figure 6. 1.** Inlet velocity profile of the FFB simulation for the triple turbine case and its power law fit.

Three NREL 5 MW offshore wind turbines are aligned in the streamwise position with spacing distances of  $7.5D$  and were operated under an ABL inlet with turbulence. The resulting contours from the LES result of mean wake velocity on the horizontal and vertical planes are shown in Fig. 6.2.

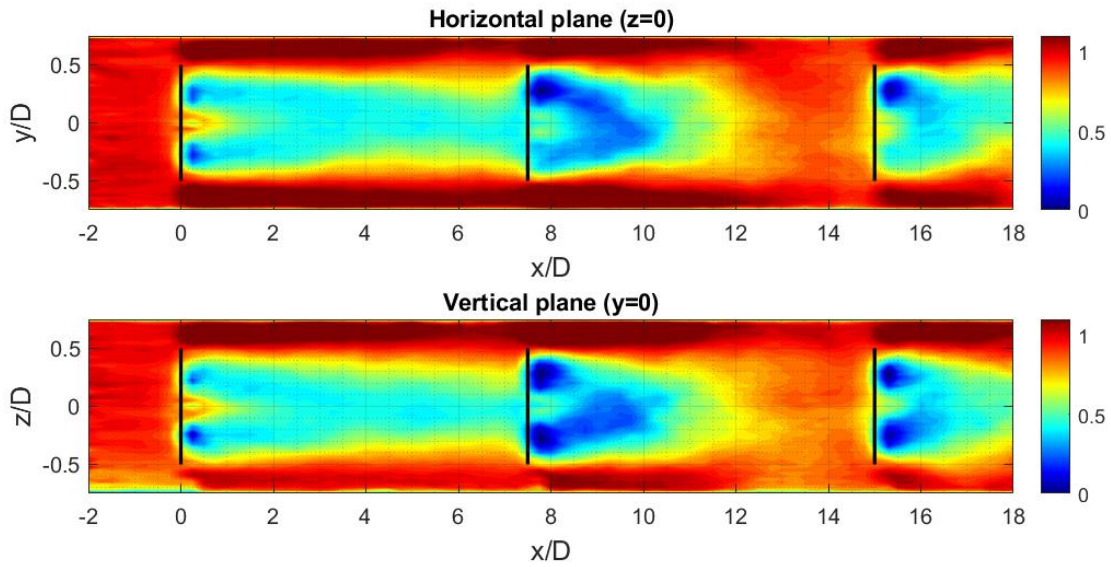


**Figure 6. 2.** Contours of the mean wake velocity of triple turbines on the horizontal and vertical planes.

It is clearly shown that a significant reduction of the inlet velocity occurred within the wake region. The maximum velocity deficit occurs downstream of the blade midspan position due to the maximum lift during the wind energy extraction by the rotor. Meanwhile, the higher wake velocity can be observed around the hub center position at the distance just behind the turbine, which indicates the double-Gaussian profile has formed. The full wake region can be observed downstream of the 1<sup>st</sup> turbine, where the spacing distance of  $7.5D$  seems too short for the wake to fully recover, at least for the presented case. In addition, the contour of streamwise turbulence intensity  $TI_x$  within the wake field is shown in Fig. 6.3.

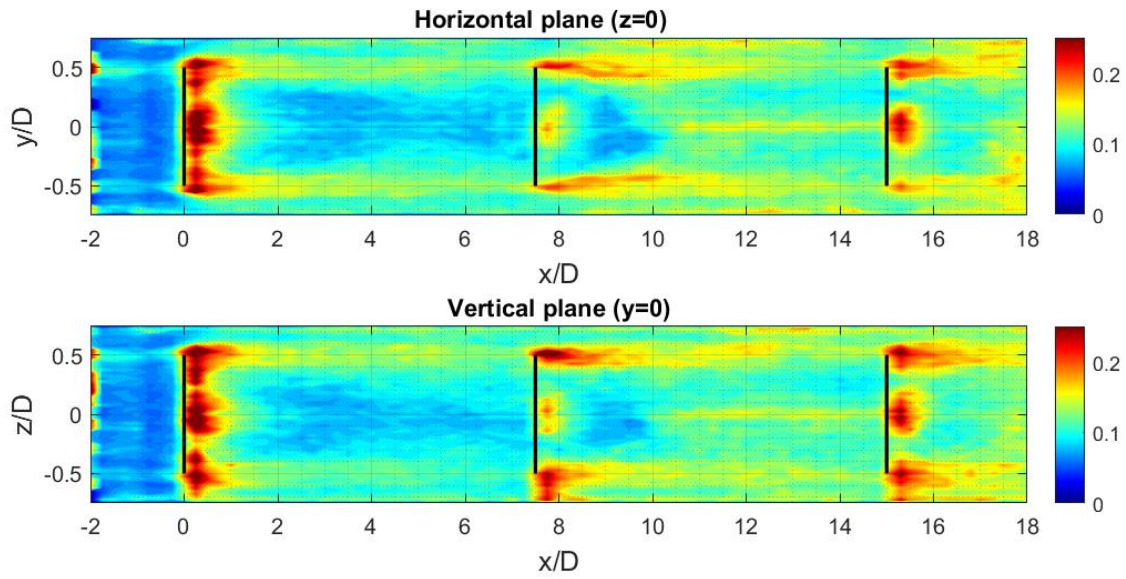


**Figure 6. 3.** Contours of the streamwise turbulence intensity of triple turbines on the horizontal and vertical planes.

The significant  $TI_x$  occurs just behind the turbine and around the blade tip due to the formation of vortical structures that swirl toward the streamwise direction. This helical pattern also contributes to the development of the mixing region, which is known for its role to determine the wake recovery rates. It is also observed that the turbulence is higher at the region just behind the nacelle and tower but reduced after approximately  $1D$  downstream of the turbine. As a result, the turbulence within the wake region is approximately the same as the ambient turbulence intensity. Further analysis of the  $TI_x$  within the rotor cross-sectional area is shown in Fig. 6.4.

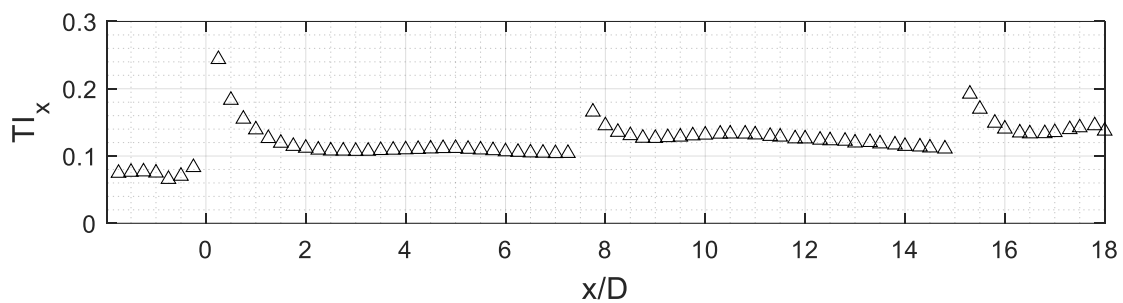


**Figure 6. 4.** Profile of the streamwise turbulence intensity within multiple wakes behind the triple turbines.

It is shown that the  $TI_x$  is significantly increased from the upstream distance near the rotors to around  $0.25D$  behind the rotors. Afterward, its intensity reduced to approximately the ambient level. Thus, the mean value of the ambient  $TI_x$  could be considered as the incoming  $TI_x$  of the downstream turbines, particularly for the analytical wake modeling of multiple wakes. However,

further work would be needed to directly model the  $Tl_x$  within the wake region by including the effect of internal or added turbulence intensity generated by the rotor.

## 6.2 Analytical modeling of multiple wakes

The proposed wake expansion function was further examined to model multiple wakes of three NREL 5 MW HAWTs, which is currently being simulated using high-fidelity LES by FFB. The wind power potential that is possible to be extracted by the turbine is located within the rotor area. Thus, the wake velocity at the evaluated downstream distances was measured using geometric averaging within the rotor cross-sectional rotor area along the streamwise direction defined as follows:

$$U = \left( \prod_{i=1}^n U_i \right)^{\frac{1}{n}} = \sqrt[n]{U_1 U_2 \dots U_n}, \quad (6.1)$$

where  $U$  is the geometric averaging of wake velocity. The location of each measurement  $i$ -point is shown in Fig. 6.5.

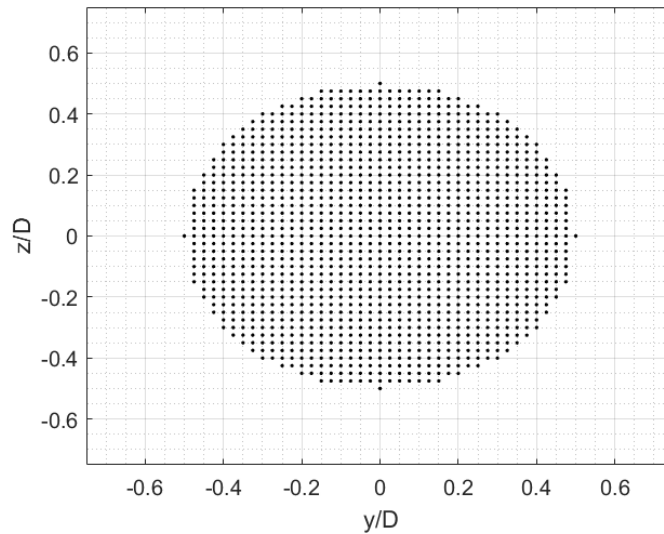


**Figure 6. 5.** Measurement points for geometric averaging of the wake velocity.

There are 1257 points in total with a spacing of  $0.025D$  that were distributed equally in the cross-sectional plane normal to the streamwise wind direction. The cross-sectional velocity was measured along the entire streamwise direction of the computational domain, with an equal spacing of  $0.25D$ . Meanwhile, to estimate the overlapping wake velocity in the multiple turbines, the wake merging method using rotor-based linear sum was used using the following relation [67]:

$$U = U_0 - \sum_{i=1}^n \Delta U_i, \quad (6.2)$$

where  $U_0$  is the reference velocity. The velocity deficit of the  $i^{\text{th}}$  turbine  $\Delta U_i$  is defined as follows:

$$\Delta U_i = U_{h,i} \left(1 - U_i / U_{h,i}\right), \quad (6.3)$$

where  $U_{h,i}$  is the geometrical averaging velocity over the  $i^{\text{th}}$  rotor.

Here, the streamwise rotor velocity  $U_{h,i}$  was measured at the distance of  $0.25D$  just behind the rotor, where this velocity was also used as the reference incoming velocity to calculate the tip speed ratio of each turbine (TSR). A constant tangential velocity of the blades' tip was set for all the turbines. Commonly, the information on  $C_t$  is only available for the 1<sup>st</sup> turbine, thus the estimation of the  $C_t$  for the downstream turbines can be obtained using the lookup table. The  $C_t$  value resulting from WT\_perf, a wind-turbine performance code developed by the National Wind Technology Center (NWTC) [68], was used for this purpose. The obtained  $C_t$  values from WT\_perf were compared against the FFB result for validation purpose, as shown in Fig. 6.6.

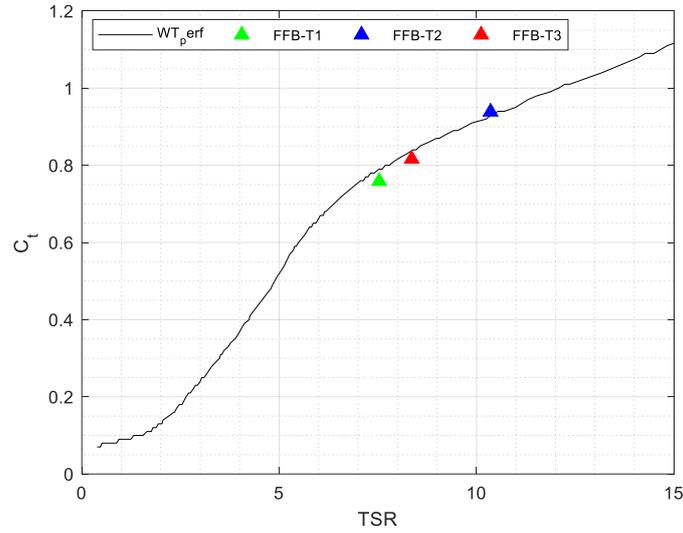


**Figure 6. 6.** The thrust coefficient ( $C_t$ ) of NREL 5 MW turbine as a function TSR.

The results show that the  $C_t$  estimations from WT\_perf are in good agreement with the benchmark FFB data. Hence, the WT\_perf was used to estimate the  $C_t$  of all the turbines. The result of the DG model prediction with the proposed function is shown in Fig. 6.7.

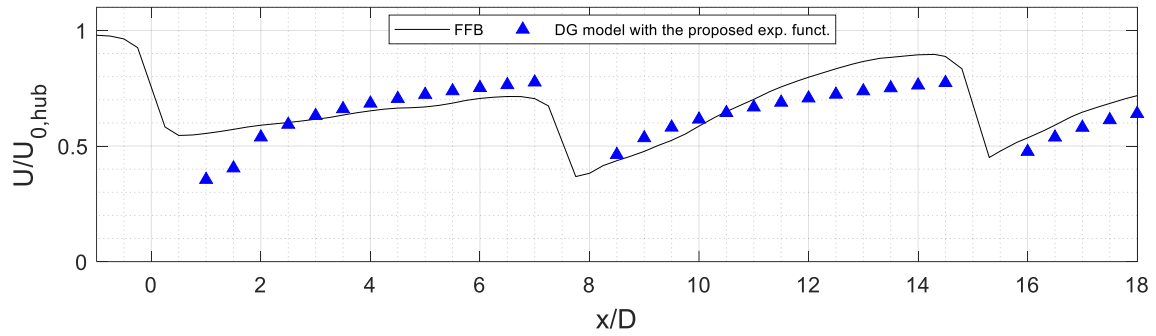


**Figure 6. 7.** Geometric averaging of wake velocity downstream of the triple turbines.

In general, the wake velocity resulting from the analytical model is in a good agreement with the FFB result. For a fully-developed wake behind the 1<sup>st</sup> turbine, a noticeable difference between the analytical prediction and LES result can be observed up to  $2D$  behind the turbine, due to the effect of internal turbulence generated by the turbine. This result can be further analyzed by referring to the streamwise profile of turbulence intensity as shown in Figure 6.4. The sudden increase of turbulence, which peaked at about  $0.25D$  just behind the rotors, may accelerate the wake flow just behind the turbine, particularly until  $2D$  behind the 1<sup>st</sup> turbine. As a result, the prediction from the analytical wake model underestimated the wake velocity just behind the rotor due to the neglect of the acceleration term of the derived formula for simplification. A noticeable different between FFB and analytical results was observed within the 2<sup>nd</sup> turbine's wake, particularly after  $11D$ . This may possibly due to the wake of 2<sup>nd</sup> turbine that has yet to reach the entire domain or fully-developed, thus causing a slightly higher velocity compared to the analytical result.

### 6.3 Conclusion

In this study, the wake interactions between the turbines in a wind farm were represented using multiple wakes of three aligned HAWTs resulting from high-fidelity LES by FFB. Three NREL 5 MW offshore wind turbines were aligned in the streamwise position with spacing distances of  $7.5D$  and were operated under an ABL inlet with turbulence. It was clearly shown that a significant reduction of the incoming velocity occurred within the wake region. The maximum velocity deficit occurred downstream of the blade midspan position due to the maximum lift during the wind energy extraction by the rotor. Meanwhile, the higher wake velocity was observed around the hub center position at the distance just behind the turbine, which indicates the double-Gaussian profile has formed. In addition, the contour of streamwise turbulence intensity was found significant at the region just behind the turbine and around the blade tip due to the formation of vortical structures that swirl toward the streamwise direction. It was also

observed that the turbulence intensity was higher in the region just behind the nacelle and tower but reduced after approximately  $1D$  downstream of the turbine. As a result, the turbulence intensity was approximately the same as the ambient level, particularly within the far-wake region.

Furthermore, the DG analytical wake model with the proposed expansion function was incorporated with the rotor-based wake merging method to predict the geometric averaging velocity of multiple wakes behind HAWTs. In general, the result shows that the analytical prediction could give a good agreement with the benchmark dataset from high-fidelity LES by FFB. This indicates the ability of the proposed expansion function to be used in predicting multiple wakes behind the HAWTs in addition to the single wake cases. Noticeable differences between the analytical prediction and LES result were observed up to  $2D$  downstream of the 1<sup>st</sup> turbine. These deviations might be affected by the sudden increase of the turbulence intensity just behind the 1<sup>st</sup> rotor, which could accelerate the surrounding wake flowfield. As a result, analytical prediction underestimated the wake velocity up to the related downstream distance due to the neglect of the acceleration term of the derived DG model formula for simplification. Meanwhile, the residuals between FFB and analytical results were also observed within the 2<sup>nd</sup> turbine's wake, particularly after  $11D$ . This might be due to the 2<sup>nd</sup> turbine's wake that has yet to meet the fully-developed condition, thus causing a slightly higher velocity compared to the analytical result.

## Chapter 7

### General discussion

This study presents valuable insight into the wake transition mechanism and its behavior within a full-wake region behind an isolated non-yawed HAWT using the analytical approach. A summary of each work is described below.

#### ◆ Investigation of the near-wake behavior of an isolated HAWT

This study revealed the DG wake velocity distribution and its anisotropic behavior within the near-wake region downstream of a HAWT. It was observed that the spatial distribution of the wake profile tends to form a DG shape, particularly within the near-wake region. This tendency underpins the feasibility of the DG function to estimate the streamwise velocity distribution within the near-wake region where the effect of turbine geometry is salient. Moreover, it was observed that the wake tends to expand in an anisotropic way in which the wake growth rate in the vertical direction is less than in the lateral direction. Hence, for analytical wake modeling, it is recommended to consider the DG shape function with anisotropic expansion for better accuracy of streamwise velocity prediction within the near-wake region.

#### ◆ Anisotropic DG analytical wake model for an isolated HAWT

By considering the anisotropic behavior of the wake expansion behind an isolated HAWT, the anisotropic DG wake model was proposed. Three case studies from LESs and lidar measurements of utility-scale HAWTs were used to validate the effectiveness of the proposed anisotropic model. For the LES results, it was found that the wake expanded in an anisotropic manner. Meanwhile, for the lidar measurement case, the wake expands at the same expansion rate from both lateral and vertical directions. This was mainly caused by the limitation on lidar measurement data, which only provided the wake centerline velocity along the streamwise direction. In general, the proposed anisotropic expansion function can give a better prediction of wake profile distribution within a full-wake region when compared to the SG and top-hat shape wake models.

#### ◆ A linear wake expansion function for the DG analytical wake model

This work focused on the development of a linear wake expansion function for the DG analytical wake model. The proposed linear expansion function for the DG wake model was derived from the existing formulations based on the conservation of mass and momentum. As a result, the proposed function can be used directly without tuning. Its performance was validated with the LES and wind tunnel measurement data. In addition, the proposed function was also compared to the existing wake expansion function for the DG model with tuning. In general, the statistical evaluation results from all the case studies showed that the proposed expansion function for the DG wake model could provide a reasonable estimation for wake expansion prediction within the full-wake region.

#### ◆ **Analysis of multiple wakes behind the HAWTs**

This chapter discussed the application of the DG model with the proposed expansion function to estimate multiple wakes from three aligned NREL 5MW HAWTs. The thrust coefficient,  $C_t$ , was estimated from the obtained TSR using lookup data resulting from WT\_perf and was validated against the LES result. It was found that the WT\_perf could give a reasonable estimation of  $C_t$ , thus was used to estimate  $C_t$  of the respective HAWTs based on their TSRs. Next, the DG model with the proposed expansion function was incorporated with the rotor-based wake merging method to predict multiple wakes behind HAWTs. The result shows that the analytical prediction of geometric averaging wake velocity could give a good agreement with the benchmark dataset from high-fidelity LES by FFB. This indicates the ability of the proposed expansion function to be used in predicting multiple wakes behind the HAWTs in addition to the single wake cases.

## **Chapter 8**

### **Conclusion and future works**

#### **8.1 Conclusion**

The main work in this study focused on the development of an analytical wake model to estimate the wake transition mechanism and its behavior behind an isolated non-yawed utility-scale HAWT using the DG approach. The observed anisotropic behavior of the wake expansion within the near-wake region was further considered to develop an anisotropic wake model based on the DG approach. The proposed anisotropic model can better provide the wake transition mechanism within a full-wake region. This wake transition mechanism was also confirmed by the LES simulation results and experimental measurement. In addition, a linear wake expansion function for the DG wake model was proposed. The effectiveness of the proposed function was also validated with the results from LES simulations and experimental measurements. In addition, the DG wake model with the proposed expansion function was further evaluated to predict the wake velocity potential of multiple turbines. It was confirmed that the proposed expansion function could reasonably estimate the wake expansion within a full-wake region of the evaluated case studies. Thus, allowing the DG model usability for practical applications. Finally, the main features, findings, and contributions of the conducted research works in this dissertation are summarized in Table 8.1.

**Table 8. 1.** Main features, findings, and contributions of the conducted research works.

Research works	Main features	Findings	Contributions
Investigation of the near-wake behavior of an isolated horizontal-axis wind turbine	The near-wake analysis using high-fidelity LES by FFB.	<ul style="list-style-type: none"> <li>- Within the near-wake region, it was clarified that the spatial distribution of the wake profile tends to form a DG shape.</li> <li>- It was observed that as the downstream distance increased, the discrepancy of velocity between two local minima located around the blade mid-span and the wake center was gradually reduced.</li> <li>- The near-wake velocity expanded in an anisotropic way and tends to expand linearly with the downstream distance.</li> </ul>	A valuable insight of the anisotropic wake expansion within the near-wake region which could be observed using high-fidelity LES.
Anisotropic double-Gaussian analytical wake model for an isolated horizontal-axis wind turbine	<ul style="list-style-type: none"> <li>- The anisotropic nature of the wake expansion is considered, thus resulting in a more realistic representation of the wake expansion within the full-wake region.</li> <li>- The proposed anisotropic DG model facilitates the wake modeling within the full-wake region behind the HAWT under different atmospheric stability.</li> </ul>	<ul style="list-style-type: none"> <li>- The proposed DG model was found to effectively model the wake transition mechanism and anisotropic wake expansion represented by the different expansion rates in both lateral and vertical directions.</li> <li>- A pair of the scaling coefficient <math>c=1.2</math> and the Gaussian local minima <math>r_0=0.26</math> were found to give lesser RMSEs for the wake velocity predictions compared to the other pairing values. Thus, its usability is recommended, particularly for the DG analytical modeling of the utility-scale HAWTs.</li> </ul>	A new low-cost analytical wake model that can predict the wake velocity transition mechanism within the full-wake region considering the anisotropic nature of the wake expansion.

	<ul style="list-style-type: none"> <li>- Constant values of the radial position of Gaussian minima <math>r_0</math> and the scale factor <math>c</math> in the far-wake onset formula for the utility-scale turbine were determined empirically.</li> </ul>	<ul style="list-style-type: none"> <li>- Instead of the DG model's accuracy within the near-wake region, it was found that the model could provide a feasible prediction within the far-wake region with a mean RMSE of approximately 0.03.</li> </ul>
<p>A linear wake expansion function for the double-Gaussian analytical wake model</p>	<ul style="list-style-type: none"> <li>- The proposed linear wake expansion function for the DG model can be used directly without tuning.</li> <li>- Only two input parameters are needed to use the DG model with the proposed expansion function:             <ol style="list-style-type: none"> <li>1. Thrust coefficient, <math>C_t</math>;</li> <li>2. Streamwise incoming turbulence intensity, <math>TI_x</math>.</li> </ol> </li> </ul>	<ul style="list-style-type: none"> <li>- The proposed linear expansion function could give reasonable predictions of the standard deviation of the velocity deficit profile (<math>\sigma</math>), which can be observed from its good agreement compared to the benchmark data sets.</li> <li>- In general, the DG model with the proposed expansion function could give feasible predictions of the wake velocity distribution, where the NRMSEs within the full and practical wake regions were 0.053 and 0.036, respectively. However, NRMSE was observed up to approximately 0.16 within the blade mid-span area at the downstream distances just behind the turbine.</li> <li>- The DG model with the proposed function could effectively predict the potential wake velocity of multiple wakes, particularly within the fully-developed wake region.</li> </ul> <p>A new linear wake expansion function for the DG analytical wake model.</p>

## 8.2 Limitations and future works

In general, the conducted research works on analytical wake modeling can give a feasible prediction of the wake transition mechanism behind the HAWT represented by the wake velocity distribution and its expansion within a full-wake region. However, some simplifications being made cause some limitations on the analytical model's performance which could be investigated in the future. Some limitations and their possible future works are summarized in Table 8.2.

**Table 8. 2.** Limitations and future works.

<b>Limitations</b>	<b>Future works</b>
In most cases, the proposed anisotropic model underestimated the wake velocity around the blade midspan position just behind the turbine.	It is hypothesized that the neglect of the acceleration term in the conservation equation when deriving the physically-based DG model for simplification purpose may affect the model's accuracy within the downstream distances near the turbine. Hence, further investigation may be essential to overcome this limitation.
The wake growth rate parameters for both lateral and vertical directions ( $k_y$ and $k_z$ ) in the proposed anisotropic DG model still need to be tuned by case.	More high-fidelity LESs of HAWT wakes under different inflow conditions and atmospheric stabilities need to be performed to further elucidate the anisotropic characteristics of the HAWT wake expansion. Thus, the universal expression for anisotropic wake expansion behind the HAWT can be derived accordingly.
The wake deflection and meandering are not considered in the present study of analytical wake modeling.	Future work could extend to include the wake deflection for the case of the HAWT with the yawed condition and very large turbulent eddies in the incoming boundary layer.
The streamwise turbulence intensity data within the wake region of the upstream turbines is needed for the wake modeling of the downstream turbines.	The analytical modeling of streamwise turbulence intensity within the wake region of the downstream turbines would be useful for the DG model to predict multiple wakes.
Structural responses to the aerodynamic loads from the wake are not modeled in the present study.	Further investigation is needed to incorporate the analytical wake model with the structural dynamics module to account for the unsteady loads experienced by HAWTs and their feedback to the wake flowfield.

## References

- [1] L. J. Vermeer, J. N. Sørensen, and A. Crespo, “Wind turbine wake aerodynamics,” *Prog. Aerosp. Sci.*, vol. 39, no. 6, pp. 467–510, 2003, doi: [https://doi.org/10.1016/S0376-0421\(03\)00078-2](https://doi.org/10.1016/S0376-0421(03)00078-2).
- [2] M. Magnusson, “Near-wake behaviour of wind turbines,” *J. Wind Eng. Ind. Aerodyn.*, vol. 80, no. 1, pp. 147–167, 1999, doi: [https://doi.org/10.1016/S0167-6105\(98\)00125-1](https://doi.org/10.1016/S0167-6105(98)00125-1).
- [3] V. L. Okulov, I. V. Naumov, R. F. Mikkelsen, I. K. Kabardin, and J. N. Sørensen, “A regular Strouhal number for large-scale instability in the far wake of a rotor,” *J. Fluid Mech.*, vol. 747, pp. 369–380, 2014, doi: [10.1017/jfm.2014.174](https://doi.org/10.1017/jfm.2014.174).
- [4] F. Porté-Agel, M. Bastankhah, and S. Shamsoddin, “Wind-Turbine and Wind-Farm Flows: A Review,” *Boundary-Layer Meteorol.*, vol. 174, no. 1, pp. 1–59, 2020, doi: [10.1007/s10546-019-00473-0](https://doi.org/10.1007/s10546-019-00473-0).
- [5] M. Bastankhah and F. Porté-Agel, “A new analytical model for wind-turbine wakes,” *Renew. Energy*, vol. 70, pp. 116–123, 2014, doi: [10.1016/j.renene.2014.01.002](https://doi.org/10.1016/j.renene.2014.01.002).
- [6] S. Xie and C. Archer, “Self-similarity and turbulence characteristics of wind turbine wakes via large-eddy simulation,” *Wind Energy*, vol. 18, no. 10, pp. 1815–1838, 2015, doi: [10.1002/we.1792](https://doi.org/10.1002/we.1792).
- [7] J. K. Kaldellis, P. Triantafyllou, and P. Stinis, “Critical evaluation of Wind Turbines’ analytical wake models,” *Renew. Sustain. Energy Rev.*, vol. 144, p. 110991, 2021, doi: <https://doi.org/10.1016/j.rser.2021.110991>.
- [8] NEL, “Characterisation of Downstream Flow from Large Wind Turbines,” p. 100, 2014.
- [9] B. Sanderse, “Aerodynamics of wind turbine wakes: Literature review,” *Energy Res. Cent. Netherlands*, pp. 1–46, 2009, doi: [10.1002/we](https://doi.org/10.1002/we).
- [10] P. Clive, S. Scientist, and A. Energy, “Scanning lidar measurements of offshore wind turbine wakes,” 2015.
- [11] M. Placidi and P. Hancock, “Veers’ Extension to Non- neutral Incoming Winds ( VENTI ),” 2019.
- [12] C. L. Archer *et al.*, “Review and evaluation of wake loss models for wind energy applications,” *Applied Energy*. 2018, doi: [10.1016/j.apenergy.2018.05.085](https://doi.org/10.1016/j.apenergy.2018.05.085).
- [13] B. Sanderse, S. P. van der Pijl, and B. Koren, “Review of computational fluid dynamics for wind turbine wake aerodynamics,” *Wind Energy*, vol. 14, no. 7, pp. 799–819, Oct. 2011, doi: [10.1016/j.weneng.2011.08.001](https://doi.org/10.1016/j.weneng.2011.08.001).

<https://doi.org/10.1002/we.458>.

- [14] E. G. A. Antonini, D. A. Romero, and C. H. Amon, “Improving CFD wind farm simulations incorporating wind direction uncertainty,” *Renew. Energy*, 2019, doi: 10.1016/j.renene.2018.10.084.
- [15] F. Porté-Agel, Y. T. Wu, H. Lu, and R. J. Conzemius, “Large-eddy simulation of atmospheric boundary layer flow through wind turbines and wind farms,” *J. Wind Eng. Ind. Aerodyn.*, vol. 99, pp. 154–168, 2011, doi: 10.1016/j.jweia.2011.01.011.
- [16] M. J. Churchfield, S. Schreck, L. A. Martínez-Tossas, C. Meneveau, and P. R. Spalart, “An advanced actuator line method for wind energy applications and beyond,” in *35th Wind Energy Symposium, 2017*, 2017, doi: 10.2514/6.2017-1998.
- [17] W. Z. Shen, J. N. Sørensen, and J. H. Zhang, “Actuator surface model for wind turbine flow computations,” in *European Wind Energy Conference and Exhibition 2007, EWEC 2007*, 2007.
- [18] Y. Li, K. J. Paik, T. Xing, and P. M. Carrica, “Dynamic overset CFD simulations of wind turbine aerodynamics,” *Renew. Energy*, vol. 37, pp. 285–298, 2012, doi: 10.1016/j.renene.2011.06.029.
- [19] J. M. O’Brien, T. M. Young, J. M. Early, and P. C. Griffin, “An assessment of commercial CFD turbulence models for near wake HAWT modelling,” *J. Wind Eng. Ind. Aerodyn.*, vol. 176, pp. 32–53, 2018, doi: 10.1016/j.jweia.2018.03.001.
- [20] N. O. Jensen, “A note on wind generator interaction,” *Risø-M-2411 Risø Natl. Lab. Roskilde*, pp. 1–16, 1983.
- [21] I. Katic, J. Hojstrup, and N. O. Jensen, “A simple model for cluster efficiency.,” 1986.
- [22] S. Frandsen *et al.*, “Analytical modelling of wind speed deficit in large offshore wind farms,” *Wind Energy*, vol. 9, pp. 39–53, 2006, doi: 10.1002/we.189.
- [23] J. N. Sorensen, R. F. Mikkelsen, D. S. Henningson, S. Ivanell, S. Sarmast, and S. J. Andersen, “Simulation of wind turbine wakes using the actuator line technique,” *Philos. Trans. R. Soc. A Math. Phys. Eng. Sci.*, vol. 373, no. 2035, 2015, doi: 10.1098/rsta.2014.0071.
- [24] M. L. Aitken, R. M. Banta, Y. L. Pichugina, and J. K. Lundquist, “Quantifying Wind Turbine Wake Characteristics from Scanning Remote Sensor Data,” *J. Atmos. Ocean. Technol.*, vol. 31, no. 4, pp. 765–787, 2014, doi: 10.1175/JTECH-D-13-00104.1.
- [25] A. Keane, P. E. O. Aguirre, H. Ferchland, P. Clive, and D. Gallacher, “An analytical model for a full wind turbine wake,” *J. Phys. Conf. Ser.*, vol. 753, p. 32039, 2016, doi: 10.1088/1742-6596/753/3/032039.

- [26] J. Schreiber, A. Balbaa, and C. L. Bottasso, “Brief communication: A double-Gaussian wake model,” *Wind Energ. Sci.*, vol. 5, no. 1, pp. 237–244, Feb. 2020, doi: 10.5194/wes-5-237-2020.
- [27] A. Keane, “Advancement of an analytical double-Gaussian full wind turbine wake model,” *Renew. Energy*, vol. 171, pp. 687–708, 2021, doi: <https://doi.org/10.1016/j.renene.2021.02.078>.
- [28] M. Abkar and F. Porté-Agel, “Influence of atmospheric stability on wind-turbine wakes: A large-eddy simulation study,” *Phys. Fluids*, vol. 27, no. 3, p. 35104, Mar. 2015, doi: 10.1063/1.4913695.
- [29] M. Bastankhah and F. Porté-Agel, “Experimental and theoretical study of wind turbine wakes in yawed conditions,” *J. Fluid Mech.*, vol. 806, pp. 506–541, 2016, doi: DOI: 10.1017/jfm.2016.595.
- [30] A. L. R. James F. Manwell, Jon G. McGowan, *Wind Energy Explained: Theory, Design and Application, 2nd Edition*. Wiley, 2010.
- [31] J. Van Der Tempel, “Design of Support Structures for Offshore Wind Turbines,” Technische Universiteit Delft, 2006.
- [32] T. Burton, N. Jenkins, D. Sharpe, and E. Bossanyi, *Wind Energy Handbook*. 2011.
- [33] G. M. Masters, *Renewable and Efficient Electric Power Systems*. 2004.
- [34] D. P. Rommel, D. Di Maio, and T. Tinga, “Calculating wind turbine component loads for improved life prediction,” *Renew. Energy*, vol. 146, pp. 223–241, 2020, doi: 10.1016/j.renene.2019.06.131.
- [35] I. E. A. IEA, “World Energy Outlook 2019 – Analysis - IEA,” *World Energy Outlook 2019*, 2019. .
- [36] D. Lopez, J. Kuo, and N. Li, “A novel wake model for yawed wind turbines,” *Energy*, 2019, doi: 10.1016/j.energy.2019.04.120.
- [37] L. P. Chamorro and F. Porté-Agel, “A Wind-Tunnel Investigation of Wind-Turbine Wakes: Boundary-Layer Turbulence Effects,” *Boundary-Layer Meteorol.*, vol. 132, no. 1, pp. 129–149, 2009, doi: 10.1007/s10546-009-9380-8.
- [38] P.-Å. Krogstad and M. S. Adaramola, “Performance and near wake measurements of a model horizontal axis wind turbine,” *Wind Energy*, vol. 15, no. 5, pp. 743–756, Jul. 2012, doi: <https://doi.org/10.1002/we.502>.
- [39] H. Sun and H. Yang, “Study on an innovative three-dimensional wind turbine wake model,” *Appl. Energy*, vol. 226, pp. 483–493, 2018, doi:

<https://doi.org/10.1016/j.apenergy.2018.06.027>.

- [40] S. McTavish, D. Feszty, and F. Nitzsche, “A study of the performance benefits of closely-spaced lateral wind farm configurations,” *Renew. Energy*, vol. 59, pp. 128–135, 2013, doi: <https://doi.org/10.1016/j.renene.2013.03.032>.
- [41] J. Jonkman, S. Butterfield, W. Musial, and G. Scott, “Definition of a 5-MW reference wind turbine for offshore system development,” *Contract*, 2009, doi: 10.1002/ajmg.10175.
- [42] J. D’Errico, “fminsearchcon.” MATLAB Central File Exchange, 2021.
- [43] I. Katić, J. Højstrup, and N. O. Jensen, “A Simple Model for Cluster Efficiency,” 1987.
- [44] M. Churchfield *et al.*, “A Large-Eddy Simulation of Wind-Plant Aerodynamics,” in *50th AIAA Aerospace Sciences Meeting including the New Horizons Forum and Aerospace Exposition*, American Institute of Aeronautics and Astronautics, 2012.
- [45] J. Annoni, P. Seiler, K. Johnson, P. Fleming, and P. Gebraad, “Evaluating wake models for wind farm control,” in *2014 American Control Conference*, 2014, pp. 2517–2523, doi: 10.1109/ACC.2014.6858970.
- [46] T. Ishihara and G. W. Qian, “A new Gaussian-based analytical wake model for wind turbines considering ambient turbulence intensities and thrust coefficient effects,” *J. Wind Eng. Ind. Aerodyn.*, 2018, doi: 10.1016/j.jweia.2018.04.010.
- [47] M. L. Aitken and J. K. Lundquist, “Utility-Scale Wind Turbine Wake Characterization Using Nacelle-Based Long-Range Scanning Lidar,” *J. Atmos. Ocean. Technol.*, vol. 31, no. 7, pp. 1529–1539, 2014, doi: 10.1175/JTECH-D-13-00218.1.
- [48] A. Keane, P. E. O. Aguirre, H. Ferchland, P. Clive, and D. Gallacher, “An analytical model for a full wind turbine wake,” Feb. 2017, doi: 10.1088/1742-6596/753/3/032039.
- [49] P. K. Chaviaropoulos, D. Chortis, and D. Lekou, “INNWIND. D1.2.1 – Definition of the Reference Wind Turbine—Analysis of Rotor Design Parameters,” *INNWIND.EU*, no. November 2012, pp. 1–30, 2013.
- [50] CENER, “Closed Loop Wind Farm Control (CL-Windcon) - Research data,” 2020.
- [51] the U. of T. Center for Research on Innovative Simulation Software, Institute of Industrial Science (IIS), “FrontFlow/blue version.8.1.”
- [52] M. Churchfield, S. Lee, and P. Moriarty, “Overview of the Simulator for Offshore Wind Farm Application (SOWFA),” *NREL*, p. 109, 2012.
- [53] D. Gallacher and G. More, “Lidar measurements and visualisation of turbulence and wake

decay length,” *Eur. Wind Energy Assoc. Conf. Exhib. 2014, EWEA 2014*, Jan. 2014.

- [54] Fraunhofer Institute for Wind Energy Systems (Fraunhofer IWES), “Wind Conditions.”
- [55] B. Ernst and J. R. Seume, “Investigation of Site-Specific Wind Field Parameters and Their Effect on Loads of Offshore Wind Turbines,” *Energies*, vol. 5, no. 10. 2012, doi: 10.3390/en5103835.
- [56] A. Rohatgi, “Webplotdigitizer: Version 4.4.” 2020.
- [57] H. Beck, J. J. Trujillo, G. Wolken-möhlmann, A. P. Diaz, and V. C. Gomes, “D5.10 Mesoscale effects on wind farm energy yield reported,” no. D5.10, 2015.
- [58] R. J. Barthelmie, S. T. Frandsen, M. N. Nielsen, S. C. Pryor, P.-E. Rethore, and H. E. Jørgensen, “Modelling and measurements of power losses and turbulence intensity in wind turbine wakes at Middelgrunden offshore wind farm,” *Wind Energy*, vol. 10, no. 6, pp. 517–528, Nov. 2007, doi: <https://doi.org/10.1002/we.238>.
- [59] Y. T. Wu and F. Porté-Agel, “Modeling turbine wakes and power losses within a wind farm using LES: An application to the Horns Rev offshore wind farm,” *Renew. Energy*, vol. 75, pp. 945–955, 2015, doi: 10.1016/j.renene.2014.06.019.
- [60] P. Veers *et al.*, “Grand challenges in the science of wind energy,” *Science (80-. )*, vol. 366, no. 6464, 2019, doi: 10.1126/science.aau2027.
- [61] Z. Ti, X. W. Deng, and H. Yang, “Wake modeling of wind turbines using machine learning,” *Appl. Energy*, vol. 257, no. July 2019, 2020, doi: 10.1016/j.apenergy.2019.114025.
- [62] J. N. Sørensen and W. Z. Shen, “Numerical modeling of wind turbine wakes,” *J. Fluids Eng. Trans. ASME*, 2002, doi: 10.1115/1.1471361.
- [63] Q. M. B. Soesanto, T. Yoshinaga, and A. Iida, “Anisotropic double-Gaussian analytical wake model for an isolated horizontal-axis wind turbine,” *Energy Sci. Eng.*, vol. 10, no. 7, pp. 2123–2145, Jul. 2022, doi: <https://doi.org/10.1002/ese3.1120>.
- [64] X. Gao, H. Yang, and L. Lu, “Optimization of wind turbine layout position in a wind farm using a newly-developed two-dimensional wake model,” *Appl. Energy*, vol. 174, pp. 192–200, 2016, doi: 10.1016/j.apenergy.2016.04.098.
- [65] M. P. Van Der Laan *et al.*, “An improved k- $\epsilon$  model applied to a wind turbine wake in atmospheric turbulence,” *Wind Energy*, vol. 18, no. 5. pp. 889–907, 2015, doi: 10.1002/we.1736.
- [66] S. Ivanell, R. Mikkelsen, and D. Henningson, “Validation of methods using EllipSys3D,”

Mechanics, School of Engineering Sciences (SCI), KTH, 2008.

- [67] A. Niayifar and F. Porté-Agel, “Analytical modeling of wind farms: A new approach for power prediction,” *Energies*, vol. 9, no. 9, pp. 1–13, 2016, doi: 10.3390/en9090741.
- [68] M. L. Buhl, A. D. Wright, and J. L. Tangier, “Wind Turbine Design Codes: A Preliminary Comparison of the Aerodynamics,” *17th Am. Soc. Mech. Eng. Wind Energy Symp.*, no. December 1997, pp. 1–9, 1998.

## **Publication list**

### **List of Papers with Referee's Review**

1. Qidun M. B. Soesanto, Tsukasa Yoshinaga, Akiyoshi Iida, "Anisotropic double-Gaussian analytical wake model for an isolated horizontal-axis wind turbine," *Energy Science and Engineering*, Vol. 10, No. 7, pp.2123-2145, 2022. <https://doi.org/10.1002/ese3.1120>
2. Qidun M. B. Soesanto, Tsukasa Yoshinaga, Akiyoshi Iida, "A linear wake expansion function for the double-Gaussian analytical wake model," *Energy Science and Engineering* (in press), 2023. <https://doi.org/10.1002/ese3.1427>

### **Paper at International Conference with Referee's Review**

Qidun M. B. Soesanto, Tsukasa Yoshinaga, Akiyoshi Iida, "Investigation of the near-wake behavior of an isolated horizontal-axis wind turbine," *The 9<sup>th</sup> International Conference on Sustainable Energy Engineering and Applications (ICSEEA 2021)*, Online, pp.1-9, October 2021.